Peak Load Shaving and Power Quality Improvement for the Louis-Hippolyte-La Fontaine Tunnel in Montréal

Mohamed Ismail Hussein Omer

A Thesis

in

The Department

of

Electrical and Computer Engineering

Presented in Partial Fulfillment of the Requirements

for the Degree of Master of Applied Science at

Concordia University

Montréal, Québec, Canada

April 2018

CONCORDIA UNIVERSITY

SCHOOL OF GRADUATE STUDIES

This is to certify that the thesis prepared

By: Mohamed Omer

Entitled:
Peak Load Shaving and Power Quality Improvement for the
Louis-Hippolyte-La Fontaine Tunnel in Montréal

and submitted in partial fulfillment of the requirements for the degree of

Master of Applied Science

Complies with the regulations of this University and meets the accepted standards with respect to originality and quality.

Signed by the final examining committee:

_____ Chair
Dr. Y. Liu

_____ Examiner, External
Dr. A. Athienitis to the Program

_____ Examiner
Dr. A. K. Rathore

_____ Supervisor
Dr. P. Pillay

Approved by: _____
Dr. W. E. Lynch, Chair
Department of Electrical and Computer Engineering

_____20_____ _____
Dr. Amir Asif, Dean
Faculty of Engineering and Computer Science

ABSTRACT

Peak Load Shaving and Power Quality Improvement for the Louis-Hippolyte-La Fontaine Tunnel in Montréal

Mohamed Ismail Hussein Omer

The Louis-Hippolyte-La Fontaine Tunnel is one of the major access points to the island of Montreal, and in conjunction with the bridge, it is the longest underwater tunnel-bridge in Canada. Recent reports estimate that around 130,000 vehicles commute through the tunnel daily. High operational standards are required to ensure the safety of commuters. Hence, high-stress levels are reflected on the electrical grid. The high tension levels on electrical power grids and the expensive price of peak power demand have prompted both the consumer and the utility to adopt Energy Storage Systems (ESS) for peak load shaving.

In this thesis, a Battery Energy Storage System (BESS) is sized and controlled to reduce the constraints imposed on the electrical grid by the Louis-Hippolyte-La Fontaine Tunnel by means of peak load shaving. The peak load reduction is attained through peak load shaving by utilizing a BESS, and also through energy and peak load shaving by using BESS in conjunction with Photovoltaics solar cells (PV). Also in this thesis, a control scheme is developed for Voltage Source Inverters (VSI) used in peak shaving applications. The developed control first allows the VSI to interface peak shaving systems with the grid reducing stress levels imposed on the grid, and secondly, play the role of power factor correction for reactive power compensation, and finally, to implement the capabilities of active harmonic filters and harmonic mitigation techniques to suppress the harmonic content in the line current.

ACKNOWLEDGEMENT

The author would like to express his appreciation and gratitude to his family, his father Ismail Hussein Omer, mother Hanan Mohamed Abusamra, sisters Afaf, and Doha, and brother Hatim, who have been an anchor of hope, love, and guidance.

The author would like to express his appreciation to his supervisor, Dr. Pragasen Pillay for his guidance and continuous financial support throughout the master's program. The authors acknowledge the support of the Natural Sciences & Engineering Research Council of Canada, and Le Ministère des Transports, de la Mobilité Durable et de l'Électrification des Transports (MTMDET).

Lastly, the author acknowledges the support and encouragement of his friends, loved ones, and colleagues in the Power Electronics and Energy Research (PEER) group.

"To my beloved Fatima Hussein…"

Contents

List of Figures

List of Tables

Nomenclature

BESS	Battery Energy Storage Systems
ESS	Energy Storage Systems
NPV	Net Present Value
IRR	Internal Rate of Return
SAM	System Advisor Model
NREL	National Renewable Energy Laboratory
VSI	Voltage Source Inverter
VFD	Variable Frequency Drives
STATCOM	Static Compensators
SVC	Static VAR Compensators
THD	Total Harmonic Distortion
UPFC	Unity Power Factor Converter
UPS	Uninterruptible Power System
HCC	Hysteresis Current Controller
HB	Hysteresis Band
THD	Total Harmonic Distortion
PF	Power Factor
PV	Photovoltaics Solar Cells

CHAPTER 1

Introduction, Objective, and Thesis Outline

1.1 Introduction

1.1.1 Peak Shaving and Power Quality

The typical load profiles of customers would have load peaks at certain times of the day, and different peak levels through the year due to the seasonal load variations. The load variation is then reflected on the electrical grids and utilities as two components; Energy Consumption, and Peak Demands. The customers are accordingly billed for both components. Peak Demand charges can contribute up to 50% of the electricity bill [1], to encourage the customers to have a balanced overall demand profile and avoid having power demand spikes [2, 3]. The stress levels, power quality issues, and high peak demand charges have inspired customers and utilities to invest in peak shaving systems and power quality enhancement systems.

The fundamental idea of peak shaving is to limit the amount of power drawn from the grid to some level, and substitute for power demand higher than that level from local on-site power sources. A common practice to reduce these peaks is to introduce energy storage systems into the main electrical system. The energy storage system will be charged during off-peak operation hours and will discharge during peak operation hours thus reducing the peak power drawn from the grid.

As simple as the idea of peak shaving appears, peak shaving systems introduce power quality issues for both the customer and the utility. For instance, peak shaving systems that utilize Battery Energy Storage Systems (BESS) to store energy during off-peak hours, tend to generate line current harmonics in the system. The continuous flow of energy from the batteries to the load, and from the grid to the batteries is achieved by means of power electronic circuitry that utilizes non-linear elements such as diodes, IGBTs, and MOSFETs. These elements alter the current waveform and therefore, inject current harmonics to the electrical power grid.

In power systems, controlling the flow of reactive power is imperative to ensure the proper operation of the power system. For example, in power transmission and distribution systems, the

flow of reactive power increases the power losses in the lines and degrades the power factor of the overall system and hence, the power transfer capability is reduced [4].

The presence of harmonics in power systems is extremely harmful to both utilities and customers. For instance, customers who use capacitor banks to compensate for the flow of reactive power may face even more difficult problems with harmonics. Because the application of the capacitive elements to a system with high harmonic content (high THD), can result in the amplification of certain harmonic orders [5]. As a result, higher currents pass through the capacitor banks shortening their expected lifetime [6]. To mitigate the harmonic content in power systems, harmonic filters are used. The filters could be passive, where inductive and capacitive elements are designed in such a way to resonate at a specific frequency corresponding to the frequency of the harmonic component to be filtered out. A major drawback for passive filters is their fixed range of harmonic compensation [7, 8]. Hence, came the need for a dynamic solution for harmonics.

To overcome the drawbacks of passive LC filters, and with the advancements in the power semiconductor industry, the use of active filters instead of passive filters in harmonic mitigation is becoming more prevalent [8]. Active filtering can be implemented through different configurations based on the connection to the system: i) Series active power filter, ii) Shunt active power filter, and iii) Hybrid active power filters. The series active filter is used to compensate the voltage harmonics through the series injection of voltage. The shunt active filter is connected in parallel with the source and used to compensate the current harmonics in the system. The hybrid active filter is the combination of a passive and an active filter [9].

1.2 Thesis Objective

The objective of this thesis is to analyze the energy consumption of the Louis-Hippolyte-La Fontaine Tunnel, and to design a Peak and Energy Shaving system using Battery Energy Storage Systems (BESS) in conjunction with Photovoltaic cells (PV) to reduce the constraints imposed on the grid from the tunnel. The system sizing is based on the expected electrical bill savings. The thesis also proposes a new control scheme for Voltage Source Inverters (VSI) used with peak shaving systems, that would allow the system not only to perform peak shaving but also allows the system to adopt the functions of active filters to mitigate the harmonic components

generated from the tunnel, and the functions of reactive power compensation and power factor correction capacitor banks.

1.3 Thesis Outline

The thesis is divided into five chapters. Chapter two analyzes the electrical power system of the Louis-Hippolyte-La Fontaine Tunnel followed by the load profile of the tunnel and the load profile breakdown, and the tariff structure. Chapter two also presents the design methodology for the peak shaving system and highlights the potential electrical bill savings, and shows the changes on the load profile after the application of the system. In chapter three, the proposed control scheme for the VSI is discussed in detail along with the methodology followed to reach the proposed scheme. Chapter four studies the operation and behavior of three phase induction motors and their electrical drives when operated from PV, this has the potential for use in the tunnel. The study is based on a case study comparing an experimental setup built in the laboratory with a simulation model in Simulink. Chapter five concludes the thesis and proposes future research work.

CHAPTER 2

Design and Control of a Peak Load Shaving System for the Louis-Hippolyte-La Fontaine Tunnel

2.1 Introduction

The Louis-Hippolyte-La Fontaine Tunnel in figure 2.1, is a part of the Trans-Canada Highway, connecting the island of Montreal with Longueuil at the south shore of the St. Lawrence River, Quebec. Along with the bridge, it is the longest underwater tunnel-bridge in Canada, at a length of 1.8 km [10]. The tunnel provides a major access point to the island of Montreal. It is estimated that 130,000 vehicles pass through the tunnel daily [11]. During the 1998 ice storm it was the only link between Montréal and the south shore, and is thus of strategic importance.

This chapter discusses the methodology used to reduce the constraints on the Hydro Quebec electrical power grid by reducing the peak load drawn by the Louis-Hippolyte-La Fontaine Tunnel. This is done by designing an energy storage system (ESS) to achieve peak shaving by means of battery energy storage systems, and photovoltaic cells in conjunction with battery energy storage system (BESS). The developed system is then validated using two softwares; the National Renewable Energy Laboratory's (NREL) system advisor model (SAM) and HOMER Pro by HOMER Energy.

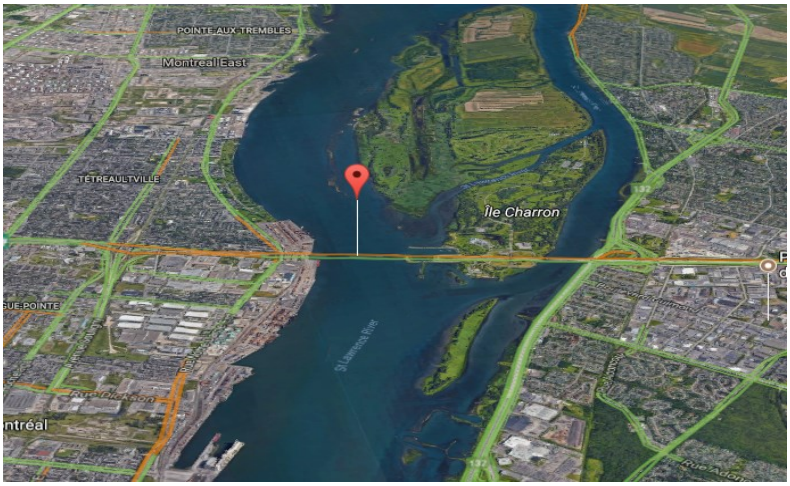

Figure 2.1 The Louis-Hippolyte-La Fontaine Tunnel aerial view, Google Maps [12].

2.2 Load Profile

This work is based on the load profile for the year 2015. The database provided by La Ministère des Transports, de la Mobilité durable et de l'Électrification des transports (MTMDET) includes the load measurements for the years of 2014, 2015, and 2016. However, years 2014 and 2016 recordings have some gaps. Therefore, the load profile taken as the base is the load of the year 2015. Figure 2.2 shows the load profile for the year 2015 in p.u the base is not disclosed due to confidentiality agreement signed with La Ministère des Transports, de la Mobilité durable et de l'Électrification des transports (MTMDET). The load profile is the load measurements recorded every 15 minutes, figure 2.3 shows the load profile breakdown.

As seen from figure 2.2, the load dynamically changes with time, peaking during winter months to reach the highest peak recorded in the year, namely February 24th at a peak of almost 2 p.u. The power drawn from the grid reduces gradually during the months of spring and summer, and the load falls in a range between 0.85-0.9 p.u.

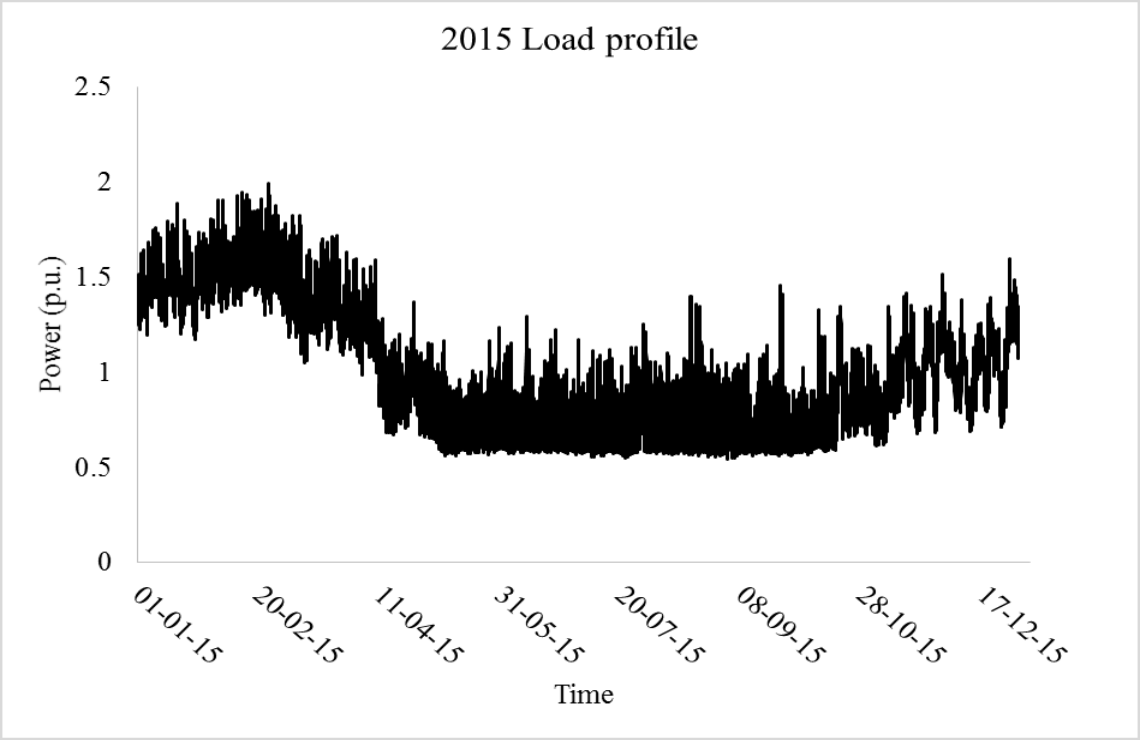

Figure 2.2 Load profile of the year 2015.

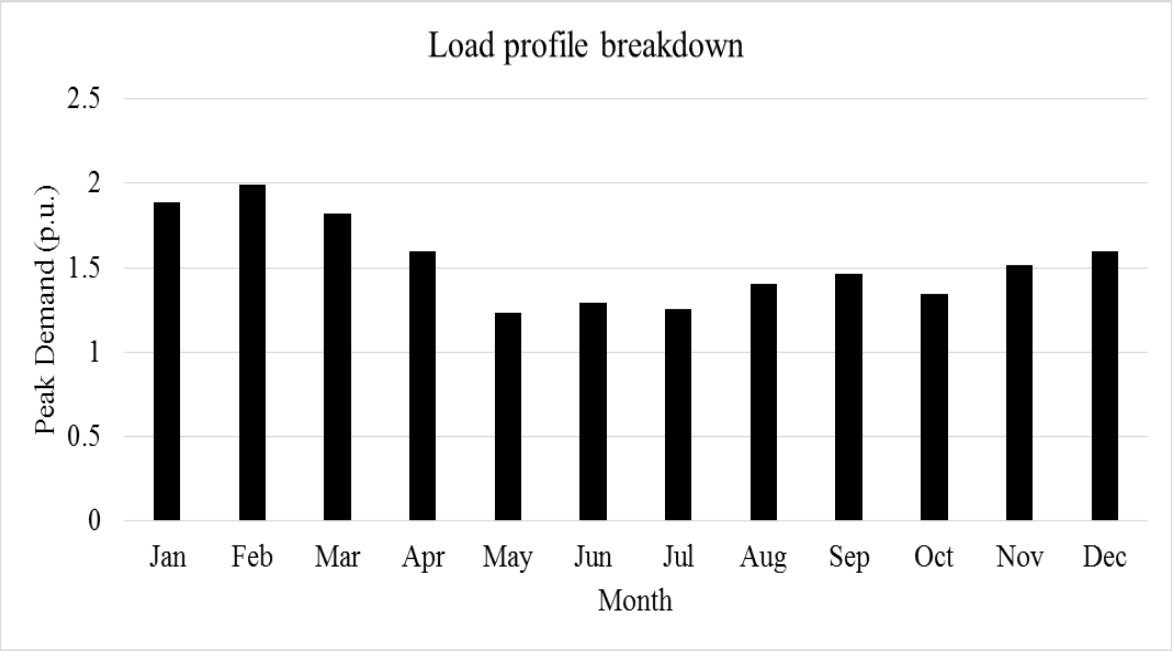

Figure 2.3 Load profile breakdown.

It can be seen from the load profile breakdown in figure 2.3, that there is a significant difference between the peak power drawn in winter and summer. Therefore, designing a peak shaving system to reduce the gap is justified.

2.3 Tariff Structure

The electrical consumption of the Louis-Hippolyte-Lafontaine Tunnel places the tunnel under the Hydro Quebec Rate M structure. General Rate M applies to a medium-power contract whose maximum power demand has been at least 50 kilowatts during a consumption period included in the 12 consecutive monthly periods ending at the end of the consumption period in question [2].

Table 2.1 Hydro Quebec rate M tariff structure.

Fixed monthly charge	36.99 $
Peak demand	14.43 $/kW

	The minimum demand is 65% of the max demand in the last 12 months
Energy rate	4.97 ₵/kWh first 210,000 kWh
	3.69 ₵/kWh remaining kWh

From table 2.1, one can conclude that the billing structure of the Louis-Hippolyte-La Fontaine Tunnel is composed of three components:

i) **Fixed monthly charge:** this charge does not depend on the consumption and is always fixed for all facilities under the application of the rate M tariff structure.

ii) **Energy Usage:** which is how much energy (in kilo Watt hour (kWh)) is consumed by the tunnel during the billing cycle in question. Rate M structure for energy usage is not based on the Time of Use (TOU). The time of use tariff structures offer different rates for different time periods of the day [13], whereas in rate M tariff structure, the rate is different only for the first 210,000 kWh, and the remaining consumption is subjected to a fixed rate regardless of the time of the consumption.

iii) **Peak Demand:** which is the maximum power drawn from Hydro Quebec by the tunnel in the billing cycle (in kilo Watt). The recordings are usually taken as average values of 5, 10, or 15 minutes [3, 14].

Tariff structures based on the Time of Use (TOU) are more beneficial for peak shaving applications that utilize renewable energy resources, especially, photovoltaics cells where the PV generation normally peaks around the same time when the load on the grid peaks. Therefore, more electrical bill savings are expected [14]. The peak demand component usually forms a considerable portion of the total bill and is used to force clients not to have high load peaks in order to reduce stress on the grid [3, 15].

Applying the tariff structure in table 2.1 on the load profile in figure 2.2 results in the electrical bill of the year 2015, in figure 2.4. The two components of the electrical bill are shown as a percentage of the monthly bill of the month in question. Seen from figure 2.4, the demand charges contribute to a maximum of 48.7% of the monthly bill for the month of September, and a

minimum value of 38.8% for the month of January. This highlights the potential of electrical bill savings to be expected from implementing a peak shaving system.

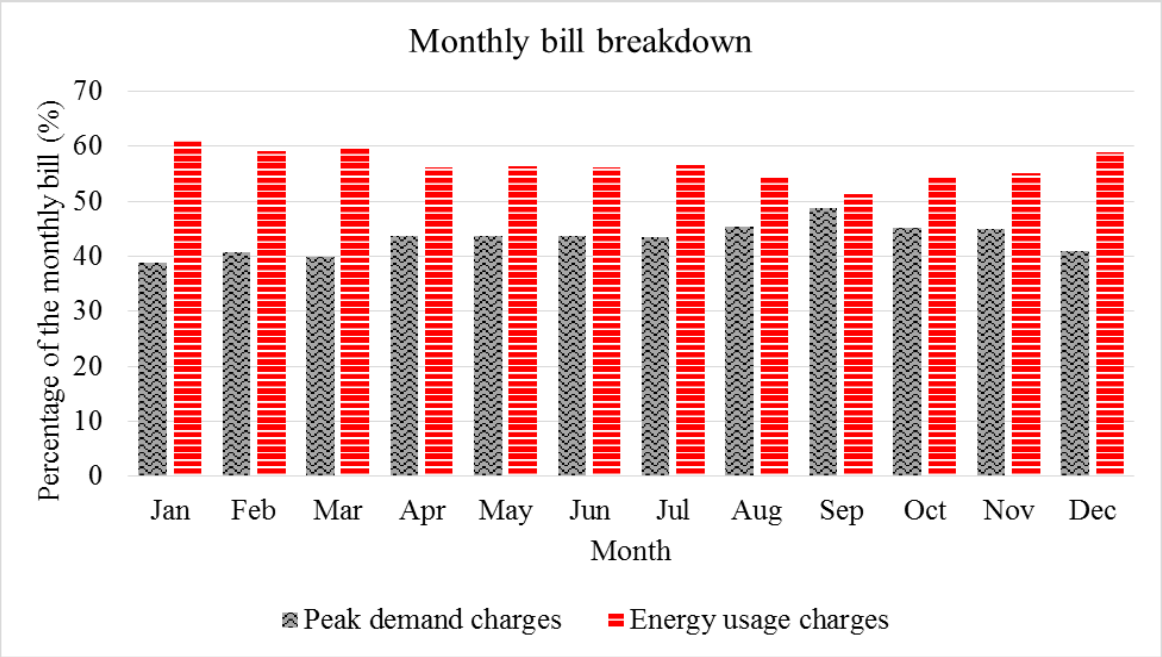

Figure 2.4 2015 Electrical bill breakdown.

2.4 Peak Load Shaving

High-stress levels and expensive peak demand charges have driven both utilities and clients to heavily invest in energy storage systems (ESS) for load leveling, peak shifting, and peak shaving. Due to the potential financial benefits of reducing the peak demand, peak shaving has usually been the preferred practice.

On-site generator sets and gas turbines alongside energy management and load scheduling are used as techniques for peak shaving [1, 15, 16]. However, in the last decade Battery Energy Storage Systems (BESS) have become more viable due to their versatility, scalability and fast response time [17]. The batteries are charged during off-peak hours, the energy stored is then discharged during peak load hours reducing power drawn from the grid, hence reducing the peak demand charges [1]. Both the customer and the utility benefit from peak load reduction. The customer would reduce the monthly electrical bill and with that comes the potential financial benefits. On the other hand, the grid would have lower stress levels during peak load hours.

Renewable energy resources are also used for peak shaving, nonetheless, the variable and fluctuating nature of renewable energy generation poses difficulties to ensure the reliability of the supply. High penetration levels of renewable energy generation into the power system compromises both the stability and reliability of the power system, as power generation and power demand must be balanced at all times [17, 18]. For these reasons, energy storage systems (ESS) have been considered.

2.5 Design Methodology

The basic idea of peak shaving is to limit the power drawn from the grid to a certain level, this level is referred to in this chapter as the shave line (Pshave). Selecting the technique to establish the shave line is influenced by the nature of the load. For example, in [3] peak shaving techniques for data centers include workload modulation, in which some tasks are simply delayed or dropped during peak hours. This technique might cause performance degradation, whereas in the case of the Louis-Hippolyte-La Fontaine Tunnel that is not acceptable due to the high safety and operation standards.

An electrical model processes the load profile and implements daily peak shaving for two cases; the first case only using battery energy storage systems, and the second case using photovoltaics cells PVs in conjunction with Battery Energy Storage Systems (BESS). An economic model processes the load profile after peak shaving and implements the Hydro Quebec tariff structure to calculate the expected electrical bill savings, which reflect the financial benefits. Based on the expected savings, the economic model returns the net present value of the system (NPV) [19], internal rate of return (IRR) [20], and the discounted payback period [21]. These economic factors then facilitate the decision-making in the selection of the BESS size.

2.5.1 Electrical Model

The electrical model analyzes the load profile for each day and searches for a shave line value (P_{shave}), such that for power measurements greater than the shave level ($P_{measure} > P_{shave}$), the energy between the measurements and the suggested shave line ($E_{Discharge}$ discharge energy) is equal to the usable energy from the battery energy storage system (E_{BESS}).

$$E_{Discharge} = \int_{t_0}^{t_1} (P_{measure} - P_{shave}) \cdot dt \qquad (2.1)$$

For power measurements less than the shave level ($P_{measure} < P_{shave}$), the energy between the suggested shave line and the measurements (E_{Charge} charge energy) is at least equal to the discharged energy from the battery energy storage system.

$$E_{Charge} = \int_{t_1}^{t_2} (P_{shave} - P_{measure}) \cdot dt \qquad (2.2)$$

$$E_{BESS} = E_{Discharge} = E_{Charge} \qquad (2.3)$$

Figure 2.5 shows a load profile for a day, highlighting the shave line (P_{shave}), and the resulting discharge and charge energies. The electrical model processes two inputs; the load profile and the desired battery energy storage system size. The electrical model then produces a new load profile for each BESS size after the peak shaving.

The first case implemented is the use of different BESS sizes to achieve peak shaving. The BESS considered in this work is a lithium-ion (Li-ion) based energy storage system. Li-ion batteries are the most widely used batteries for peak shaving applications due to their high energy density and high efficiency [22]. The second case utilizes a photovoltaic solar farm in conjunction with different BESS sizes to shave the load peaks.

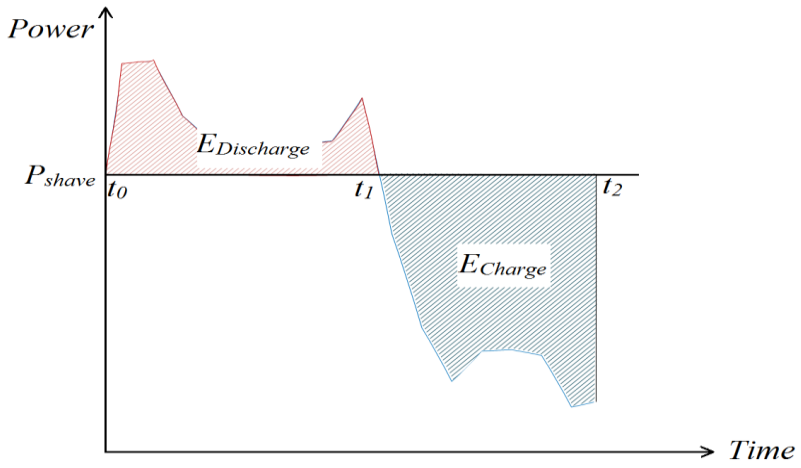

Figure 2.5 A typical day load profile showing the shave line level, discharge and charge energies.

The electrical model then produces the expected load profile, then compares the peak load before and after the system to determine the reduction in the power drawn from the grid.

2.5.2 Economic Model

Introducing BESS into the power system of the Louis-Hippolyte-La Fontaine Tunnel will result in electrical bill reduction. Larger energy storage systems produce higher reduction. However, higher running and maintenance costs are expected for large energy storage systems. The economic model applies the utility tariff on the new load profile obtained from the electrical model and calculates the expected electrical bill reduction.

The economic model assumes a 5% interest rate, 0.6% inflation rate, and a 5.63% nominal discount rate. The expected lifetime of the project is 25 years. All amounts in this paper are in Canadian dollars. The model calculates the following factors:

- Net Present Value (NPV):

The NPV of an investment with an expected lifetime of N years, and has an initial cost of C_0, a cash flow of C_n in year n, and a nominal discount rate of i, is calculated using equation 2.4. An investment with a positive NPV indicates that the expected revenues produced exceed the designed initial cost of capital. A negative NPV suggests that the investment will lead to a net loss [19].

$$NPV = \sum_{n=1}^{n=N} \frac{C_n}{(1+i)^n} - C_0 \qquad (2.4)$$

- Internal Rate of Return (IRR):

The internal rate of return is defined as the interest rate at which the net present value of an investment equals zero. A net present value of zero indicates that the expected returns from an investment and the designed initial cost of capital are equal, the investment returns the initial cost of capital without any profit [20].

- Payback Period:

Payback period is the number of years required to recover the initial expenditures of an investment. In the utilized model the time value of money is ignored [21].

2.5.3 Designed Initial Cost of Capital

The cost of Li-ion batteries has dropped by an average of 23% per year from 2010 to 2015 [23]. In [24], it is projected that the cost reduction of Li-ion batteries will continue. In a study by the National Renewable Energy Laboratory (NREL) in 2016, reports of installed cost benchmarks in the U.S. estimate the price of energy from Li-ion batteries by comparing four different installations of different sizes. The comparison reflects the different prices on a standardized system size. The study concluded that the price of BESS ranges from 450$ to 630$ per kWh [23].

The cost of solar photovoltaics benchmarks is studied in [25], the study reveals that the solar deployment growth in the United States has increased dramatically in the past five years. The residential sector, commercial sector, and utility scale installations have grown by 46%, 43%, and 101%, respectively. Meanwhile, PV systems costs have declined rapidly. The study estimates the cost to range from 1,100$ to 1,700$ per kW. This includes the installation costs, hardware costs, module, and the inverter. This article considers the price of BESS to be 504$/kWh with an expected lifetime of 25 years based on lifetime estimations in [18], and 1,300$/kW for the PV system. The maintenance and operation costs are considered 20$/kW-year based on a study in [26].

2.6 Results

2.6.1 Peak Shaving with Battery Energy Storage System (BESS)

This study shows that the application of BESS to the Louis-Hippolyte-La Fontaine Tunnel for peak shaving will lead to financial benefits in the form of electrical bill reduction. The optimal size of the BESS is determined based on the outputs of the economic model. The search process for the optimal BESS size is done by studying the impact of different sizes of BESS, starting from 100 kWh up to 1000 kWh, on the tunnel's electrical power system using MATLAB. The same sizes are also simulated using the National Renewable Energy Laboratory's (NREL) system advisor model (SAM), and HOMER Pro by HOMER Energy.

The system advisor model (SAM) has the capability for peak shaving. However, one can't specify the desired power level, or the control strategy for the BESS. On the other hand, HOMER Pro allows one to specify the desired power peaks for each month. The developed MATLAB model

calculates the shave line for each day based on the battery full capacity, the instantaneous state of charge of the system, and the maximum depth of discharge.

Examining a load profile of one day, and applying the three models (SAM, HOMER Pro, and MATLAB) will result in a new load profile for that day. The new load profile for the day in question is shown in figure 2.6. It can be seen that the system advisor model (SAM) has the highest load peak compared with the other two models. This suggests lower estimations for the expected reduction in the electrical bill compared with the other two models. The developed MATLAB model and HOMER Pro almost produce the same shave level, but higher energy consumption results from HOMER, hence, higher electrical bill reduction is expected from the MATLAB model. Figure 2.7 shows the expected electrical bill reduction, as stated above, the developed MATLAB model estimates higher reduction. The expected electrical bill savings increase as the system size increases, simultaneously, the system costs increase. The net present value for each battery size is then calculated and shown in figure 2.8.

The system advisor model estimates lower financial benefits and hence a smaller range of BESS sizes, SAM estimates positive net present values for BESS sizes from 100 kWh up to 350 kWh, whereas, the developed MATLAB model and HOMER pro model agree on positive NPV for BESS sizes from 100 kWh to 400 kWh. The difference between the three sizes is 50 kWh, and for commercial customers with high power demand, this difference is not significant.

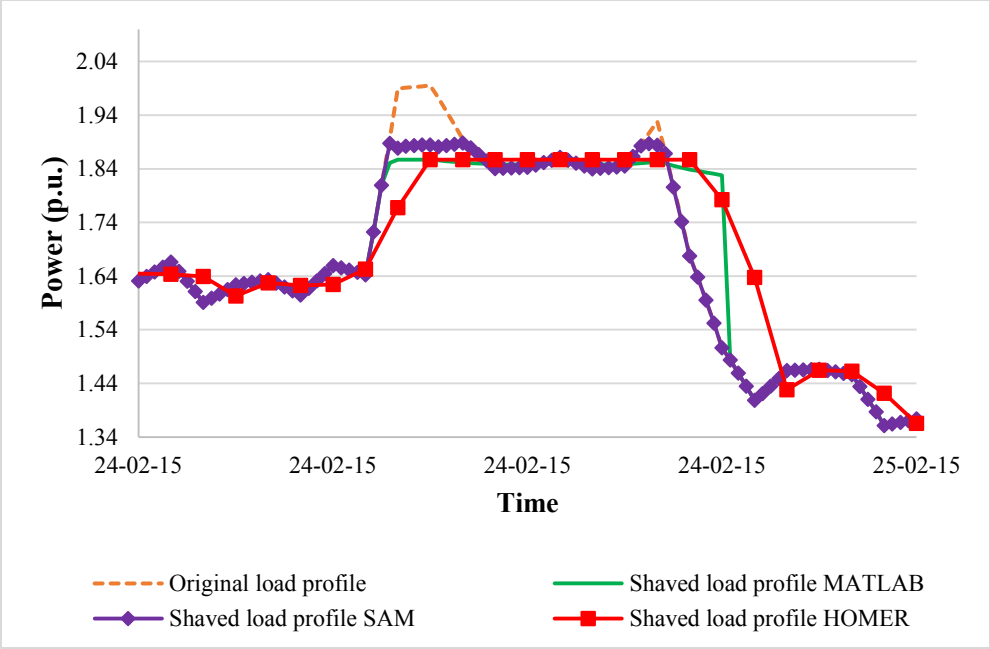

Figure 2.6 Original load profile versus the shaved load profile after the BESS produced from the MATLAB model, SAM, and HOMER Pro, respectively.

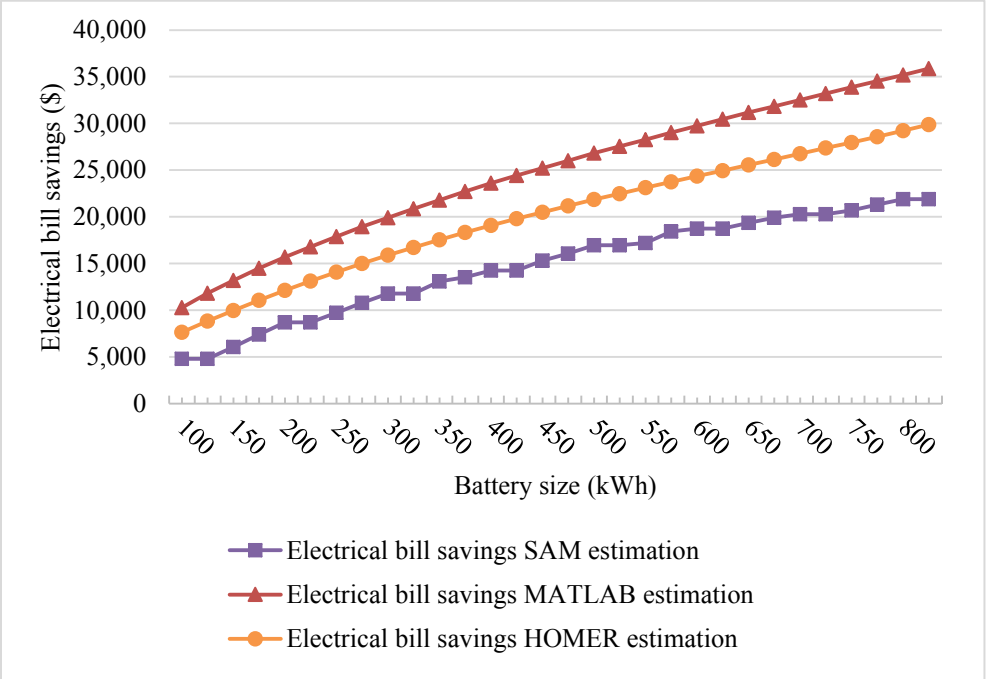

Figure 2.7 Expected electrical bill reduction produced from the application of BESS: The MATLAB model, SAM, and HOMER Pro, respectively.

Figure 2.9 shows the expected payback periods estimated by the models. SAM estimates longer payback periods, while the developed MATLAB model and HOMER estimations are closer, with shorter payback periods estimated by the MATLAB model.

The selection process for the BESS is based on the desired outcome from the system. For instance, if the expected financial benefits is to be targeted, the battery with the highest expected benefits and a positive NPV should be selected. The analysis is focused on the BESS selection based on the system that achieves more peak shaving, and therefore, reduce the stress on the grid as much as possible. Table 2.2 shows selected BESS sizes based on the results of the three models. The expected load profile after the application of BESS is shown in figure 2.10.

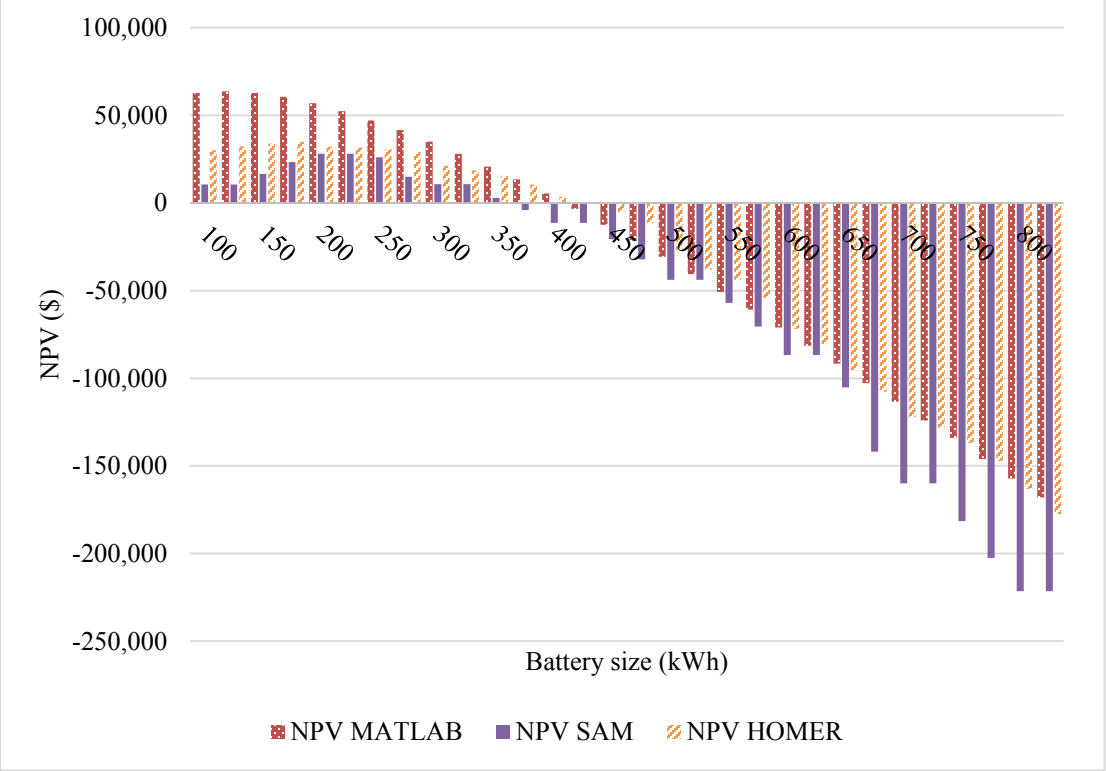

Figure 2.8 Expected net present values for each battery size estimated from the MATLAB model, SAM, and Homer Pro.

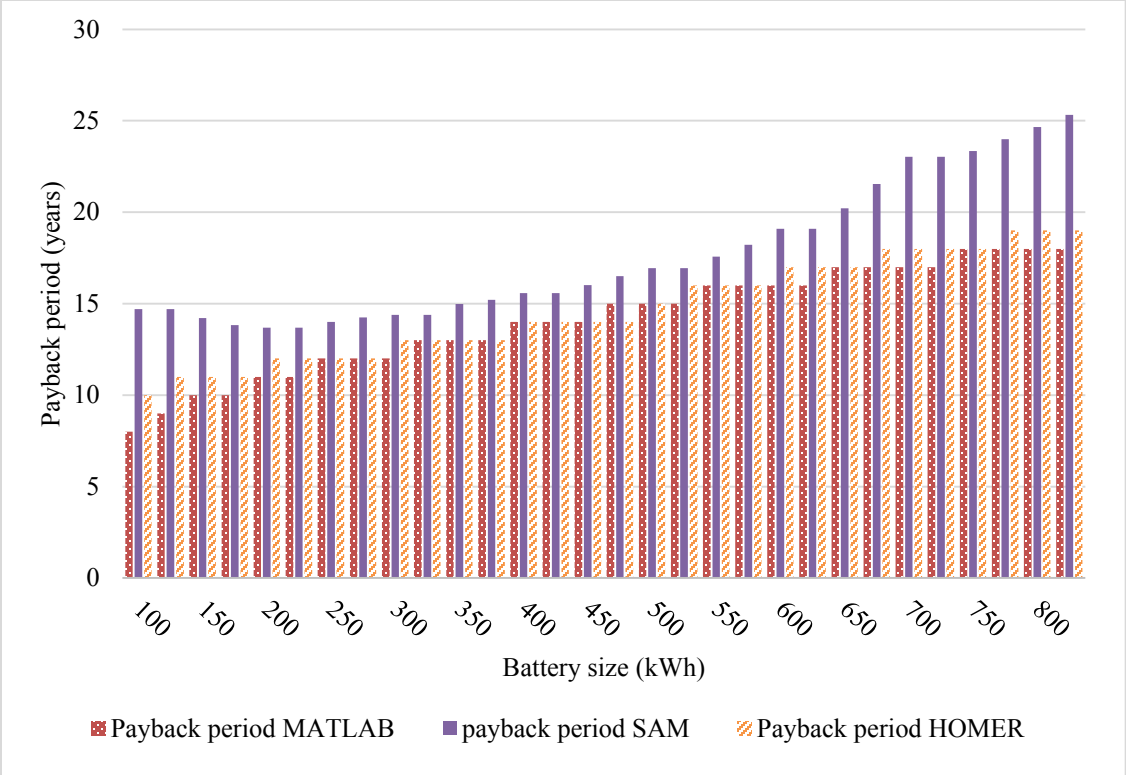

Figure 2.9 Payback periods estimations by the models.

Table 2.2 The economic sizes for the BESS.

Model	BESS size (kWh)	Expected electrical bill reduction ($)	NPV ($)	IRR (%)	Payback period (years)
MATLAB	400	23,590.97	5,438.78	5.8	14
HOMER	400	19,067.44	3,710.15	5.77	14
SAM	350	13,081.80	2,855.39	N/A	15

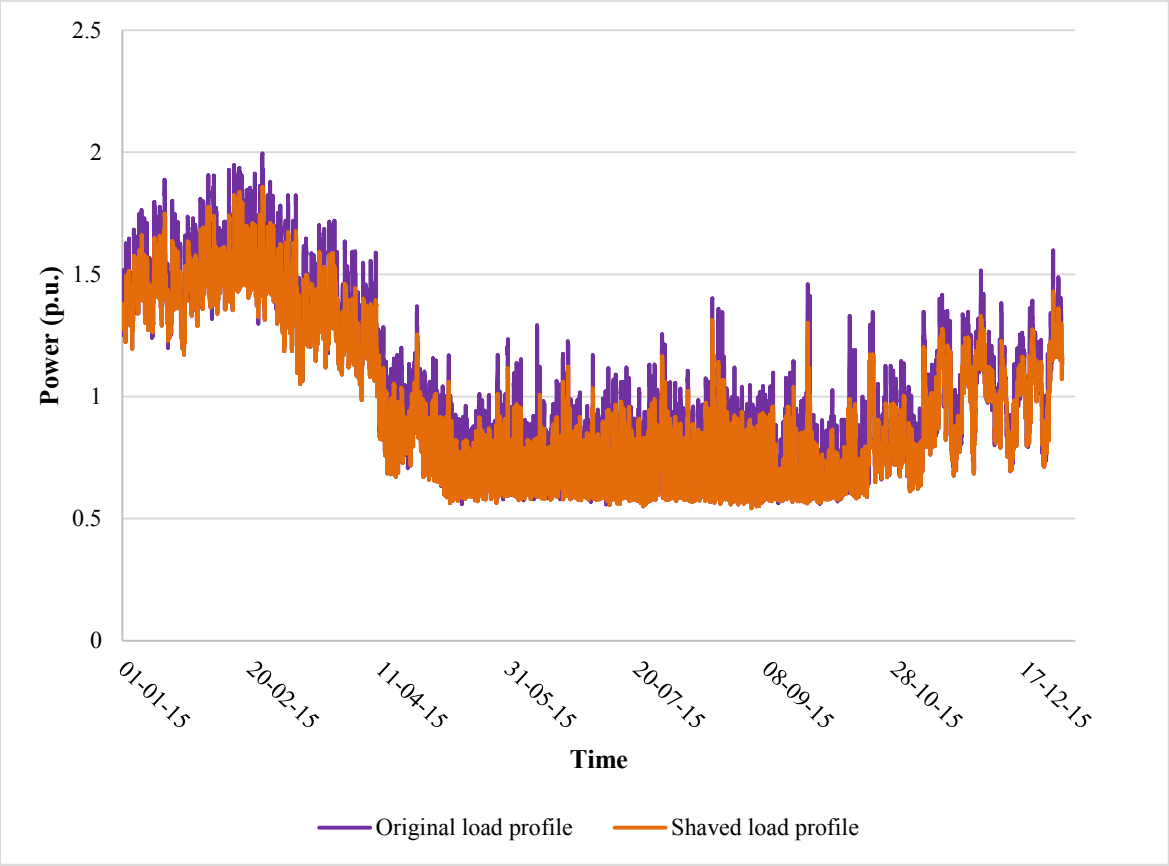

Figure 2.10 Load profiles before and after the economically sized BESS, for year 2015.

2.6.2 Peak Shaving with Photovoltaics and Battery Energy Storage System (PV and BESS)

The photovoltaics solar farm is introduced to the system and the same analysis procedure is implemented. The resulting load profiles from the three models are depicted in figure 2.11. The system advisor model has the highest peak, and hence, the expected electrical bill reduction is less than the other two models. Figure 2.12 shows the expected electrical bill reduction estimated by the three models, SAM has a lower estimation, whereas the developed MATLAB model and HOMER model estimations are in good agreement. In the case of only BESS, the HOMER model utilizes higher energy due to the losses of the BESS. However, with the introduction of photovoltaics to the system, the mismatch in the electrical bill estimations due to the consumed energy component is reduced. Therefore, the two models estimations are close.

The NPV of the systems are calculated and shown in figure 2.13. The developed MATLAB model, and HOMER model estimate a positive NPV for battery sizes from 100 kWh up to 725 kWh, while SAM estimates a positive NPV for battery sizes up to 650 kWh. In this case, the size difference is 75 kWh. Figure 2.14 shows the expected payback periods estimated by the three models. SAM estimates longer payback periods, while the developed MATLAB model and HOMER estimate the same payback period for the same battery sizes.

Reducing the stress on the grid also dictates the size selection decision for this case. Table 2.3 shows selected BESS sizes based on the results of the three models. The expected load profile after the application of BESS in conjunction with PVs is shown in figure 2.15.

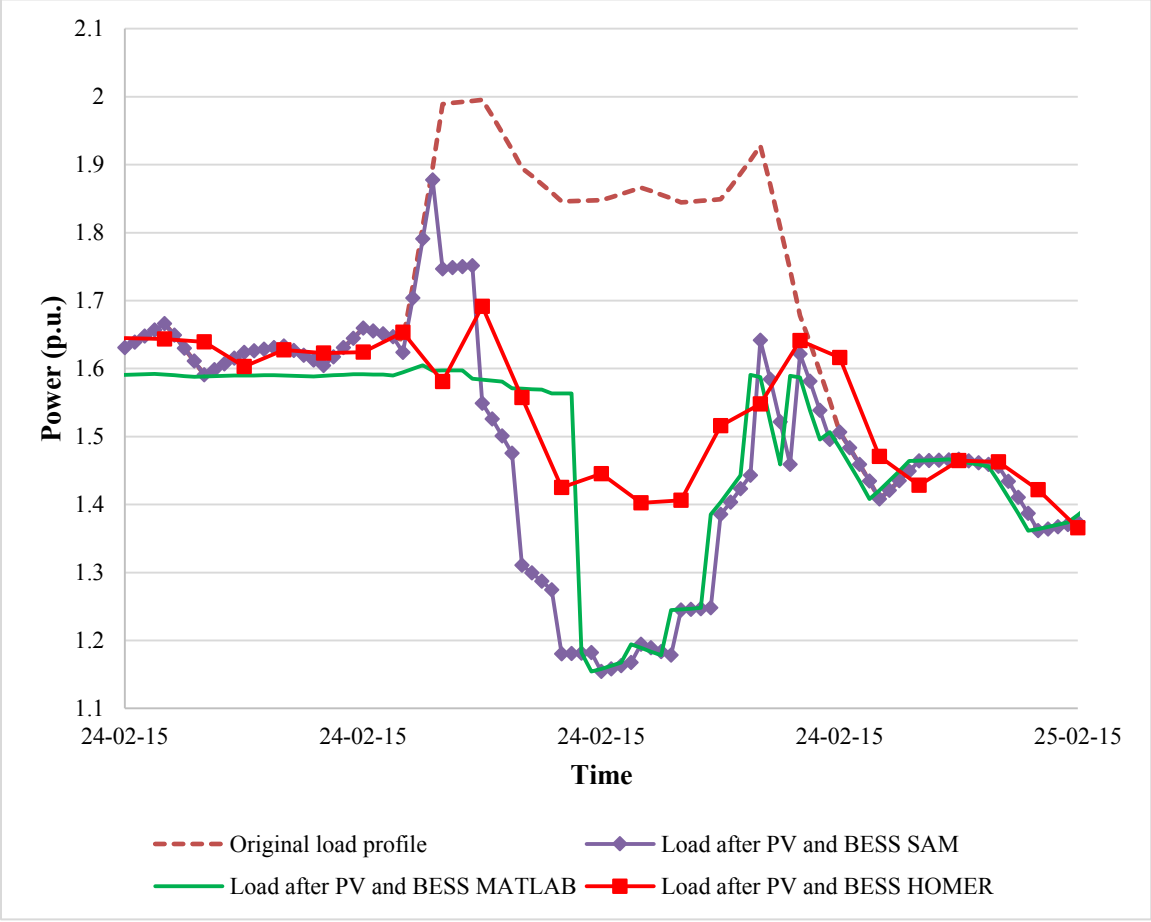

Figure 2.11 Original load profile versus the shaved load profile after the PV and BESS produced from the MATLAB model, SAM, and HOMER Pro, respectively.

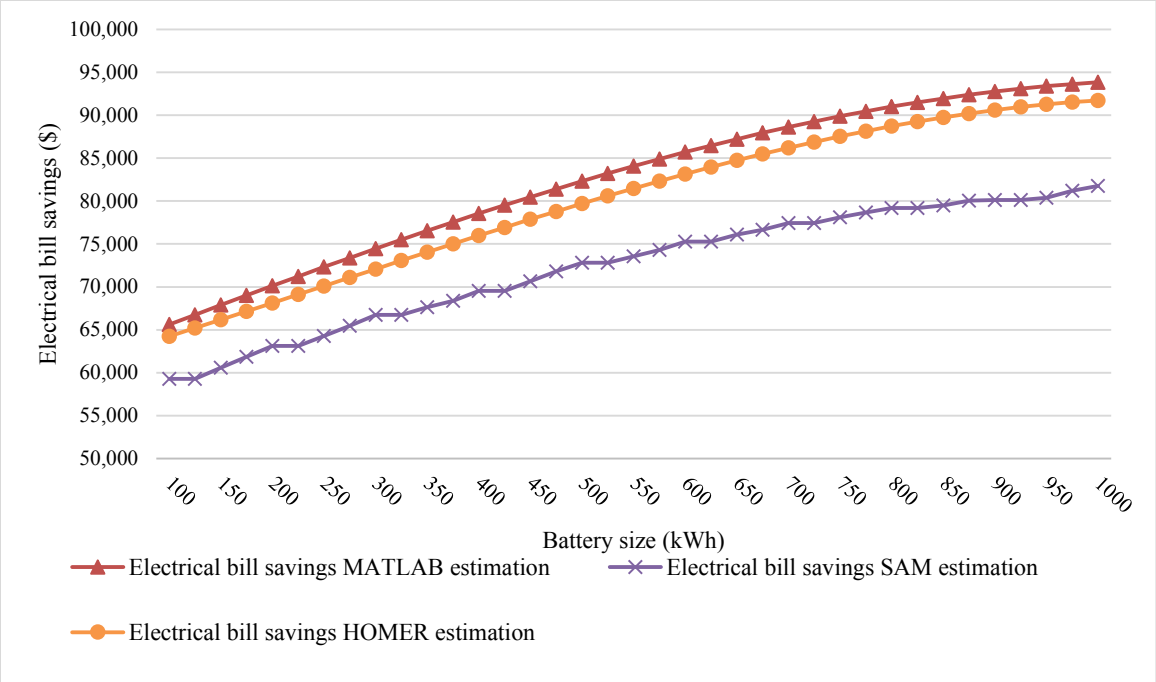

Figure 2.12 Expected electrical bill reduction produced from the application of BESS and PV MATLAB model, SAM, and HOMER Pro, respectively.

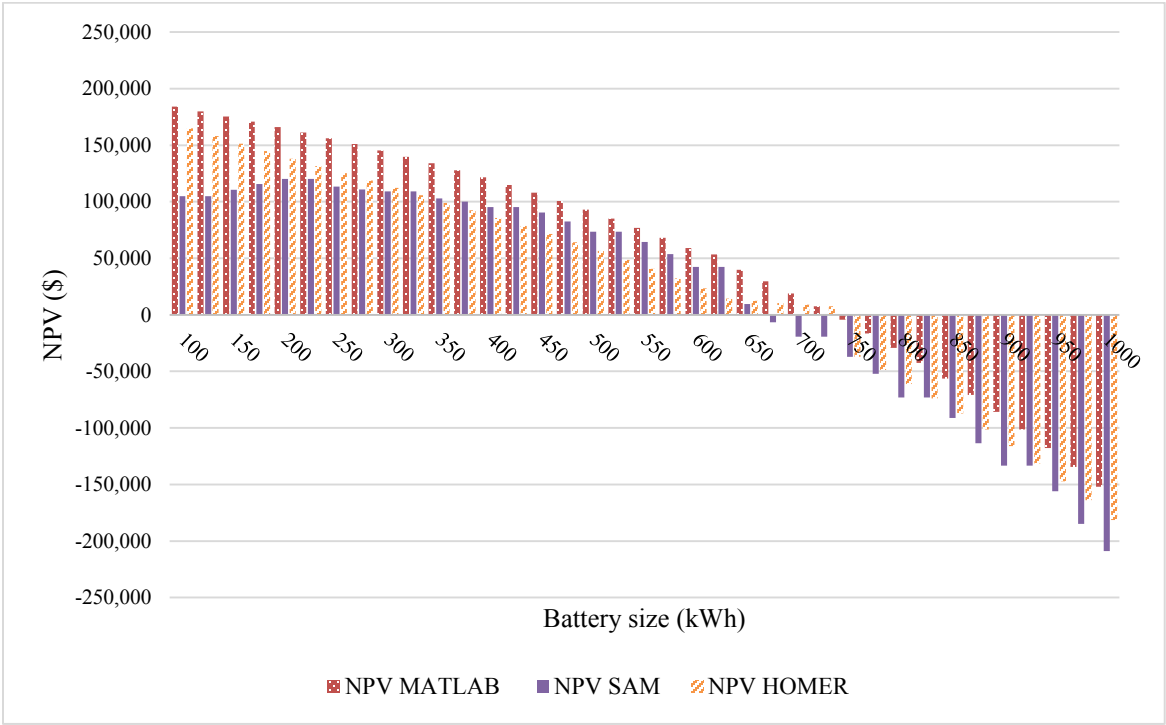

Figure 2.13 Expected net present values for each battery size estimated from the MATLAB model, SAM, and HOMER Pro.

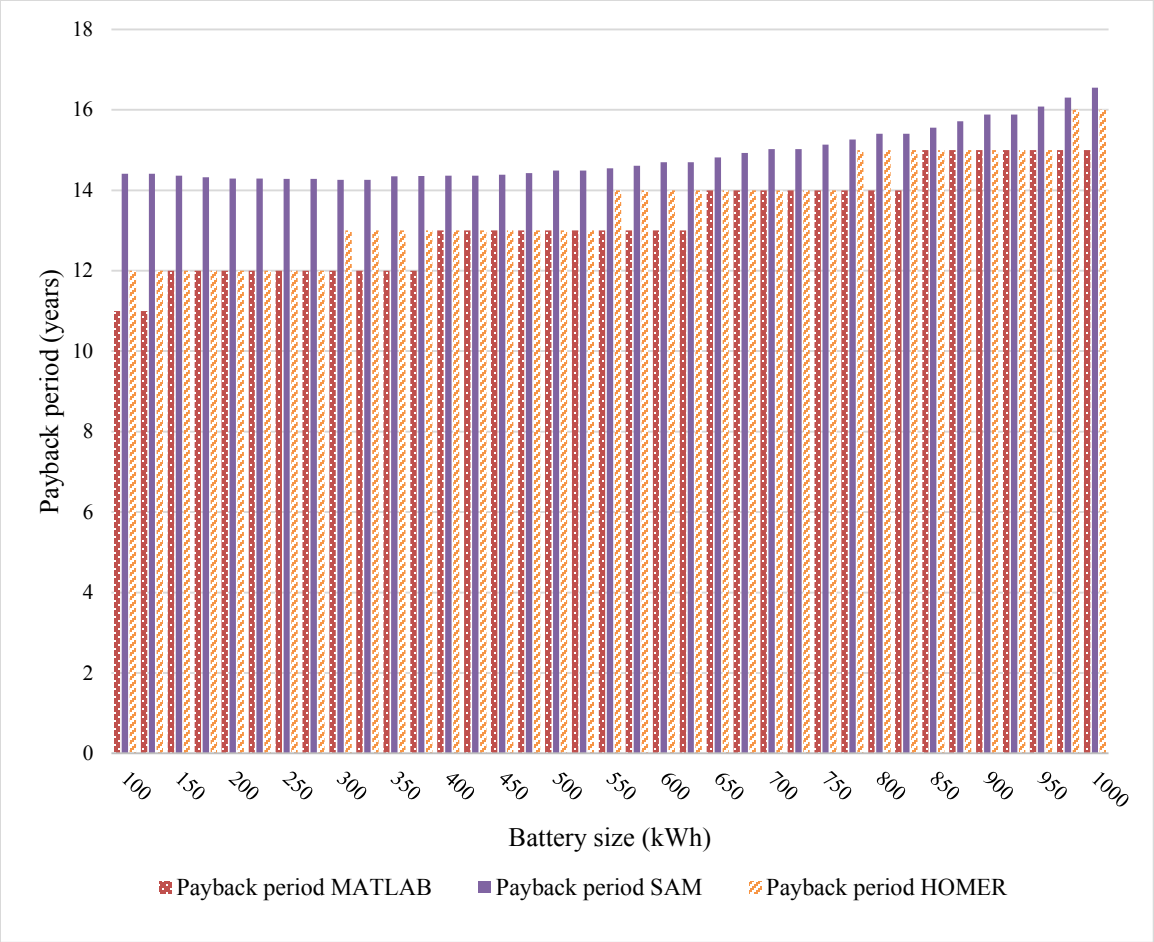

Figure 2.14 Payback periods estimations by the models.

Table 2.3 The economic sizes for the BESS in conjunction with PV.

Model	BESS size (kWh)	Expected electrical bill reduction ($)	NPV ($)	IRR (%)	Payback period (years)
MATLAB	725	89,262.09	7,521.89	5.69	14
HOMER	725	86,878.12	6,416.24	5.68	14
SAM	650	76,101.10	9,516.82	N/A	15

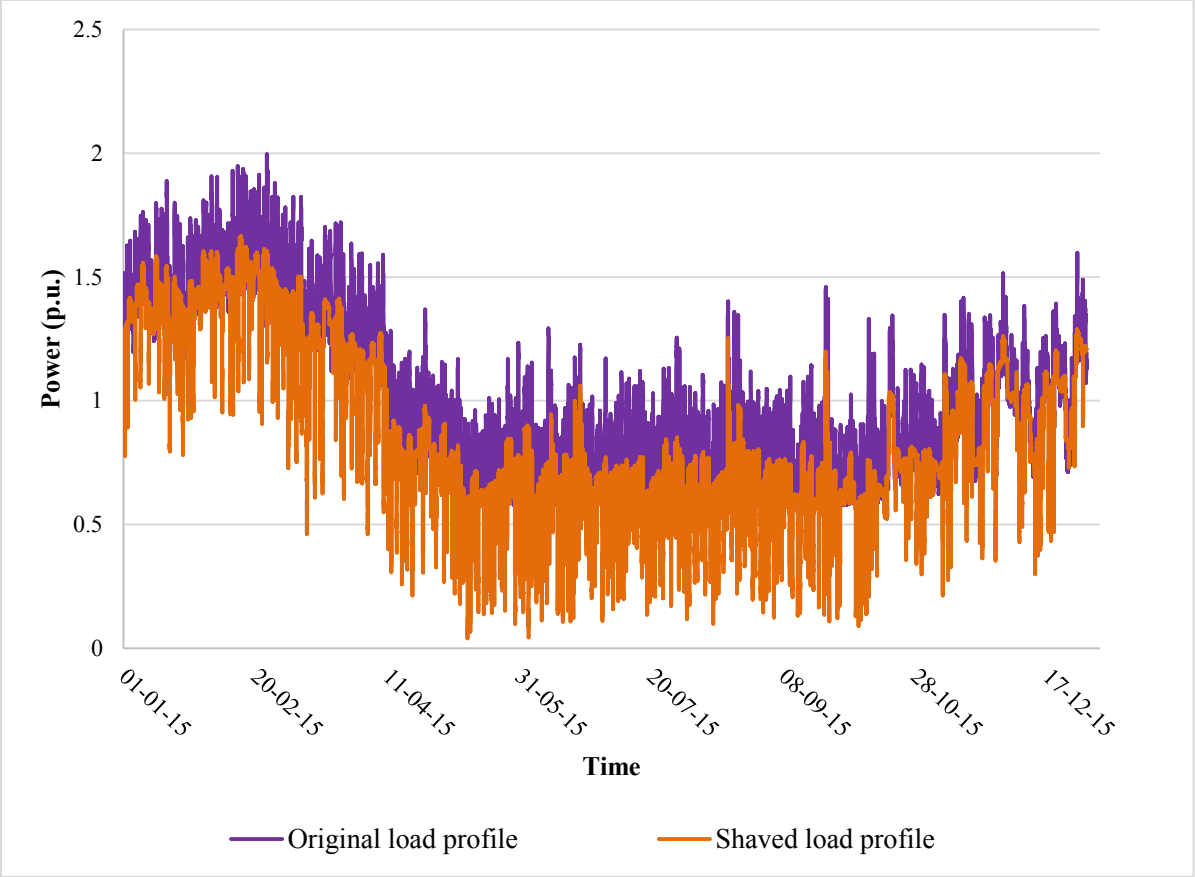

Figure 2.15 Load profiles before and after the PV and the economically sized BESS, for year 2015.

2.7 Discussion

The expected load profiles in figures 2.10 and 2.15 show the impact of the developed system on the grid compared with the original load profile, this impact is broken down in figure 2.16, where the peak load produced by the two modelled systems are shown for the year 2015.

The month of February has the highest peak load at about almost 2 p.u., using BESS reduces the peak power to 1.86 p.u. which is around 7% reduction, while utilizing PV in conjunction with BESS limits the peak to 1.66 p.u., which is a 16.58% reduction in the power drawn from the grid.

The month of July is when the PV panels have the highest generation, and as a result the system utilizing PV cells reduces the power from the grid to 0.85 p.u compared with the original

1.25 p.u, which is a 32% reduction, whereas, using BESS reduces the peak power to 1.16 p.u. which is around 7.26% reduction. Tables 2.4 and 2.5 show the comparison between the peak demand before and after the application of both systems.

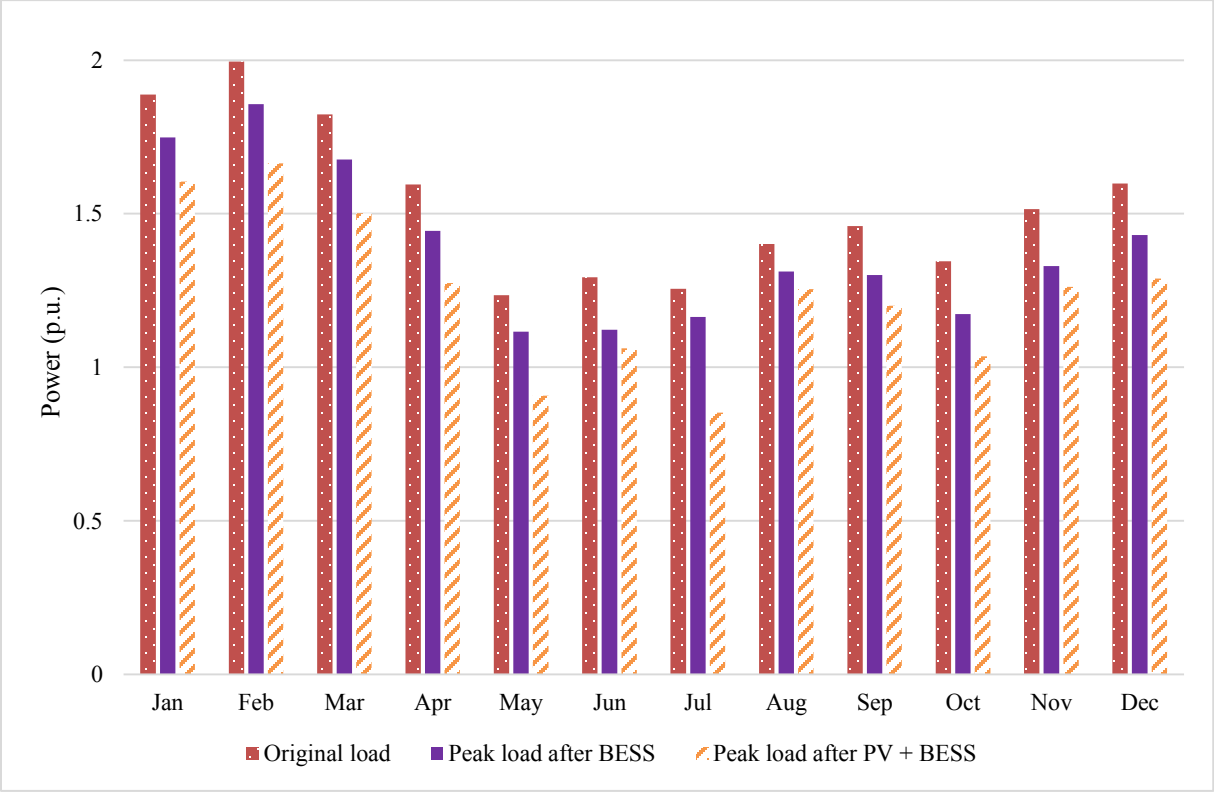

Figure 2.16 Load peaks drawn from HQ before and after the BESS, and BESS in conjunction with PV, respectively.

Table 2.4 Peak demand before and after the application of BESS.

Month	Original peak demand (p.u.)	Peak demand after the BEE (p.u.)	Peak reduction (%)
January	1.888	1.749	7.363
February	1.995	1.857	6.931
March	1.824	1.677	8.072
April	1.595	1.445	9.449
May	1.235	1.116	9.625
June	1.293	1.122	13.202
July	1.256	1.164	7.264
August	1.401	1.312	6.356
September	1.460	1.300	10.916

October	1.345	1.173	12.784
November	1.515	1.329	12.289
December	1.598	1.431	10.471

Table 2.5 Peak demand before and after the application of BESS in conjunction with PV.

Month	Original peak demand (p.u.)	Peak demand after the BEE (p.u.)	Peak reduction (%)
January	1.888	1.604	15.006
February	1.995	1.664	16.584
March	1.824	1.502	17.662
April	1.595	1.275	20.095
May	1.235	0.908	26.486
June	1.293	1.062	17.869
July	1.256	0.853	32.098
August	1.401	1.254	10.489
September	1.460	1.200	17.785
October	1.345	1.036	22.959
November	1.515	1.261	16.758
December	1.598	1.288	19.367

2.8 Summary

This chapter proposes an economic design and control of an energy storage system for peak load shaving of the Louis-Hippolyte-La Fontaine Tunnel to reduce the constraints imposed on the Hydro Quebec grid. The developed MATLAB model finds the shave level based on the capacity of the selected battery energy storage system BESS, and the instantaneous state of charge of the system. The modelled systems reduce the power drawn from the grid and therefore, reducing the stress imposed on the grid. The expected financial benefits from the developed system are compared with NREL's system advisor model (SAM) and HOMER Pro. The comparison showed the accuracy of the developed control strategy. The developed MATLAB model produced the same BESS size as HOMER Pro.

CHAPTER 3

Control of Voltage Source Inverters in Peak Shaving Applications

3.1 Introduction

This chapter presents a control scheme for Voltage Source Inverters (VSI) used in peak shaving applications. The presented control first allows the VSI to interface peak shaving systems with the grid reducing stress levels imposed on the grid. Secondly, they play the role of power factor correction banks for reactive power compensation. And finally, they inherit the capabilities of active harmonic filters and harmonic mitigation techniques to suppress the harmonic content in the line current.

The stress levels on the electrical power grids and power quality issues have encouraged consumers to invest in peak shaving systems. Renewable energy resources, on-site diesel power generation, and load management and scheduling are all techniques used for peak shaving [1, 15, 16]. In the past decade, Battery Energy Storage Systems (BESS) have gained more attention as a technique for peak shaving due to their flexibility and fast response time [17]. BESS are used to store energy from the grid during off-peak hours and discharge it back to the load during peak demand hours to reduce the amount of power drawn from the grid.

The conversion of power -from and to the DC side- is done by means of power electronic circuitry. This conversion creates voltage and current harmonics depending on the control scheme used to control the operation of the power electronic system. Furthermore, the growing presence of non-linear loads such as Variable Frequency Drives (VFD), high switching frequency devices and Uninterruptible Power System (UPS) tends to increase the impact of the current and voltage harmonics on the overall power quality of the system [6], and if not treated, these harmonics could be very harmful to both the electrical utility and the consumer.

To mitigate the effect of line current harmonics, the simplest solution involves the use of passive filters. The single-tuned shunt connected passive filter is used to filter out specific harmonic frequencies [5]. However, the use of passive elements presents some limitation regarding

the fixed range of compensation, and the possibility of creating resonance condition [7, 8]. Furthermore, static VAR compensators (SVCs) have been considered to mitigate the harmonic effects on the system. However, they tend to generate low-order harmonics. In addition, their longer response time might not be suitable for fast-fluctuating load [6].

In power systems, controlling the flow of reactive power is imperative to ensure the proper operation of the power system. For instance, in power transmission and distribution systems, the flow of reactive power increases the power losses in the lines and degrades the power factor of the overall system and hence the power transfer capability is reduced [27].

The application of capacitor banks to compensate the flow of reactive power is valid, but it has many disadvantages; first, introducing capacitive elements into an inductive power system causes the amplification of certain order harmonics in line current harmonics due to the parallel resonance phenomena [5]. Under resonance conditions, the parallel impedance between the capacitor banks and the system inductance is less than the system's impedance, and therefore, high currents flow through the capacitor bank shortening the lifetime of the capacitors [28]. Secondly, the load is changing dynamically with time, and the capacitor banks only produce a fixed amount of reactive power into the system. Therefore, the use of active dynamic compensators is preferable to the use of fixed capacitor banks.

Unity Power Factor Converter (UPFC), Static Compensators (STATCOMs), and active filters could all be used as dynamic reactive power compensators [29]. The basic structure of these devices is a DC bus component, usually a capacitor, and an inverter to interface the DC side of the device with the AC side of the power system. However, the major difference is the control used to generate the references needed to achieve the required function.

3.2 Methodology

The presented analysis in this chapter assumes that a peak shaving system already exists and the VSI is connected in parallel with the load. The proposed control strategy is based on generating the required current references for peak shaving, active power filtering, and power factor correction to be injected by the VSI into the network. The references for each function are generated separately, and then added together and fed to a Hysteresis Current Controller (HCC) to generate the gating signals for the VSI.

3.2.1 Peak Shaving Control Module

The basic concept of peak shaving is to reduce the power drawn from the grid during peak load hours to a certain level (P_{shave}), either by generating power locally (from diesel generator sets or from photovoltaic cells), or by storing power from the grid during off peak hours using for example BESS and discharging it back during peak hours.

The peak shaving system is required to provide the difference between the actual load demand (P_{demand}) and the limit desired for grid consumption (P_{shave}).

$$P_{Discharge} = P_{demand} - P_{shave} \tag{3.1}$$

Given first, the voltage level of the grid, and secondly, the active power $P_{Discharge}$ and the power factor at which the power is discharged at (i.e. $Q_{Discharge}$), the instantaneous three phase grid voltages (V_{a_grid}, V_{b_grid}, and V_{c_grid}) are translated to the corresponding two-phase components (V_{α_grid}, and V_{β_grid}) using Clarke transformation.

$$T_{abc-to-\alpha\beta} = \sqrt{\frac{2}{3}} \times \begin{bmatrix} 1 & \frac{-1}{2} & \frac{-1}{2} \\ 0 & \frac{\sqrt{3}}{2} & \frac{-\sqrt{3}}{2} \end{bmatrix} \tag{3.2}$$

$$\begin{bmatrix} v_{\alpha\_grid} \\ v_{\beta\_grid} \end{bmatrix} = T_{abc-to-\alpha\beta} \times \begin{bmatrix} v_{a\_grid} \\ v_{b\_grid} \\ v_{c\_grid} \end{bmatrix} \tag{3.3}$$

The two-phase components (V_{α_grid}, and V_{β_grid}) are then used alongside the active and reactive power to be discharged from the peak shaving system ($P_{Discharge}$, $Q_{Discharge}$) to calculate the two-phase current components (i_{α_peak}, i_{β_peak}).

$$i_{\alpha\_peak} = \frac{P_{Discharge} - v_{\beta\_grid} \times i_{\beta\_peak}}{v_{\alpha\_grid}} \tag{3.4}$$

$$i_{\beta\_peak} = \frac{P_{Discharge} \times v_{\beta\_grid} - Q_{Discharge} \times v_{\alpha\_grid}}{v_{\alpha\_grid}^{\,2} + v_{\beta\_grid}^{\,2}} \tag{3.5}$$

Figure 3.1 shows the control block diagram of the peak shaving system. The required three phase current references for peak shaving (i_{a_peak}, i_{b_peak}, and i_{c_peak}) are then obtained using:

$$T_{\alpha\beta-to-abc} = \sqrt{\frac{2}{3}} \times \begin{bmatrix} \frac{1}{\sqrt{2}} & 1 & 0 \\ \frac{1}{\sqrt{2}} & \frac{-1}{2} & \frac{\sqrt{3}}{2} \\ \frac{1}{\sqrt{2}} & \frac{-1}{2} & \frac{-\sqrt{3}}{2} \end{bmatrix} \tag{3.6}$$

$$\begin{bmatrix} i_{a\_peak} \\ i_{b\_peak} \\ i_{c\_peak} \end{bmatrix} = T_{\alpha\beta-to-abc} \times \begin{bmatrix} i_0 \\ i_{\alpha\_peak} \\ i_{\beta\_peak} \end{bmatrix} \tag{3.7}$$

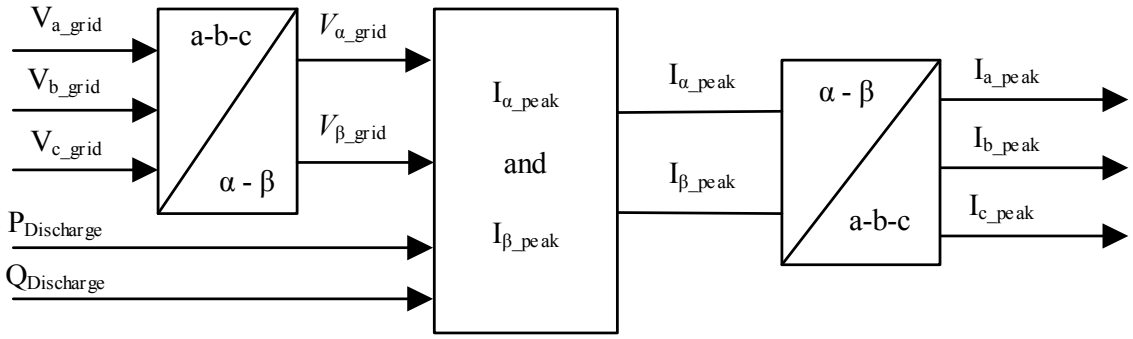

Figure 3.1 Control block diagram of peak shaving system.

3.2.2 Active Power Filtering Control Module

To overcome the drawbacks of passive LC filters, and with the advancements in the power semiconductor industry, the use of active filters instead of passive filters in harmonic mitigation has become more prevalent [8]. Active filtering can be implemented through different configurations based on the connection to the system: i) Series active power filter, ii) Shunt active power filter, and iii) Hybrid active power filters.

The series active filter is used to compensate the voltage harmonics through the series injection of currents. The shunt active filter is connected in parallel with the source and used to

compensate the current harmonics in the system. The hybrid active filter is a combination of a passive and active filter [9].

In this chapter, a shunt active power filter is adopted. The control scheme used in [9] is selected, where the instantaneous three phase load currents and voltages are translated to their corresponding two-phase components (α – β components).

$$\begin{bmatrix} v_{\alpha\_load} \\ v_{\beta\_load} \end{bmatrix} = T_{abc-to-\alpha\beta} \times \begin{bmatrix} v_{a\_load} \\ v_{b\_load} \\ v_{c\_load} \end{bmatrix} \tag{3.8}$$

$$\begin{bmatrix} i_{\alpha\_load} \\ i_{\beta\_load} \end{bmatrix} = T_{abc-to-\alpha\beta} \times \begin{bmatrix} i_{a\_load} \\ i_{b\_load} \\ i_{c\_load} \end{bmatrix} \tag{3.9}$$

The α-β components contain a fundamental component and harmonic content. The instantaneous active power and the instantaneous reactive power ($P_{\_load}$ and $Q_{\_load}$) are then calculated using:

$$P_{load} = v_{\alpha\_load} \times i_{\alpha\_load} + v_{\beta\_load} \times i_{\beta\_load} \tag{3.10}$$

$$Q_{load} = -v_{\alpha\_load} \times i_{\beta\_load} + v_{\beta\_load} \times i_{\alpha\_load} \tag{3.11}$$

The calculated powers result from the fundamental component (P_{fun}, Q_{fun}) and the harmonic content (P_{har}, Q_{har}). To extract the active and reactive power resulting from the harmonic content (P_{har}, and Q_{har}), a low pass filter is used to extract the fundamental components of the active and reactive powers. The fundamental components are then subtracted from the calculated powers.

The required current to filter the harmonic content in the line current (i_{α_har}, i_{β_har}) are calculated using equations 3.12, and 3.13. The required compensation current references (i_{a_har}, i_{b_har}, and i_{c_har}) are calculated using equation 3.14. The control block diagram is shown in figure 3.2.

$$i_{\alpha\_har} = \frac{P_{har} - v_{\beta\_load} \times i_{\beta\_har}}{v_{\alpha\_load}} \tag{3.12}$$

$$i_{\beta\_har} = \frac{P_{har} \times v_{\beta\_load} - Q_{load} \times v_{\alpha\_load}}{{v_{\alpha\_load}}^2 + {v_{\beta\_load}}^2} \tag{3.13}$$

$$\begin{bmatrix} i_{a\_har} \\ i_{b\_har} \\ i_{c\_har} \end{bmatrix} = T_{\alpha\beta-to-abc} \times \begin{bmatrix} i_{\alpha\_har} \\ i_{\beta\_har} \\ 0 \end{bmatrix} \tag{3.14}$$

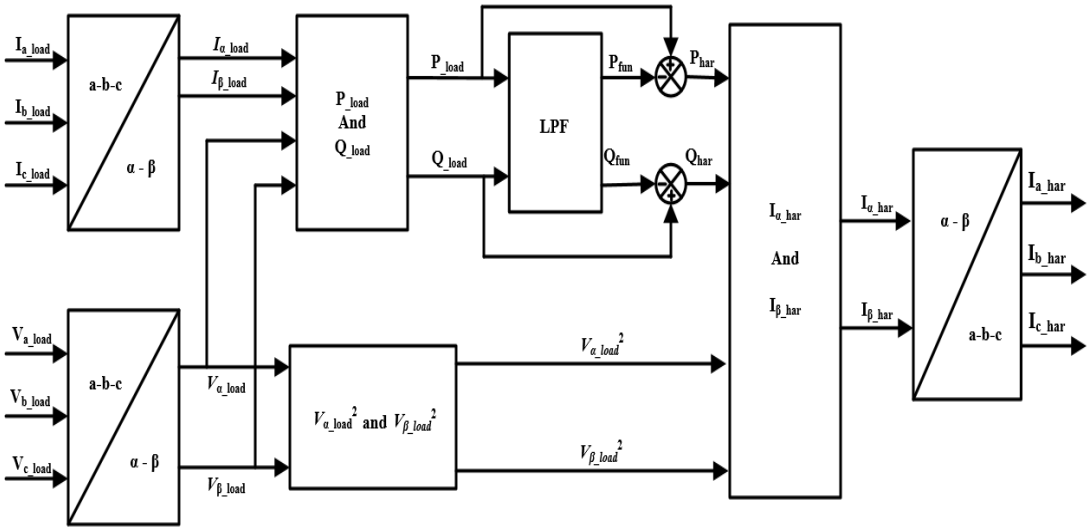

Figure 3.2 Control block diagram of shunt active power filter.

3.2.3 Reactive Power Compensation Control Module

Controlling the flow of the reactive power ensures the proper operation of the power system [5, 27] and reduces the power transmission losses [5, 6, 27]. The shunt active power filter creates the current references from the harmonic content of the line currents by introducing the low pass filter to the control block. To compensate for the reactive power, the calculated reactive power ($Q_{\_load}$) including the fundamental and the harmonic content (Q_{fun}, and Q_{har}) is used to generate the current references. The block diagram of the control logic is shown in figure 3.3.

The three sets of references are then added to form the required three phase current references to be injected from the batteries to the load. A hysteresis current controller is fed the three current references to produce the gating signals to the inverter switches.

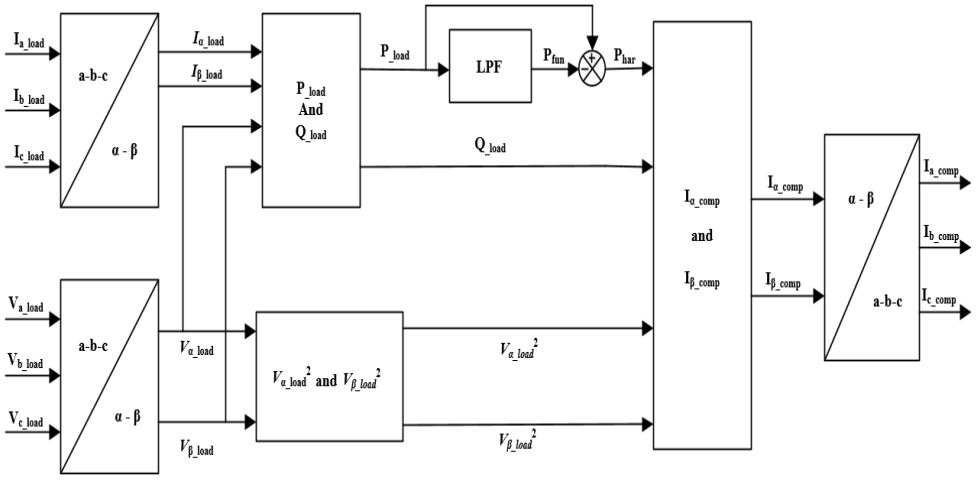

Figure 3.3 Control block diagram of shunt active power filter and reactive power compensation system.

3.2.4 Hysteresis Current Control (HCC)

Hysteresis current control is a very powerful control technique. It is employed in a variety of applications such as active power filters [30], and single phase grid connected inverters [31], due to its dynamic response, stability, accuracy, and independence of load parameters and nature [30-33]. Space vector HCC (SV-HCC) [32], zero crossing detection based HCC (ZCD-HCC) [33], are two improved versions of HCC. However, the added level of complexity in these improved versions is a major drawback.

In this chapter, the conventional HCC is adopted. The concept of HCC is to create an envelope around the required reference called the Hysteresis Band (HB). One side of the HB would be higher than the required reference by $\frac{\mathrm{HB}}{2}$, while the other HB side is less by $\frac{\mathrm{HB}}{2}$.

The current is allowed an error margin within the HB. Figure 3.4 shows the concept of the HCC, the switch to be controlled is switched on when the actual current reaches the lower hysteresis band for T_{ON} time units and switched off when the current reaches the upper hysteresis band for T_{OFF} time units, resulting in a PWM signal.

The switching frequency (f_{sw}) is equal to the inverse of T_{ON} plus T_{OFF}. As seen from figure 3.4, the switching frequency is directly related to the hysteresis band width. A narrow HB corresponds to higher switching frequencies. The switching losses also increase with the switching frequency. The selection of the HB width is therefore a tradeoff between the required accuracy and the subsequent switching losses.

$$f_{sw} = \frac{1}{T_{ON} + T_{OFF}} \qquad (3.15)$$

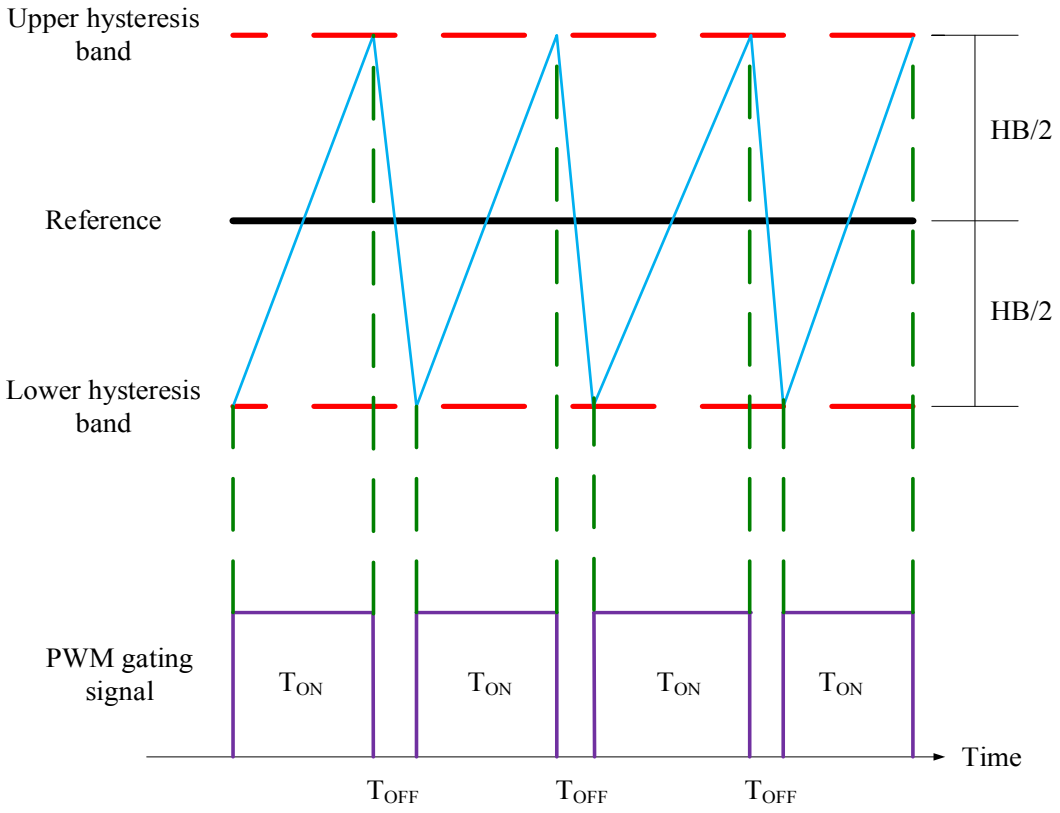

Figure 3.4 Hysteresis current control.

3.3 Simulation and Experimental Results

To validate the performance of the proposed control, two common power quality issues are simulated with two case studies; one case examines the effects of the proposed control on a load with a high THD, and the other case studies the effect on a load with a poor power factor. Figure 3.5 shows the system studied.

With the manual switch turned off, the load consists of two diode bridge rectifiers (non-linear load 1 and non-linear load 2), in this case the load current is highly non-linear, and the power is consumed at a high power factor. When the manual switch in figure 3.5 is turned on, the linear highly inductive load is connected and the load current becomes more sinusoidal but the power factor of the system drops. Table 3.1 shows the values of elements in figure 3.5.

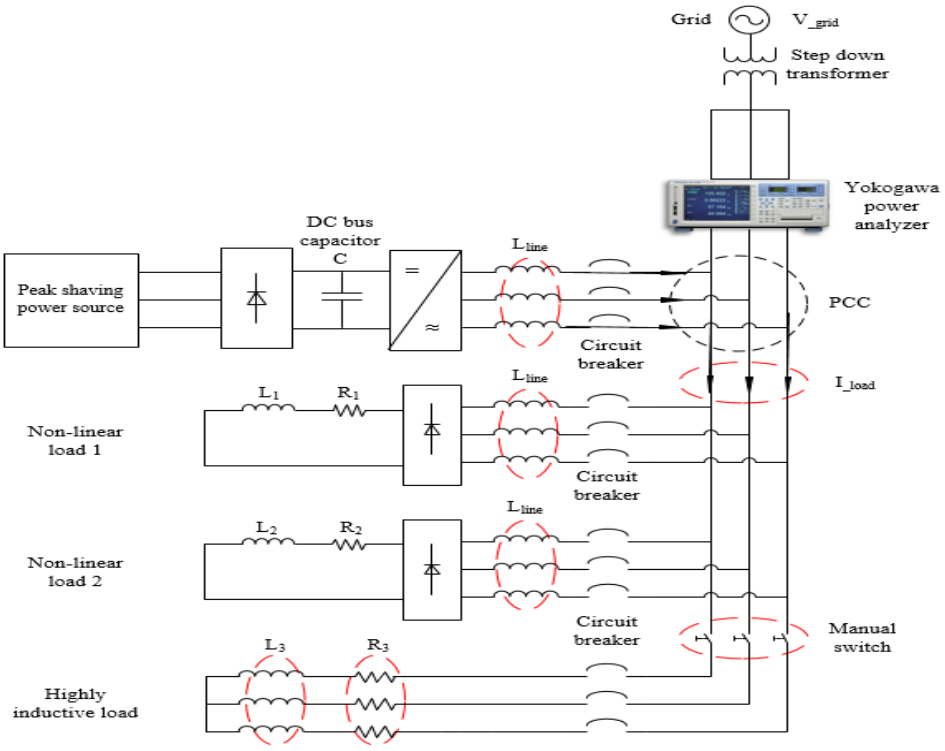

Figure 3.5 System layout of case studies.

Table 3.1 System layout of case study.

Component	Value	Component	Value
R_1	90 Ω	L_2	5 mH
R_2	60 Ω	L_3	16 mH
R_3	2 Ω	L_{line}	5 mH
L_1	5 mH	C	7.8 mF
L_2	5 mH	L_2	5 mH

The proposed control technique is run on the two case studies and this section discusses the obtained results. The simulation results of each control module of the proposed control will be discussed. The experimental results will be presented after.

3.3.1 Simulation Results

3.3.1.1 Case Study One: Operation with High THD:

The first case study examines the operation in a network with a high THD. The load in this case consists of two diode bridge rectifiers supplying an inductive load. Each control module will be activated individually first, then all the control modules will be activated to achieve peak shaving, active power filtering, and reactive power compensation, simultaneously.

3.3.1.1.1 Active Power Filtering:

The active power filtering module of the proposed control technique is implemented in SIMULINK/MATLAB. The control scheme is activated at a simulation time of 0.2 seconds for only filtering. Figure 3.6 (a) is the load current, (b) is the injected current from the filter, and (c) is the grid current. As seen from (c) before activating the filter, the current drawn from the grid has a THD of 25.02% at a PF of 0.956. While after activating the filter the grid current becomes sinusoidal with a THD of 6.39% at a PF of 0.999. Table 3.2 summarizes the filtering function. Figure 3.7 shows a comparison between the harmonic spectrum of the line current before and after the application of the filter.

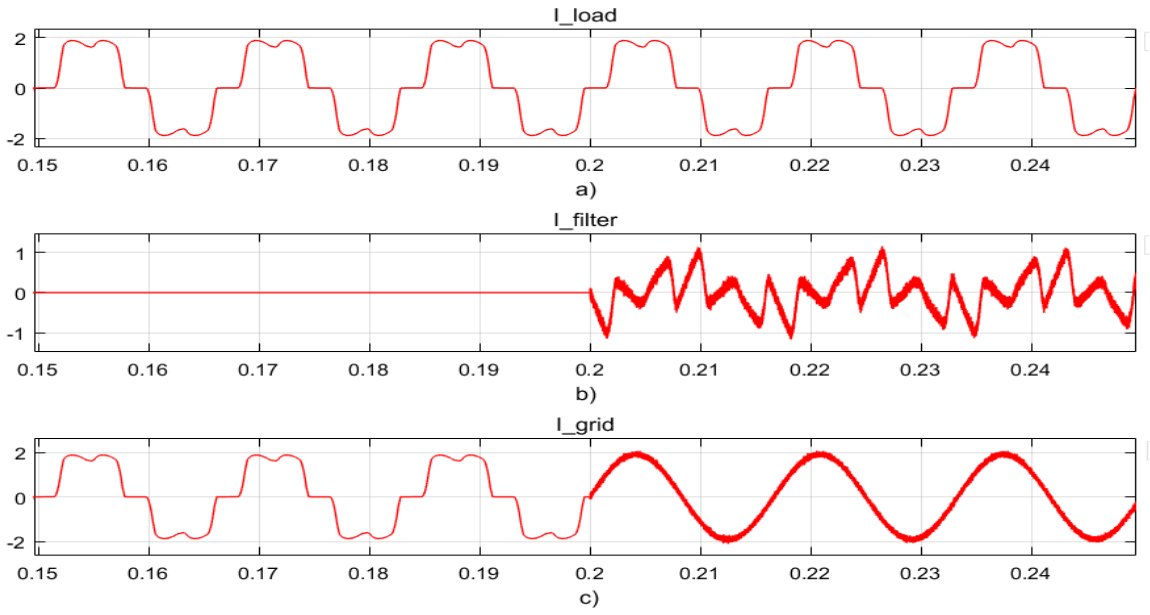

Figure 3.6 Harmonic distortion case study: Simulation results for active power filtering, (a) load current, (b) injected filter current, and (c) grid current.

Table 3.2 Harmonic distortion case study summary of simulation results for active power filtering.

	Before filtering	After filtering
	Phase A	Phase A
Phase voltage (V)	28.8675	28.8675
Line current (A)	1.4143	1.3543
Three phase active power (W)	117.1	117.2
PF	0.956	0.999
THD (%)	25.02	6.39

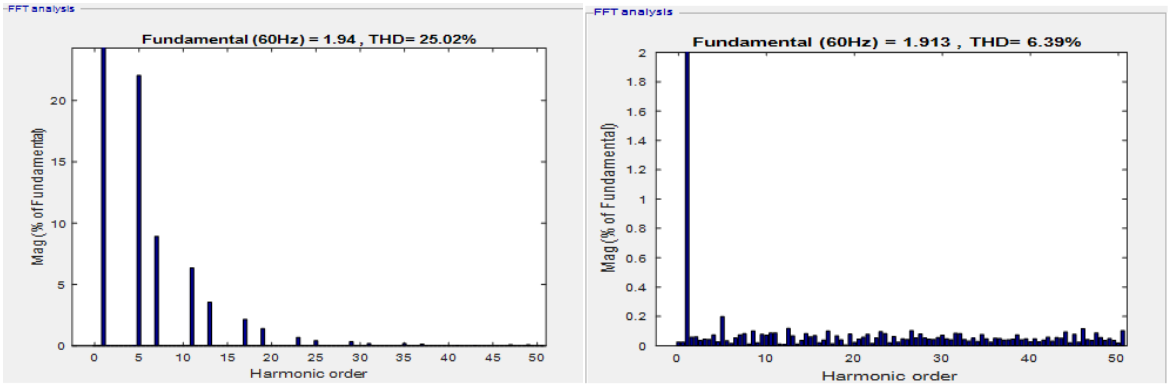

(a) (b)

Figure 3.7 Harmonic distortion case study: Harmonic spectrum of line current (a) before active power filtering, (b) after active power filtering.

3.3.1.1.2 Peak Shaving:

The proposed control strategy is set to reduce the peak demand drawn from the grid by 25%. Figure 3.8 shows the simulation results. Table 3.3 summarizes the results and figure 3.9 shows the harmonic spectrum of the line current before and after the peak shaving. As seen from table 3.3, the THD of the line current increases from 25.02% to 34.34%, that's because both the harmonics generated from the non-linear loads and the hysteresis controller are now reflected on the grid. The power factor drops to 0.93 from 0.95, and peak shaving function reduced the total power drawn from the grid to 88.34 W. As a result, the drawn current is reduced from 1.414 A to 1.0887 A.

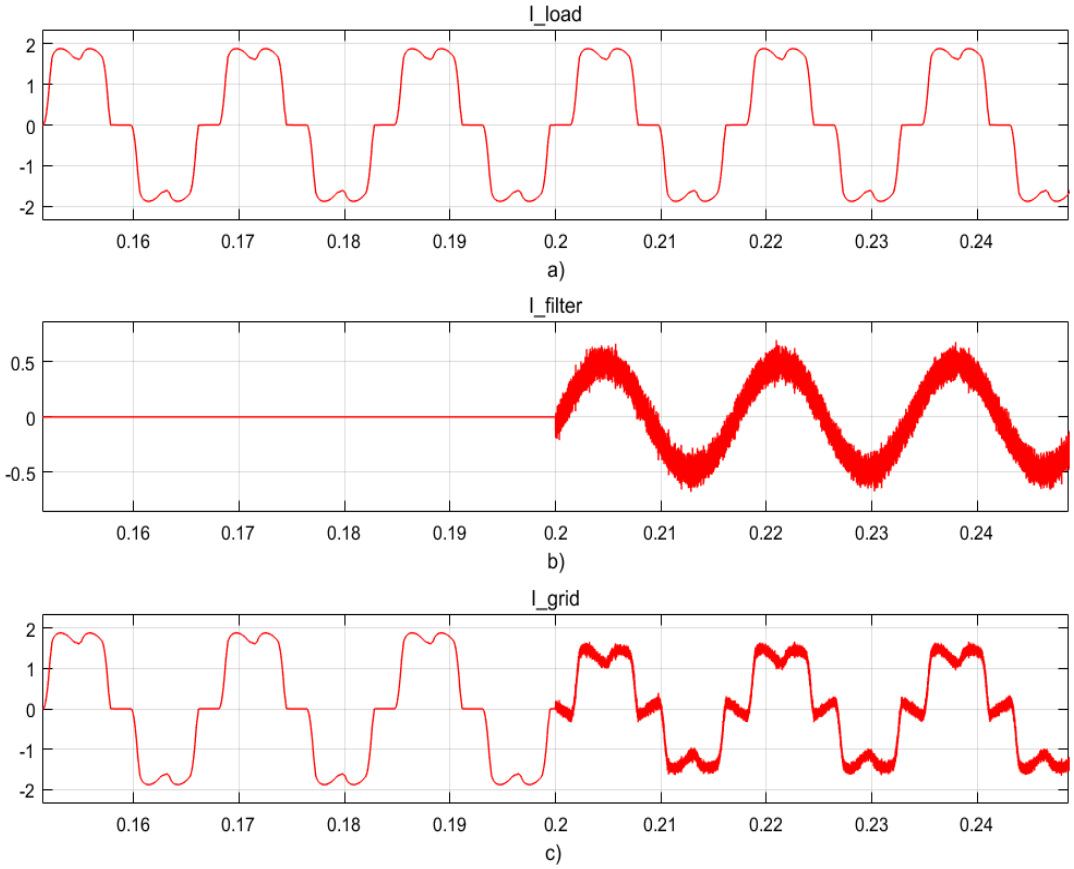

Figure 3.8 Harmonic distortion case study: Simulation results for peak shaving, (a) load current, (b) injected filter current, and (c) grid current.

Table 3.3 Harmonic distortion case study summary of simulation results for peak shaving.

	Before peak shaving	After peak shaving
	Phase A	Phase A
Phase voltage (V)	28.8675	28.866
Line current (A)	1.4143	1.0887
Three phase active power (W)	117.1	88.34
PF	0.956	0.9302
THD (%)	25.02	34.34

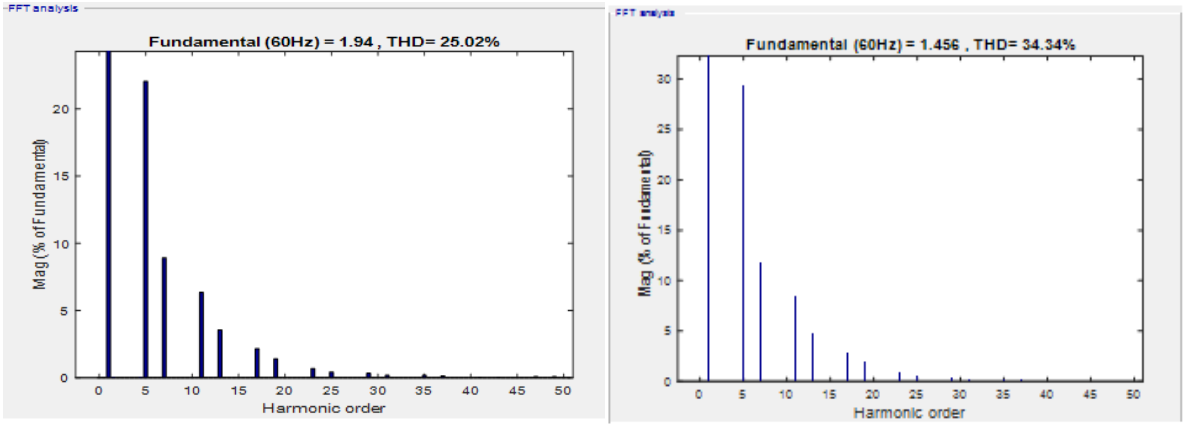

(a) (b)

Figure 3.9 Harmonic distortion case study: Harmonic spectrum of line current (a) before peak shaving, (b) after peak shaving.

3.3.1.1.3 Peak Shaving, Active Power Filtering, and Reactive Power Compensation:

The proposed control strategy is set to achieve peak shaving, active power filtering, and reactive power compensation. The peak shaving subsection of the proposed control is set to reduce the total active power drawn from the grid by 25%. The simulation results are shown in figure 3.10. Table 3.4 summarizes the simulation results and the line current harmonic spectrum before and after the peak shaving and filtering is shown in figure 3.11. The proposed control technique reduces the power drawn from the grid from 117.1 W to 87.35 W. The THD is reduced from 25.02% to 8.62% and the PF is improved from 0.96 to 0.99.

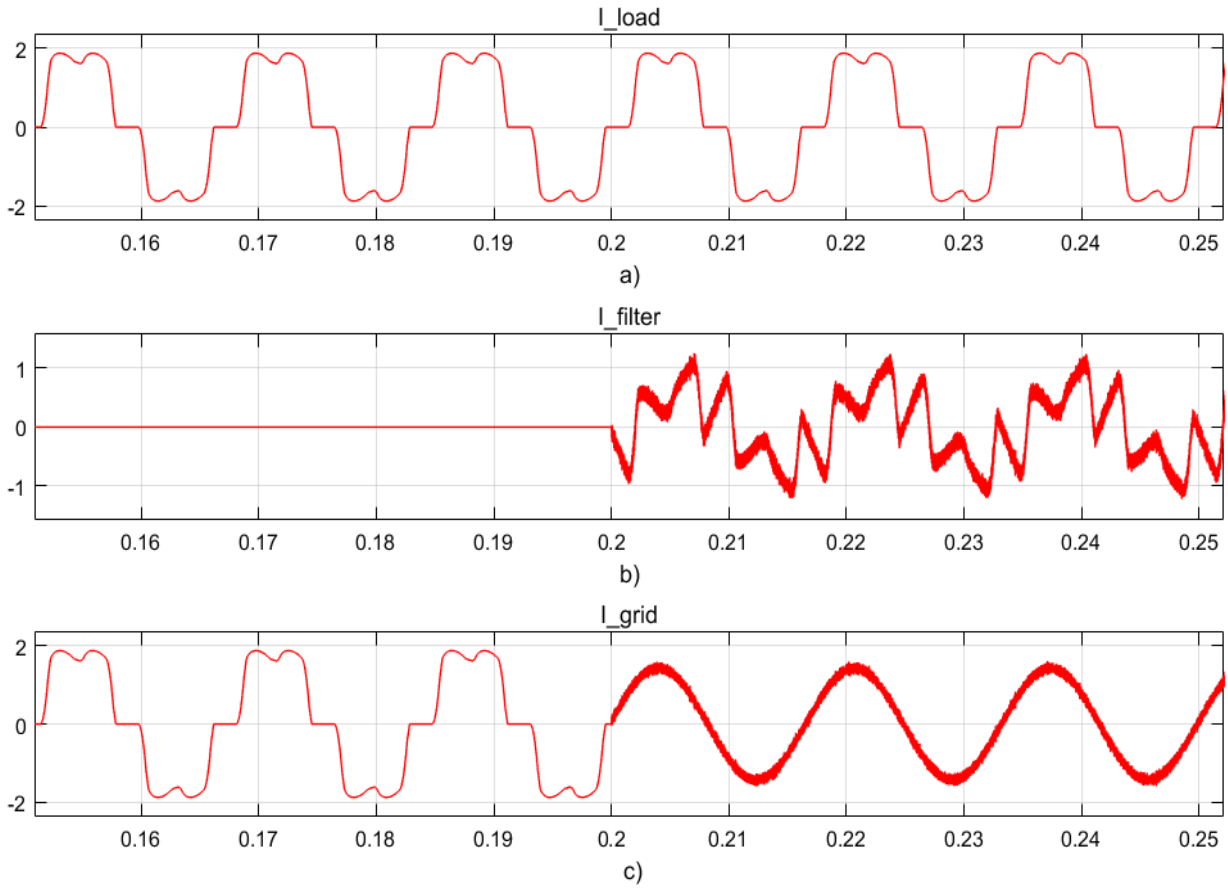

Figure 3.10 Harmonic distortion case study: Simulation results for peak shaving and active filtering: (a) load current, (b) injected filter current, and (c) grid current.

Table 3.4 Harmonic distortion case study summary of simulation results for peak shaving and active power filtering.

	Before peak shaving and filtering	After peak shaving and filtering
	Phase A	Phase A
Phase voltage (V)	28.8675	28.866
Line current (A)	1.4143	1.012
Three phase active power (W)	117.1	87.35
PF	0.956	0.9965
THD (%)	25.02	8.62

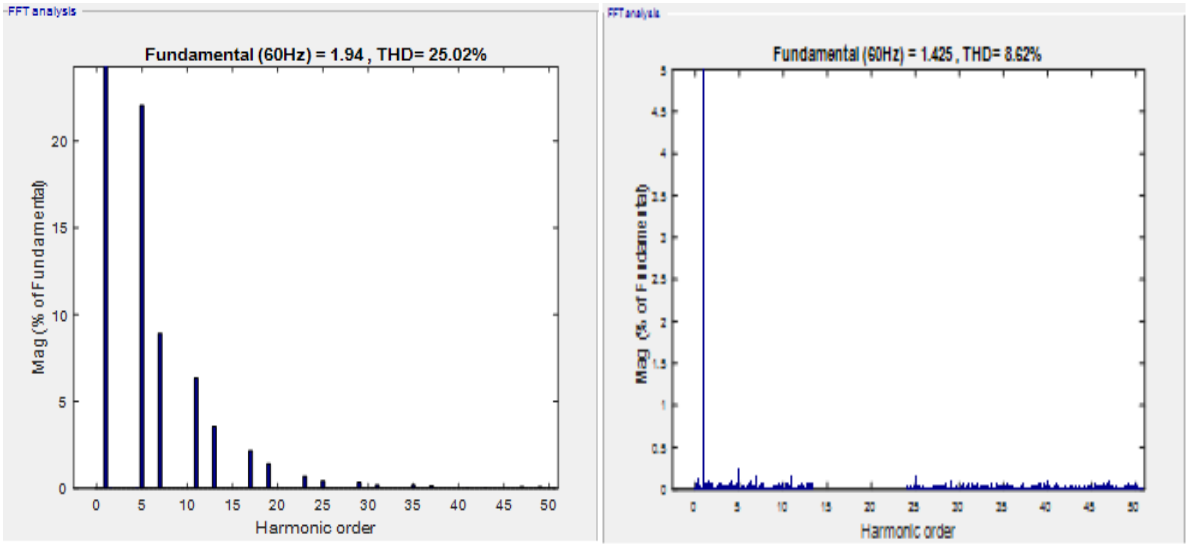

(a) (b)

Figure 3.11 Harmonic distortion case study: Harmonic spectrum of line current (a) before peak shaving and active filtering, (b) after peak shaving and active filtering.

3.3.1.2 Case Study Two: Performance at a Low PF:

The second case study examines the operation in a network with a low PF. Each control module will be activated individually first. Then, all the control modules will be activated to achieve peak shaving, active power filtering, and reactive power compensation, simultaneously.

3.3.1.2.1 Active Power Filtering:

The proposed control is simulated for the case with a low power factor just for active filtering. The PF improved from 0.51 to 0.999 with a slight reduction in the THD. Figure 3.12 shows the simulation results. Table 3.5 summarizes the filtering function. Figure 3.13 compares the harmonic spectrum of the line current before and after the application of the filter.

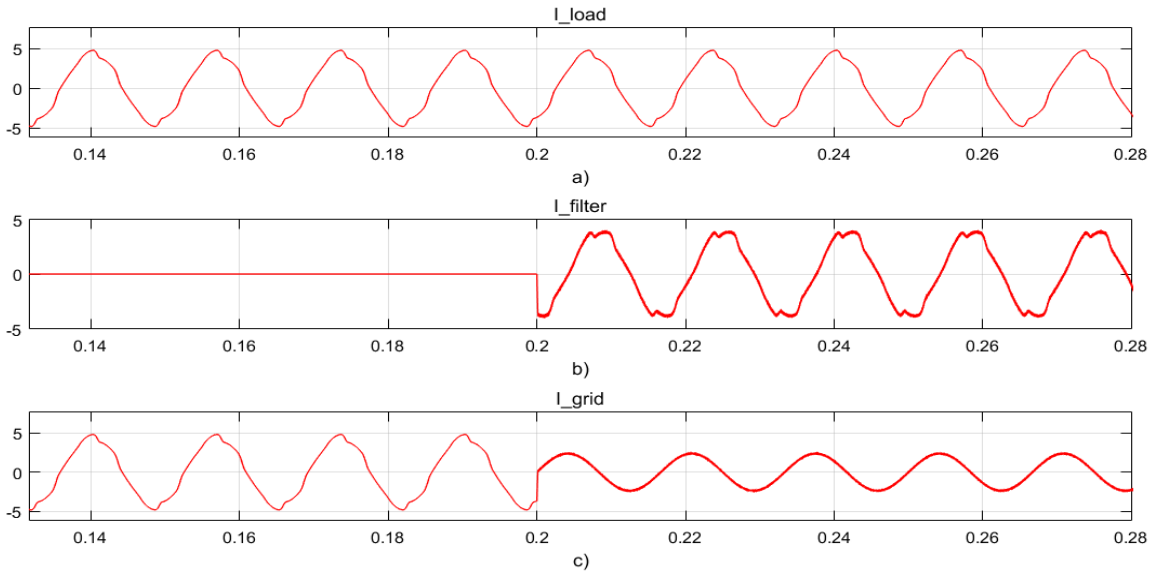

Figure 3.12 Low power factor case study: Simulation results for active power filtering, (a) load current, (b) injected filter current, and (c) grid current.

Table 3.5 Low power factor case study summary of simulation results for active power filtering.

	Before filtering	After filtering
	Phase A	Phase A
Phase voltage (V)	17.3188	17.3188
Line current (A)	3.222	1.675
Three phase active power (W)	86.63	86.99
PF	0.5174	0.999
THD (%)	6.41	5.15

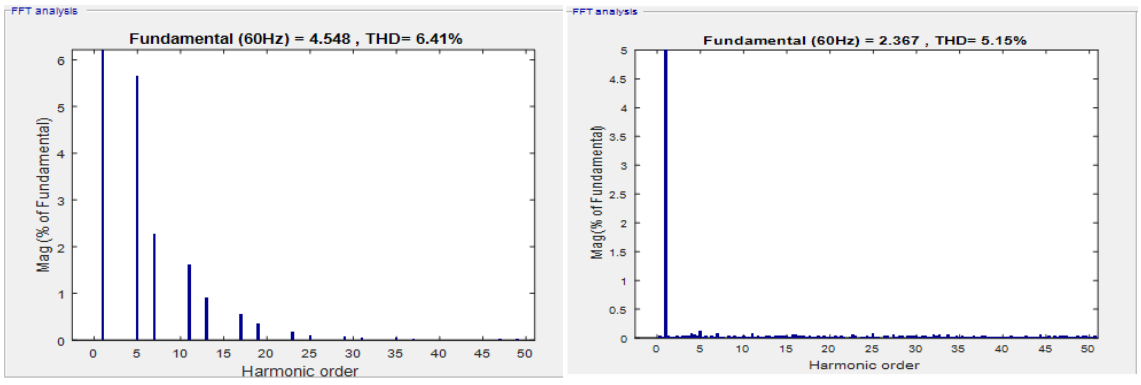

(a) (b)

Figure 3.13 Low power factor case study: Harmonic spectrum of line current (a) before active power filtering, (b) after active power filtering.

3.3.1.2.2 Peak Shaving:

The same procedure is followed with the low PF case study. The control is set to reduce the peak power from grid by 25%. Figure 3.14 shows the simulation results. Table 3.6 summarizes the simulation results. Figure 3.15 shows the harmonic spectrum of the line current before and after peak shaving. As seen from the results, the PF drops to 0.4254 and the THD increases to 7.63%. The total power drawn from the grid was reduced to 65.02 W instead of 86.63 W.

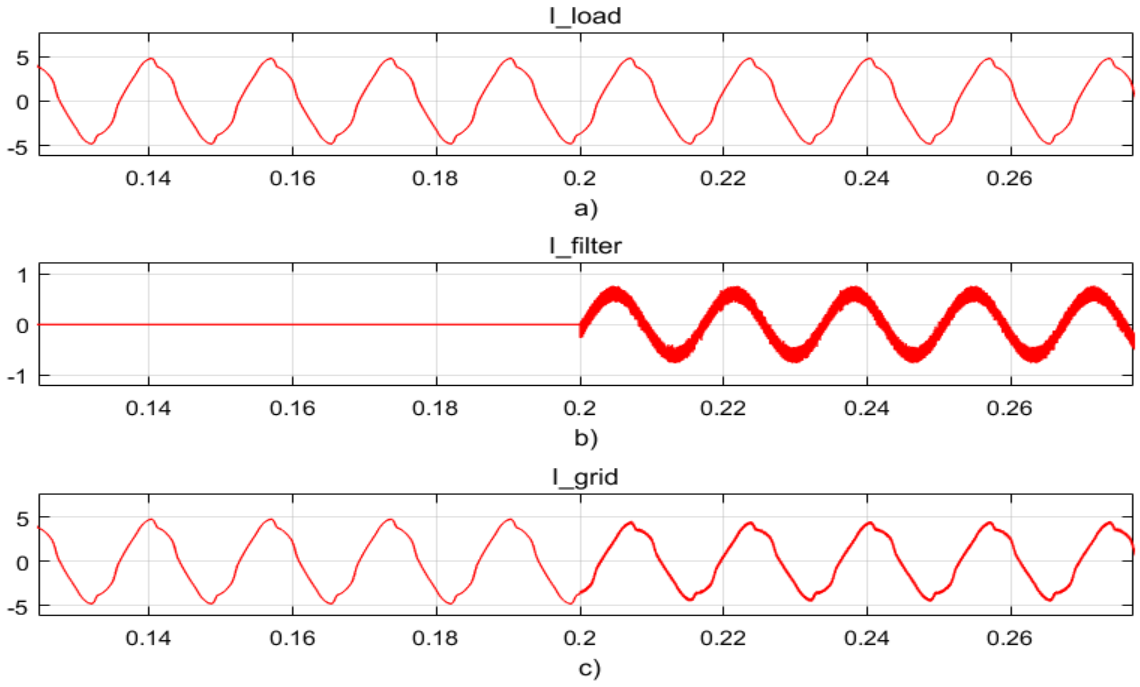

Figure 3.14 Low power factor case study: Simulation results for peak shaving, (a) load current, (b) injected filter current, and (c) grid current.

Table 3.6 Low power factor case study summary of simulation results for peak shaving.

	Before peak shaving	After peak shaving
	Phase A	Phase A
Phase voltage (V)	17.3188	17.319
Line current (A)	3.222	2.9425
Three phase active power (W)	86.63	65.02
PF	0.5174	0.4254
THD (%)	6.41	7.63

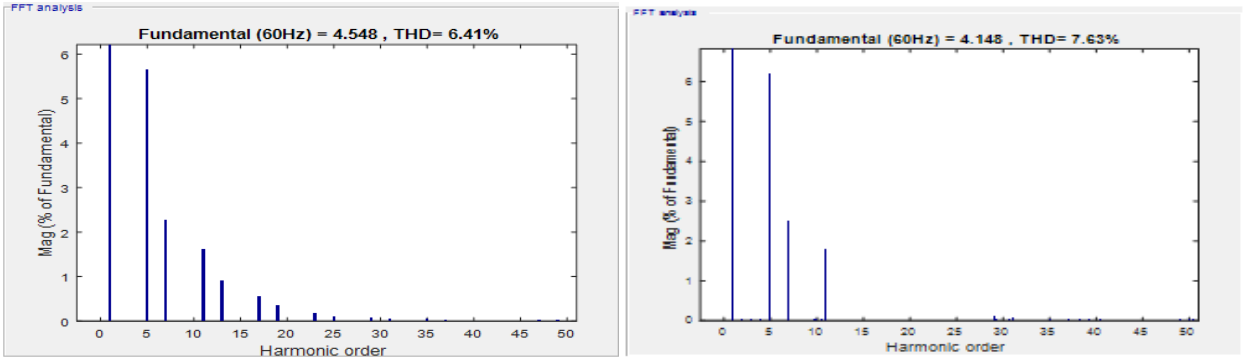

(a) (b)

Figure 3.15 Low power factor case study: Harmonic spectrum of line current (a) before peak shaving, (b) after peak shaving.

3.3.1.2.3 Peak Shaving, Active Power Filtering, and Reactive Power Compensation:

The same procedure used for the performance under harmonic distortion was followed for operation at low PF. Figure 3.16 shows the simulation results. Table 3.7 summarizes the simulation results. The PF is improved from 0.5174 to 0.9958, and the THD is increased slightly from 6.41% to 6.90%. The total power drawn from the grid is reduced to 65.01 W instead of 86.63 W. Figure 3.17 shows the harmonic spectrum of the line current before and after the peak shaving and active power filtering.

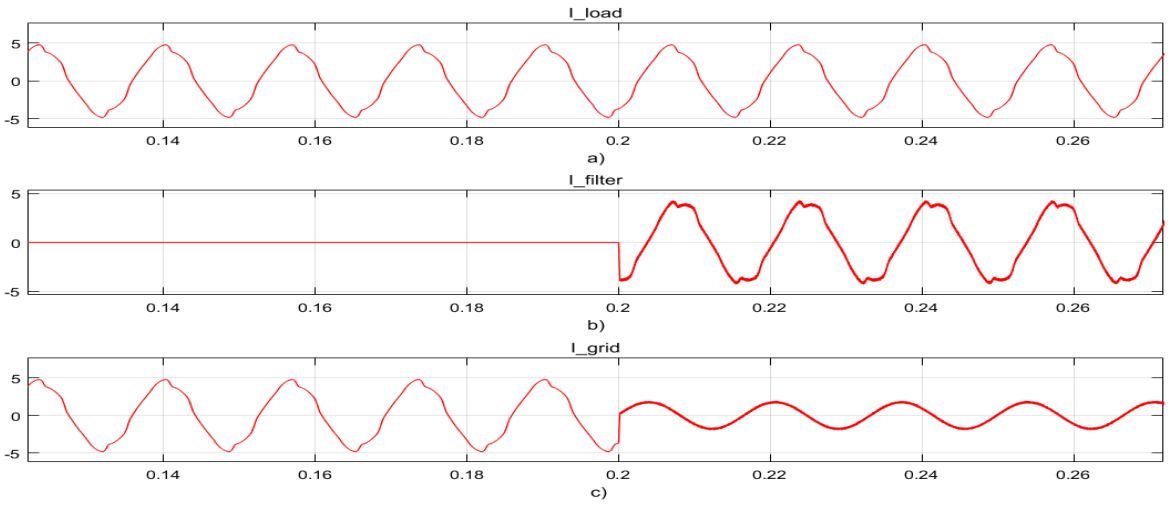

Figure 3.16 Low power factor case study: Simulation results for peak shaving and active filtering, (a) load current, (b) injected filter current, and (c) grid current.

Table 3.7 Low power factor case study summary of simulation results for peak shaving and active filtering.

	Before peak shaving and filtering	After peak shaving and filtering
	Phase A	Phase A
Phase voltage (V)	17.3188	17.319
Line current (A)	3.222	1.2558
Three phase active power (W)	86.63	65.01
PF	0.5174	0.9958
THD (%)	6.41	6.90

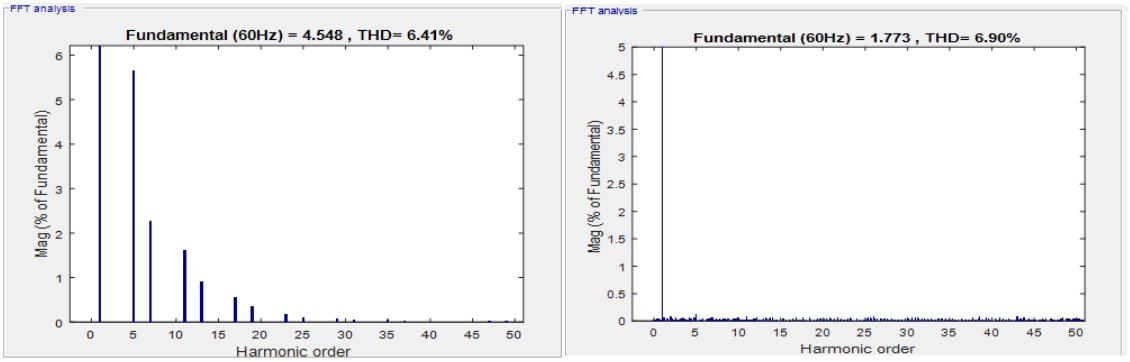

(a) (b)

Figure 3.17 Low power factor case study: Harmonic spectrum of line current (a) before peak shaving and active filtering, (b) after peak shaving and active filtering.

3.3.2 Experimental Results

The system in figure 3.5 is also built in the laboratory to validate the proposed control. However, the built experimental setup is scaled down to a lower voltage level due to the current rating of some of the components found in the laboratory. The experimental setup is scaled down to 50 V line to line for the harmonic distortion case and 30 V line to line for the low power factor case study. The experimental setup is shown in figure 3.18.

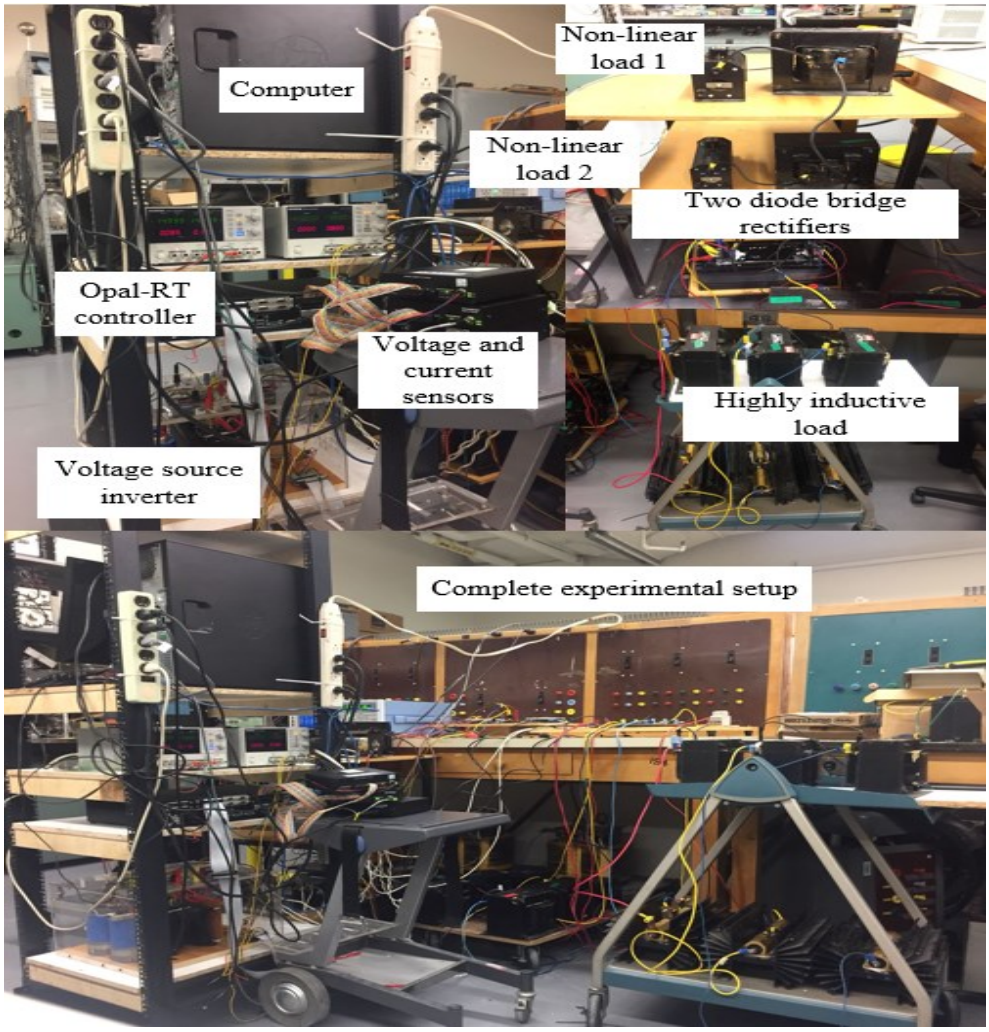

Figure 3.18 Experimental setup.

3.3.2.1 Grid Synchronization:

Grid synchronization of power electronic converters connected at the point of common coupling (PCC) is a key factor in the design procedure of control techniques for power electronic converters [34]. The performance of a control technique is highly dependent on the accuracy and quick response of the synchronization technique used [35].

The main objective of synchronization is to estimate the phase angle of the voltages at the PCC. The estimated phase angle will be used to synchronize the injected currents with those of the grid. Inaccurate synchronization will force the voltages at the PCC to become unstable and in some extreme cases might even cause black-outs [36, 37].

Synchronous Reference Frame Phase-Locked Loop (SRF-PLL) synchronization technique is deemed to be the most commonly used technique for grid synchronization due to its adequate performance and easy implementation [34], this technique is adopted for our analysis and the estimated phase angle is showed in figure 3.19 plotted against the phase voltage.

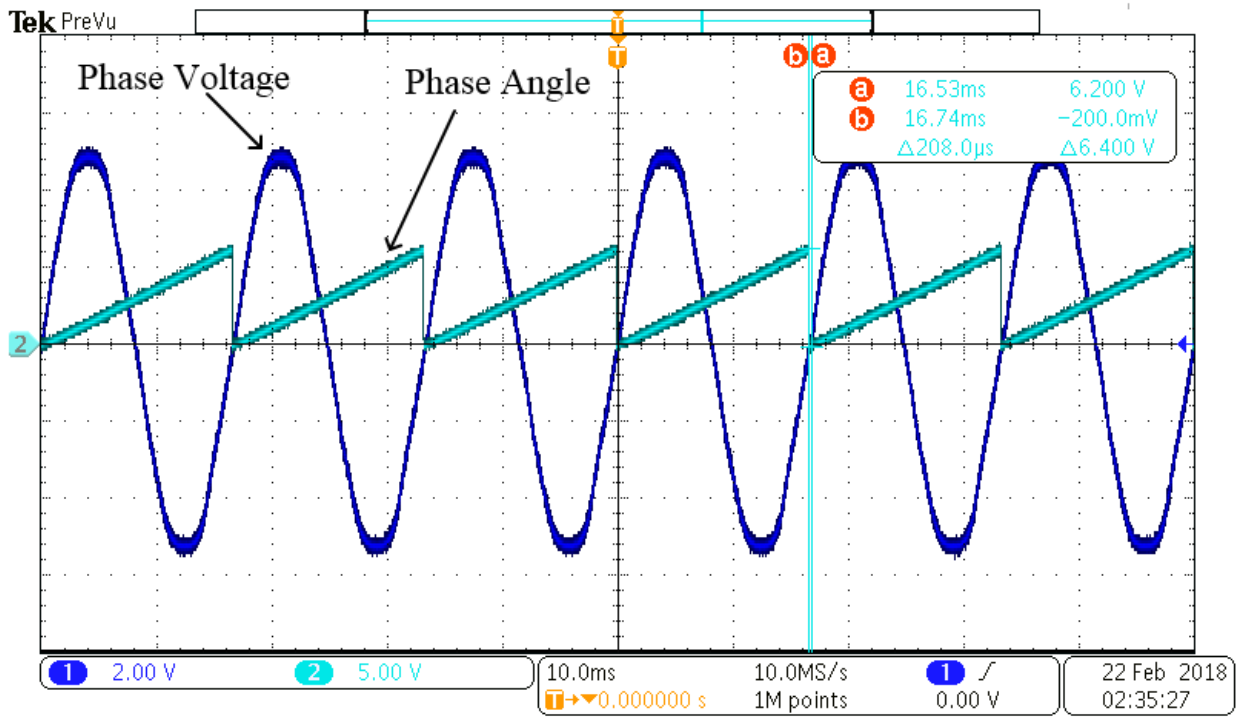

Figure 3.19 Grid synchronization: Phase angle estimation.

3.3.2.2 Case Study One: Operation with High THD:

3.3.2.2.1 Active Power Filtering:

The proposed control is implemented on the experimental setup. Figure 3.20 shows the experimental results for the system. The THD of the current drawn from the grid is reduced from 20.815% to 7.699% and the PF is improved from 0.952 to 0.98. Table 3.8 summarizes the experimental results for the filtering control module. Figure 3.21 shows a comparison between the harmonic spectrum of the line current of phase A before and after the application of the filter.

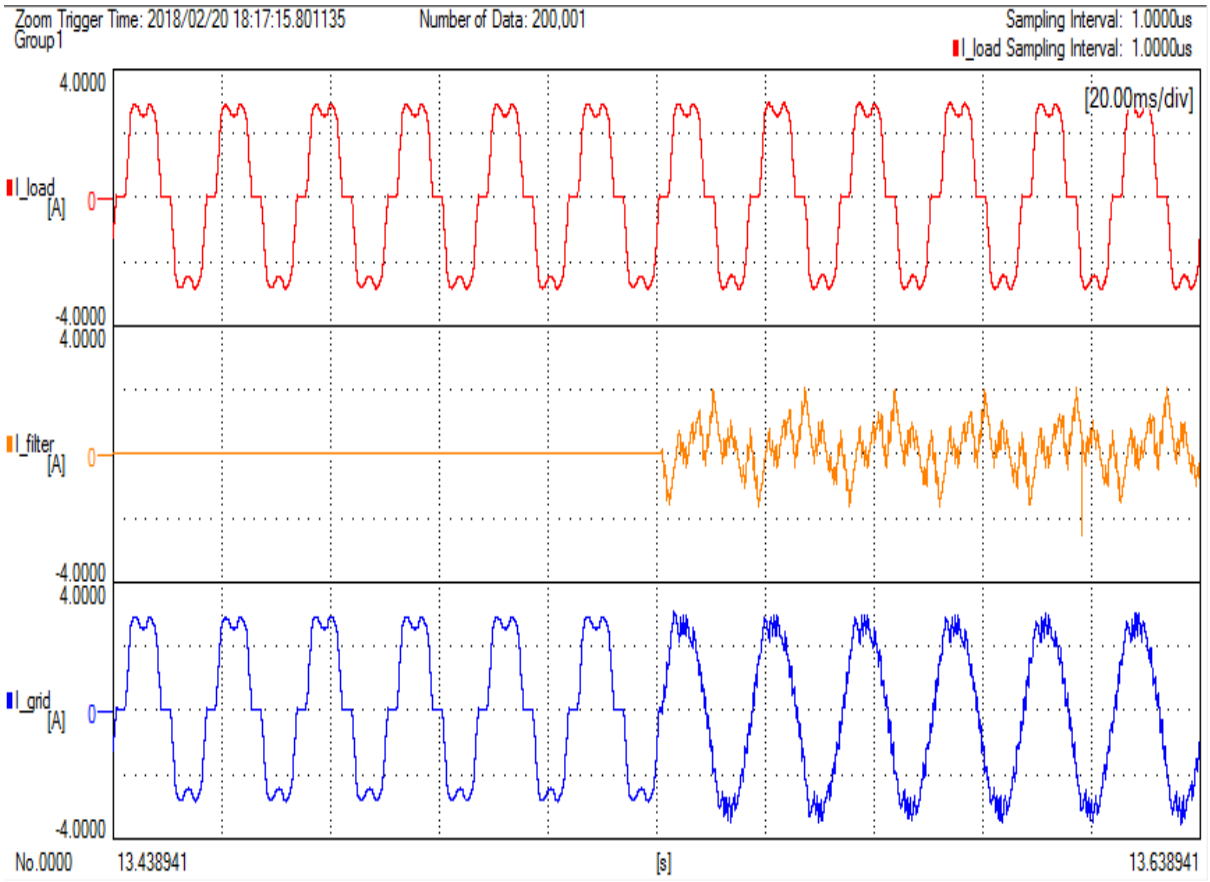

Figure 3.20 Harmonic distortion case study: Experimental results for active power filtering: load current, injected filter current, and grid current, respectively.

Table 3.8 Harmonic distortion case study summary of experimental results for active power filtering.

	Before filtering	After filtering
	Phase A	Phase A
Phase voltage (V)	30.295	30.212
Line current (A)	2.1571	2.1241
Three phase active power (W)	175.9	170.4
PF	0.95146	0.98269
THD (%)	20.815	7.699

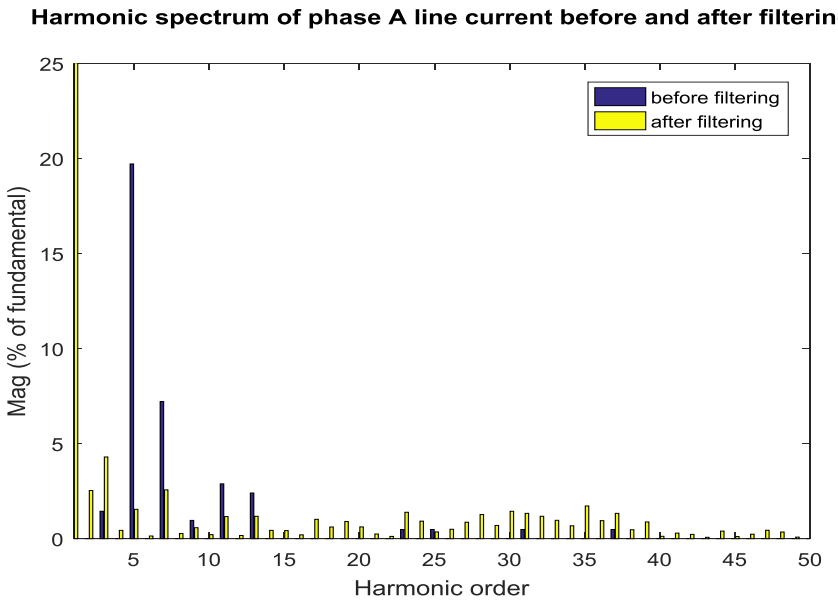

Figure 3.21 Harmonic distortion case study: Harmonic spectrum of line current before and after the filtering.

3.3.2.2.2 Peak Shaving:

The experimental setup is run with the proposed control technique set to achieve peak shaving. The control is set to reduce the peak demand drawn from the grid by 25%. Figure 3.22 shows the experimental results. Table 3.9 summarizes the results and figure 3.23 shows the harmonic spectrum of the line current after the peak shaving. The drawn current is reduced from 2.16 A to 1.74 A. As a result the three phase active power drawn from the grid is reduced to 135.2 W. The THD before the peak shaving is 20.815% and after the peak shaving it increased to 26.898%.

The proposed control technique is also tested for different shave levels using the experimental setup. The different shave levels are set to 10%, 15%, 20% and 25%. The proposed control technique was able to reduce the total three phase active power drawn from the grid to 160.8 W, 152.4 W, 143.9 W, and 135.2 W, respectively. Table 3.10 summarizes the performance of the proposed control for the different shave levels. It can be noticed from table 3.10 that the THD increases as the shave percentage increases. With the increasing shave percentage, the switching in the line current increases as a result of the HCC increase as well. Figure 3.24 shows a comparison between the harmonic spectrums of the line current for the different shave levels.

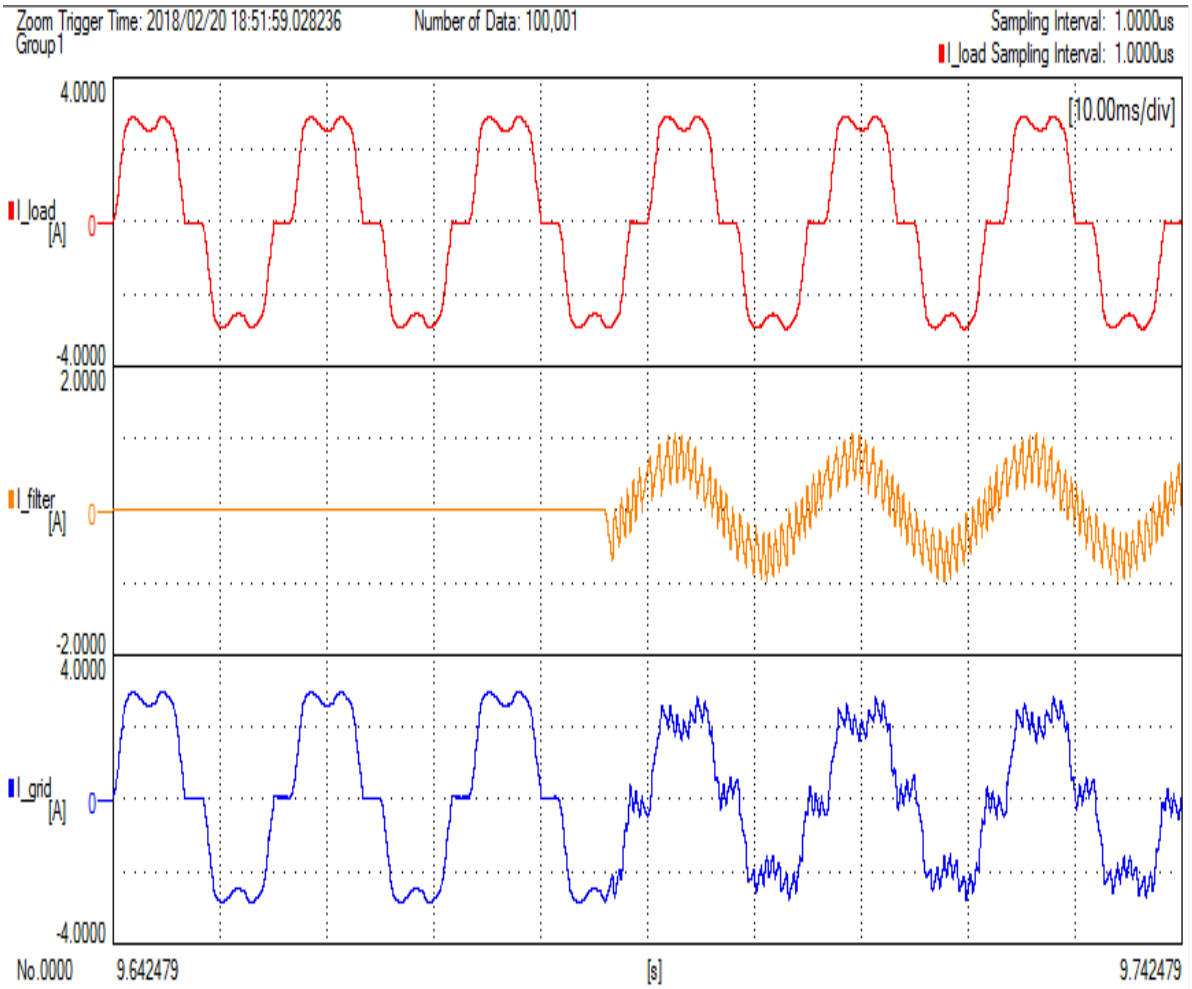

Figure 3.22 Harmonic distortion case study: Experimental results for peak shaving, load current, injected filter current, and grid current, respectively.

Table 3.9 Harmonic distortion case study summary of experimental results for peak shaving.

	Before peak shaving	After peak shaving
	Phase A	Phase A
Phase voltage (V)	30.295	30.59
Line current (A)	2.1571	1.7425
Three phase active power (W)	175.9	135.2
PF	0.95146	0.90496
THD (%)	20.815	26.898

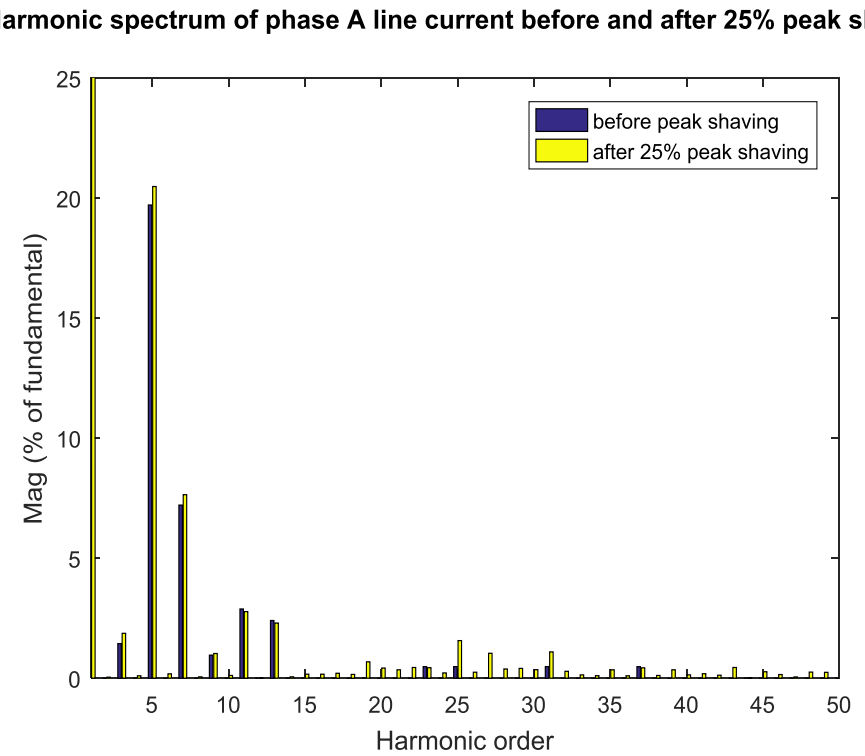

Figure 3.23 Harmonic distortion case study: Harmonic spectrum of phase A line current before and after peak shaving.

Table 3.10 Experimental performance summary for harmonic distortion case study with the different shave levels.

Shave level (%)	Three phase active power from grid (W)	PF	THD (%)
10	160.8	0.921	24.159
15	152.4	0.914	25.285
20	143.9	0.905	26.672
25	135.2	0.895	28.226

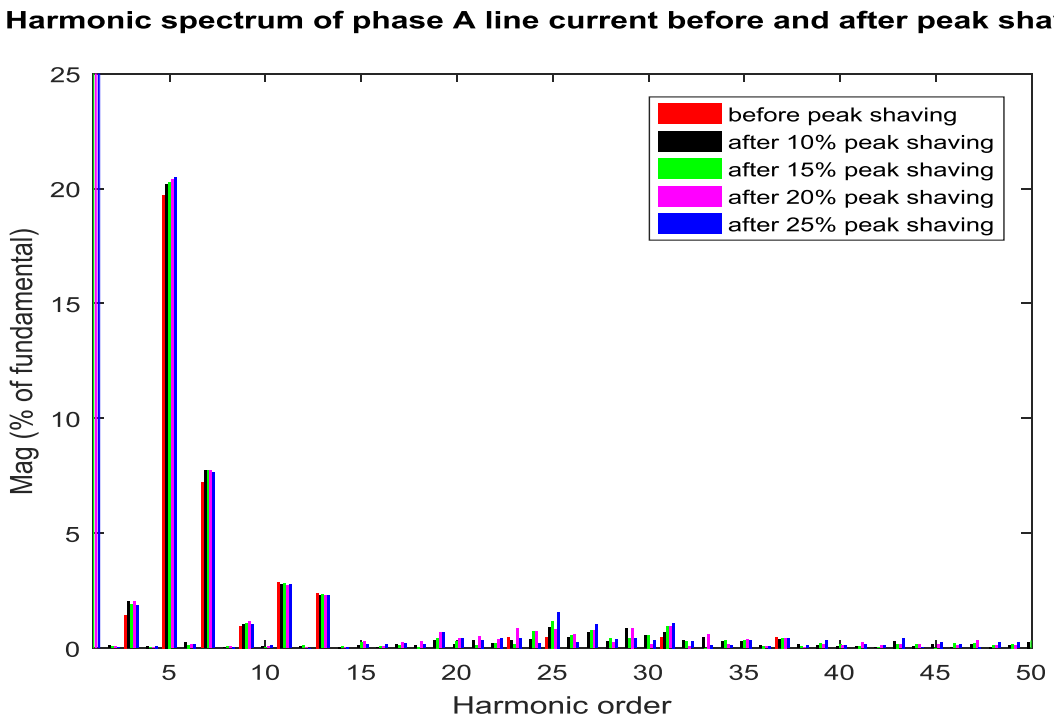

Figure 3.24 Harmonic distortion case study: Harmonic spectrum of phase A line current before and after different shave levels.

3.3.2.2.3 Peak Shaving, Active Power Filtering, and Reactive Power Compensation:

The experimental setup is run with the proposed control set to reduce the total power drawn from the grid by 25%, while compensating the flow of reactive power and active filtering the line current. The experimental results are shown in figure 3.25. Table 3.11 summarizes the experimental results. The total power drawn from the grid is reduced from 175.9 W to 147.1 W, with an improvement in the PF from 0.95146 to 0.976. The THD is decreased from 20.815% to 14.079%. The reduction in not quite clear because the current value is small, hence, the harmonic content in the line current would be high. The line current harmonic spectrum after the peak shaving and active power filtering is shown in figure 3.26.

Different shave levels are also implemented, where the proposed control is set to shave the load peak by 10%, 15%, 20%, and 25%, respectively. Table 3.12 shows the summary of the results for different shave levels. The harmonic spectrum of the line current before and after the control is shown in figure 3.27.

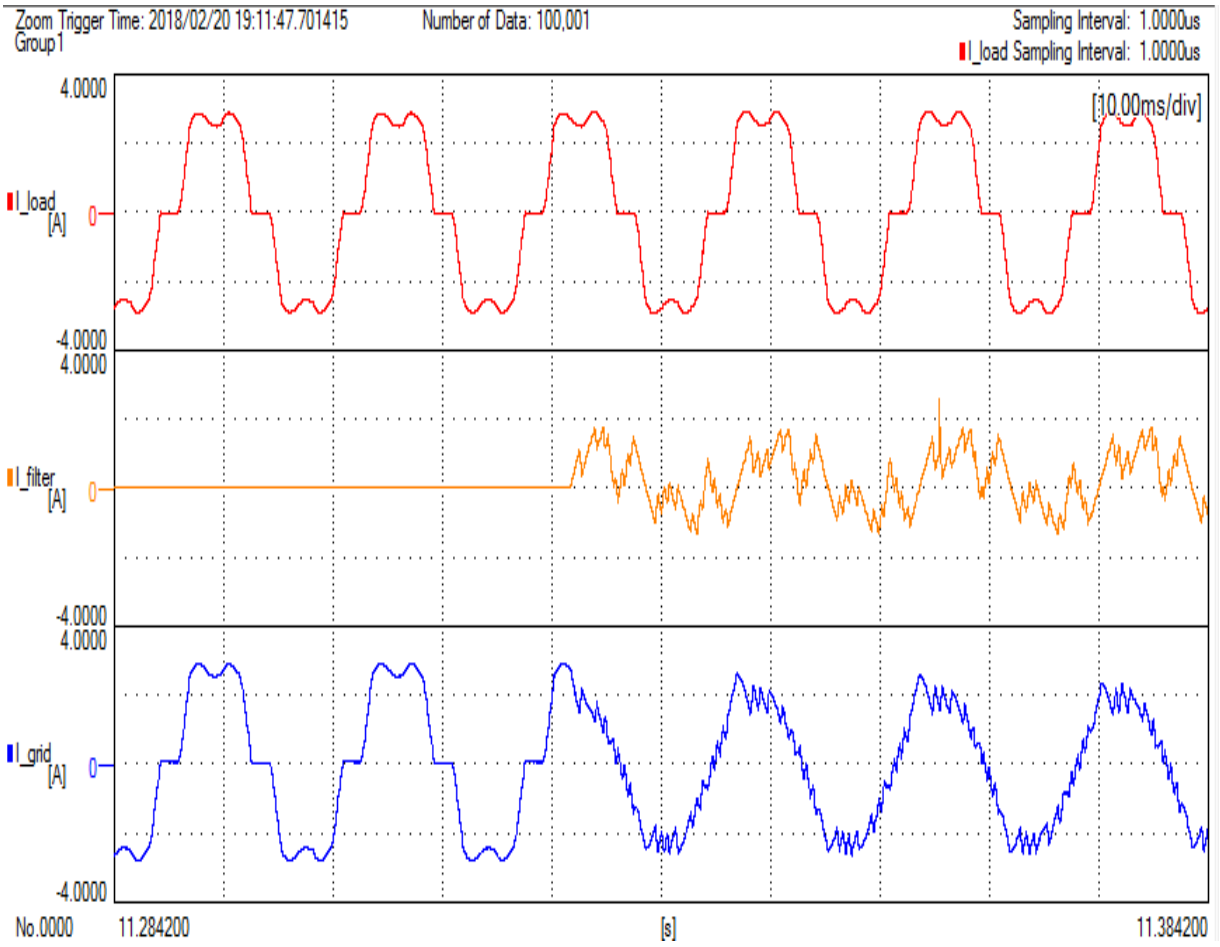

Figure 3.25 Harmonic distortion case study: Experimental results for peak shaving and active filtering: load current, injected filter current, and grid current.

Table 3.11 Harmonic distortion case study summary of experimental results for peak shaving and active power filtering.

	Before peak shaving and filtering	After peak shaving and filtering
	Phase A	Phase A
Phase voltage (V)	30.295	30.608
Line current (A)	2.1571	1.6991
Three phase active power (W)	175.9	147.1
PF	0.95146	0.97595
THD (%)	20.815	14.079

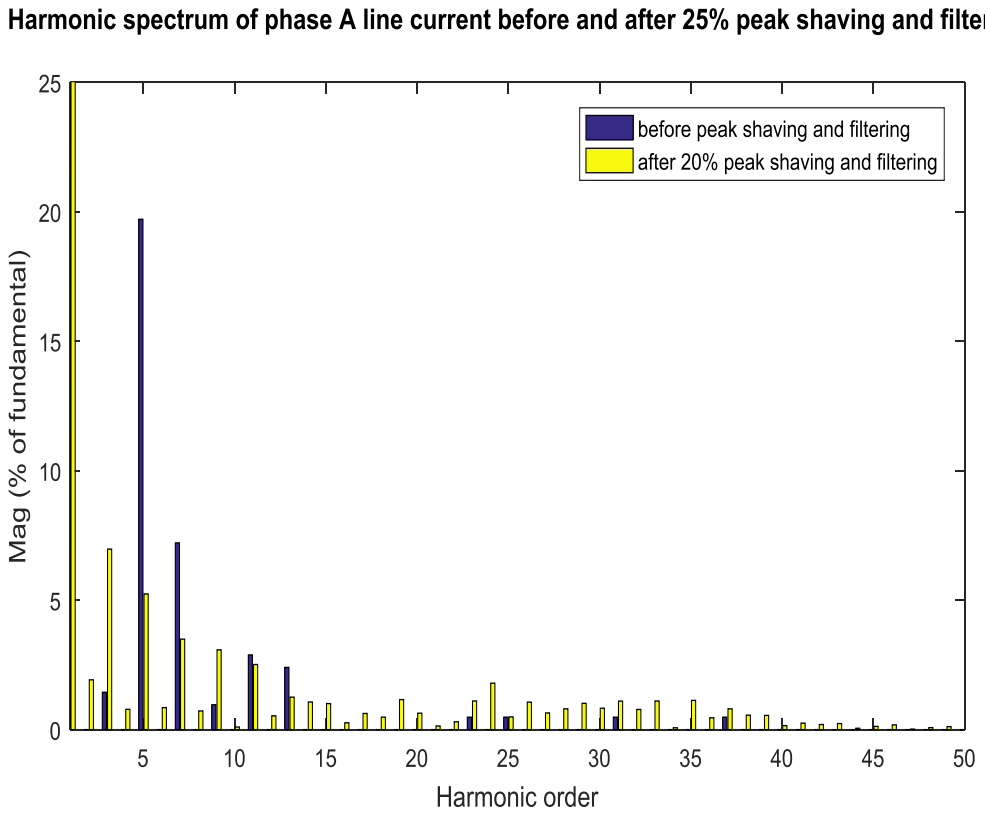

Figure 3.26 Harmonic distortion case study: Harmonic spectrum of phase A line current before and after peak shaving and active power filtering.

Table 3.12 Experimental performance summary for harmonic distortion case study with the different shave levels and active power filtering.

Shave level (%)	Three phase active power from grid (W)	PF	THD (%)
10	169.8	0.983	10.906
15	164.2	0.982	12.287
20	153.7	0.9797	13.253
25	147.1	0.9776	14.544

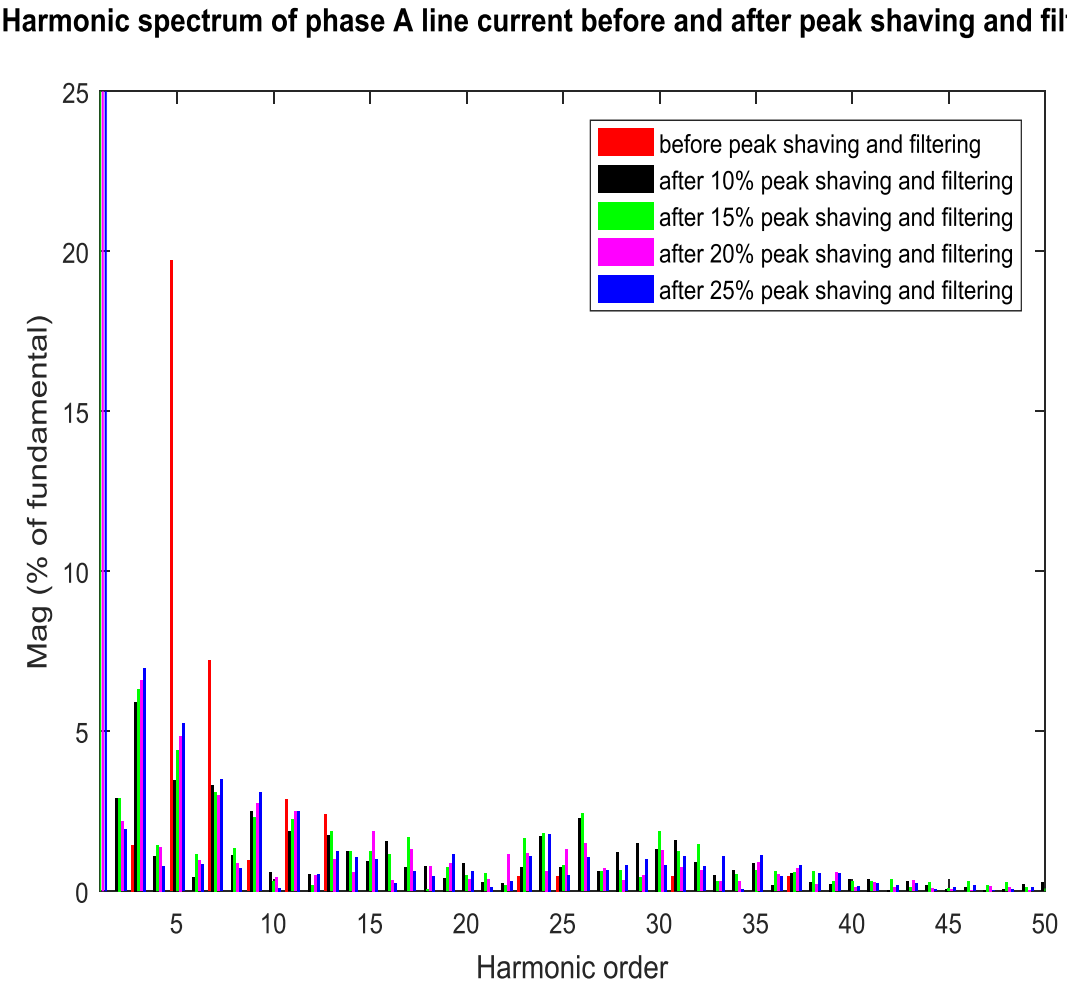

Figure 3.27 Harmonic distortion case study: Harmonic spectrum of phase A line current before and after different shave levels and active power filtering.

3.3.2.3 Case Study Two: Performance at a Low PF:

3.3.2.3.1 Active Power Filtering:

The experimental setup is run with the control scheme set for active filtering. The PF is improved from 0.6 to 0.98 with a slight increase in the THD from 7.312% to 7.789%. Figure 3.28 shows the experimental results. Table 3.13 summarizes the filtering function. Figure 3.29 compares the harmonic spectrum of phase A line current before and after the application of the filter.

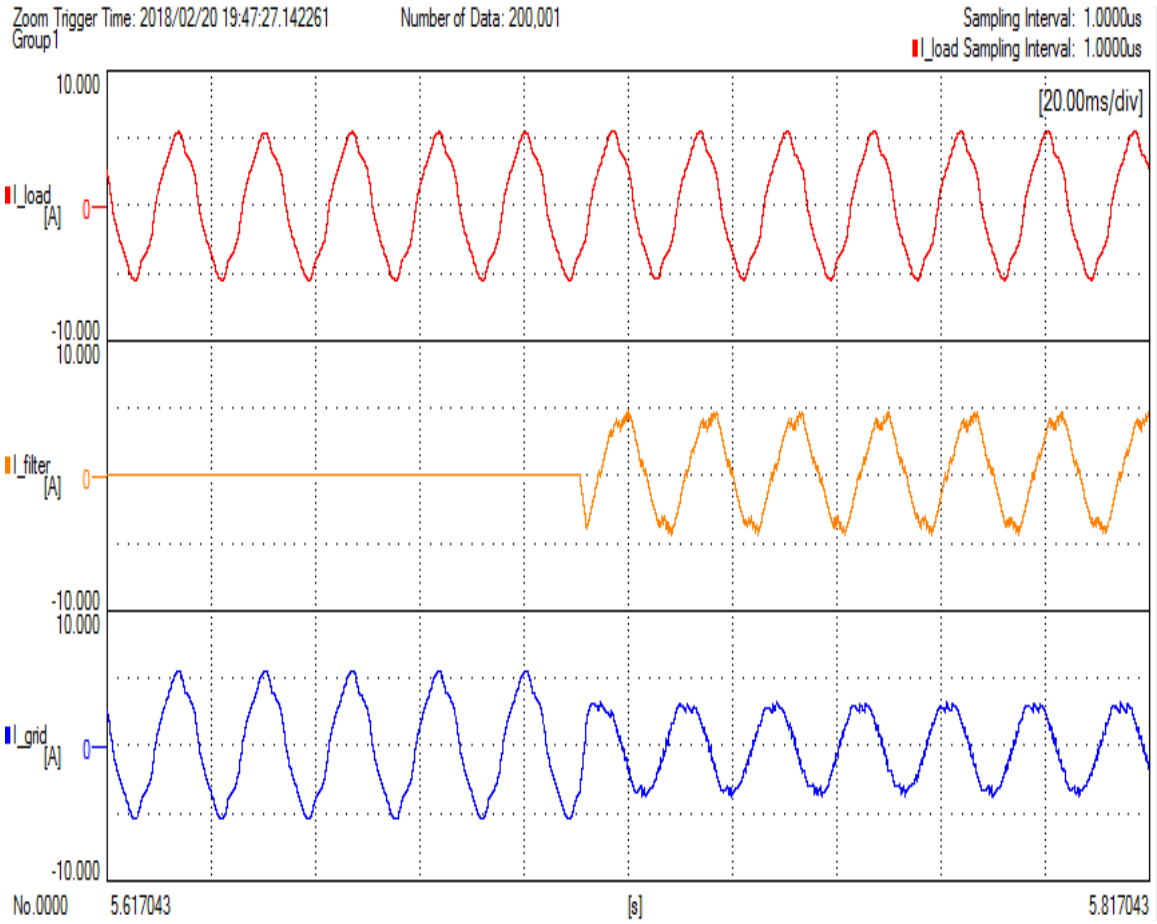

Figure 3.28 Low power factor case study: Experimental results as an active filter, load current, injected filter current, and grid current, respectively.

Table 3.13 Low power factor case study summary of experimental results for active power filtering.

	Before filtering	After filtering
	Phase A	Phase A
Phase voltage (V)	17.866	18.078
Line current (A)	3.6941	2.3869
Three phase active power (W)	112.2	110.9
PF	0.60669	0.98509
THD (%)	7.312	7.789

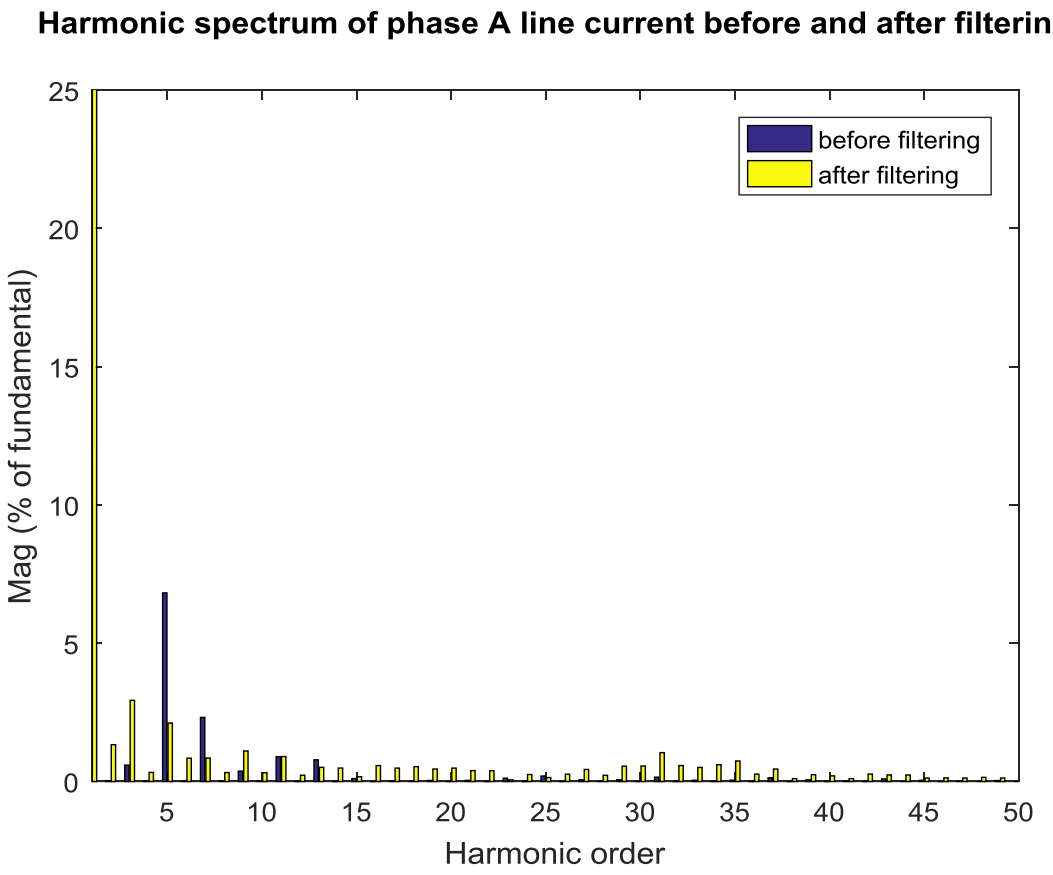

Figure 3.29 Low power factor case study: Harmonic spectrum of line current before and after the filtering.

3.3.2.3.2 Peak Shaving:

The experimental setup is run to achieve peak shaving. The control technique is able to reduce the total power drawn from grid from 112.2 W to 79.3 W. The THD is increased to 8.27% and the PF dropped to 0.46835. Figure 3.30 shows the experimental results. Table 3.14 summarizes the experimental results and figure 3.31 shows the harmonic spectrum of phase A line current. 10%, 15%, 20%, and 25% peak shaving levels are run on the experimental setup. Table 3.15 summarizes the obtained results for the different shave levels. The values of the THD and PF are the average value for the three phases. Figure 3.32 shows the line current harmonic spectrum before and after the different shave levels.

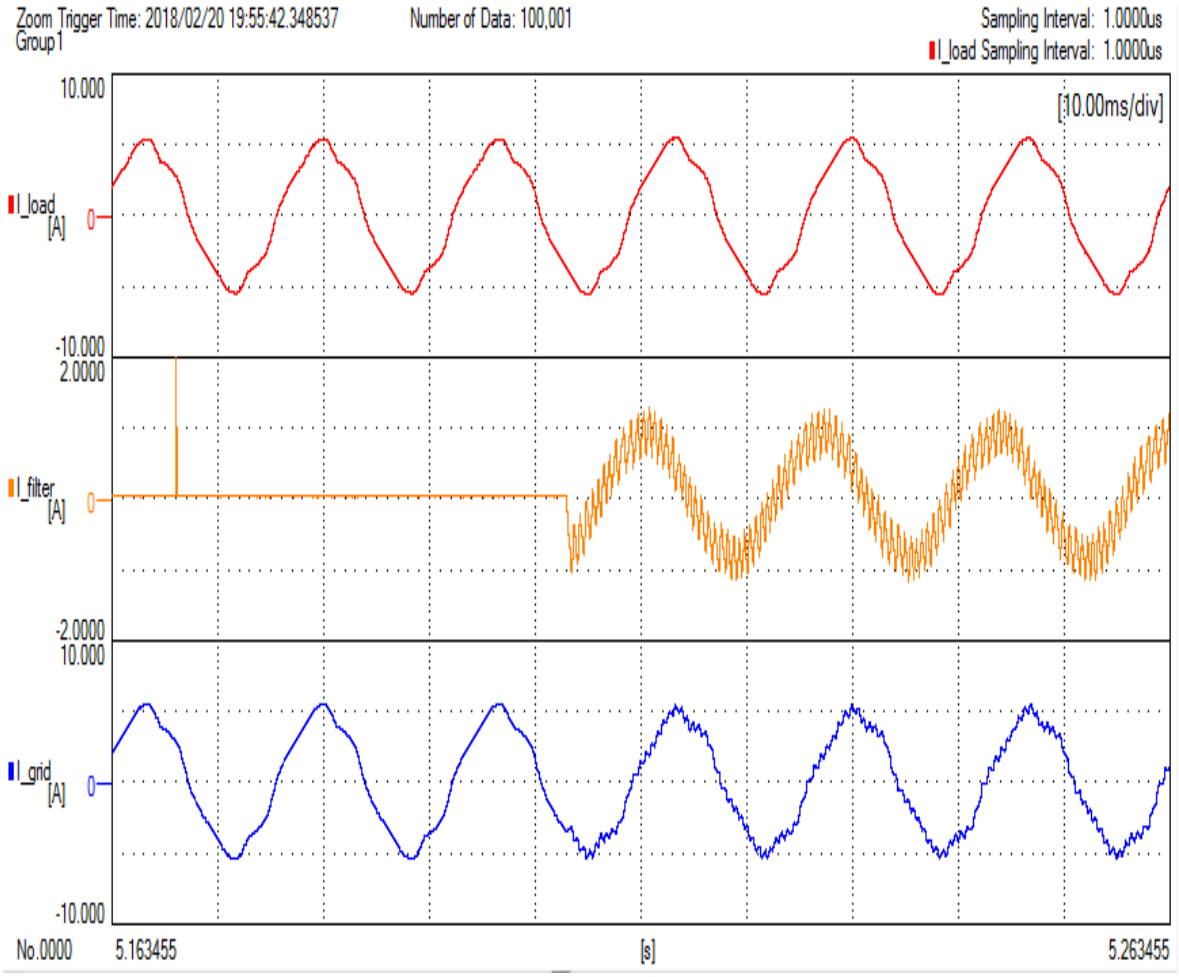

Figure 3.30 Low power factor case study: Experimental results for peak shaving, load current, injected filter current, and grid current, respectively.

Table 3.14 Low power factor case study summary of experimental results for peak shaving.

	Before peak shaving	After peak shaving
	Phase A	Phase A
Phase voltage (V)	17.866	17.885
Line current (A)	3.6941	3.4197
Three phase active power (W)	112.2	79.3
PF	0.60669	0.46835
THD (%)	7.312	8.27

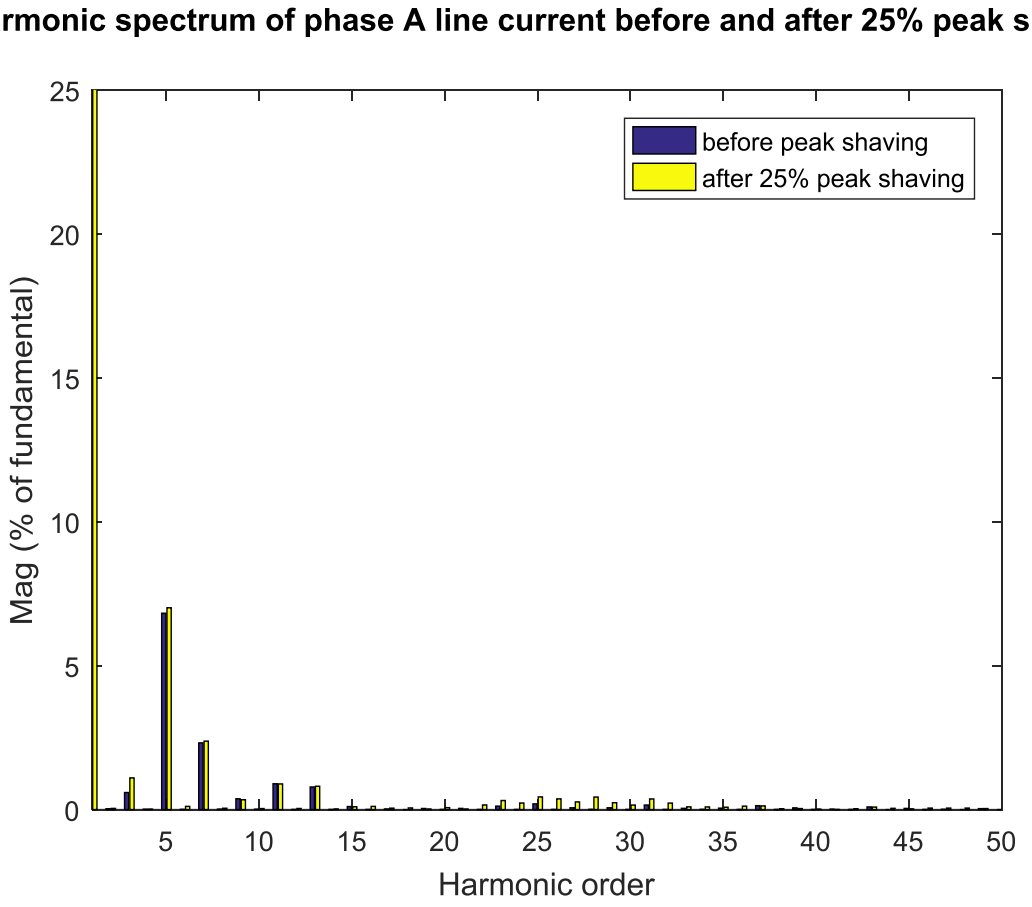

Figure 3.31 Low power factor case study: Harmonic spectrum of phase A line current before and after peak shaving.

Table 3.15 Experimental performance summary for low power factor case study with the different shave levels.

Shave level (%)	Three phase active power from grid (W)	PF	THD (%)
10	95.2	0.533	8.324
15	89.3	0.510	8.444
20	84.15	0.487	8.681
25	79.3	0.464	8.860

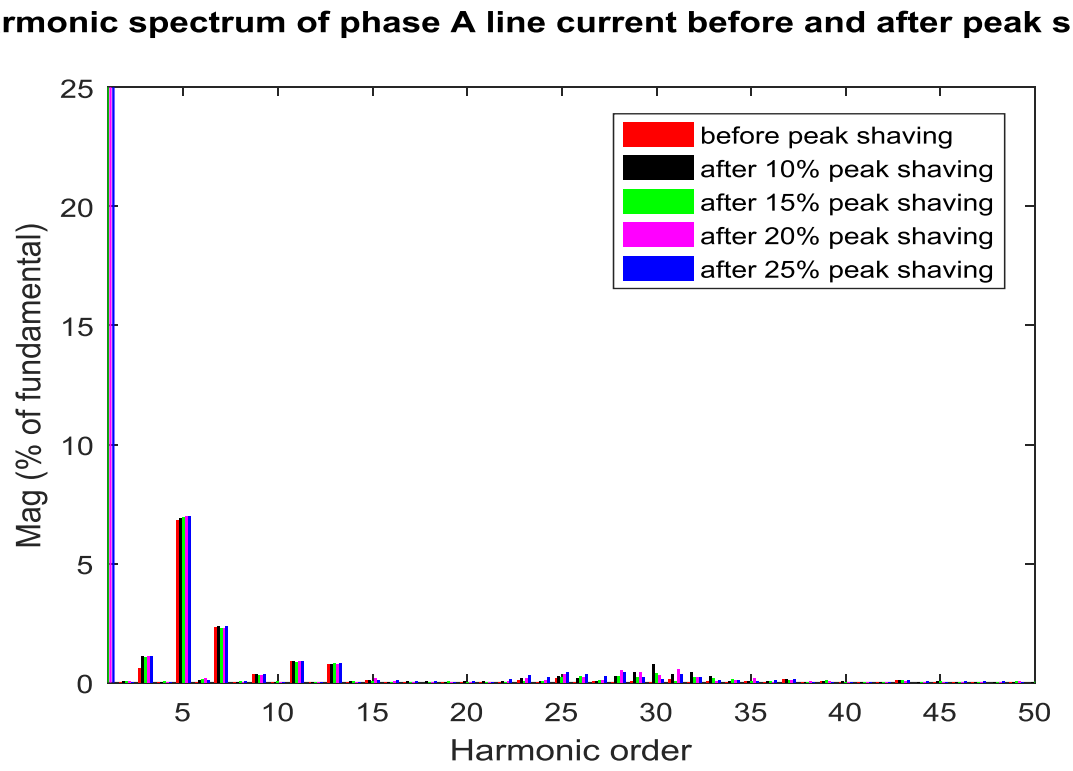

Figure 3.32 Low power factor case study: Harmonic spectrum of phase A line current before and after different shave levels.

3.3.2.3.3 Peak Shaving, Active Power Filtering, and Reactive Power Compensation:

The experimental setup is run for the low PF case. The peak shaving module is set to reduce the power drawn from the grid by 25%. Figure 3.33 shows the experimental results. Table 3.16 summarizes the results. The peak power drawn from grid becomes 87.9 W instead of 112.3 W. The PF is improved from 0.60669 to 0.97562. The THD of the line current is increased from 7.312% to 12.737%.

After the peak shaving and filtering the drawn current from the grid is 1.7705 A, while before the application of the control the system was drawing 3.69 A. The line current harmonic spectrum after the peak shaving and active power filtering is shown in figure 3.34.

Different shave levels are tested and table 3.17 shows the summary of the results and figure 3.35 shows the harmonic spectrum of the line current before and after the application of the control strategy.

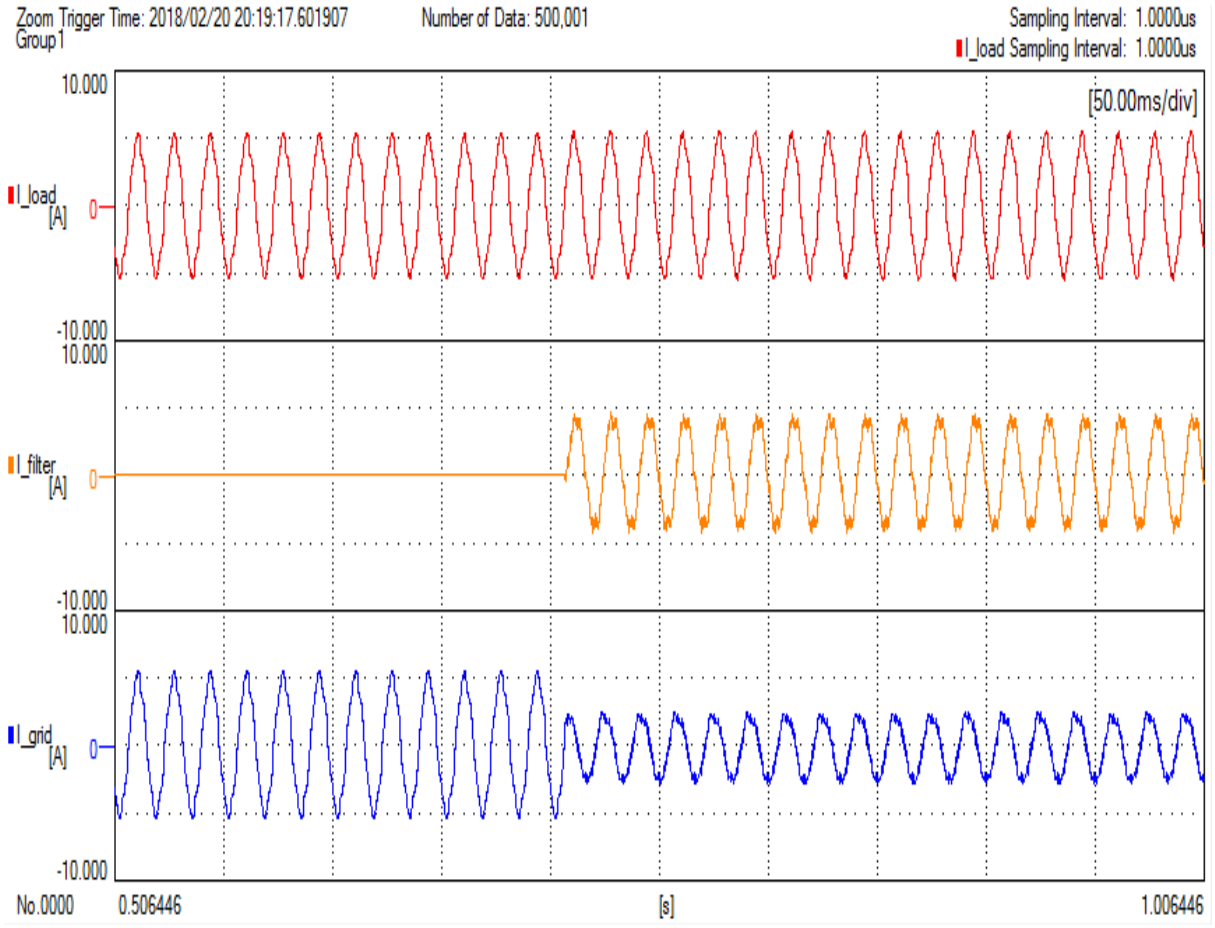

Figure 3.33 Low power factor case study: Experimental results for peak shaving and active filtering, load current, injected filter current, and grid current, respectively.

Table 3.16 Low power factor case study summary of experimental results for peak shaving and active power filtering.

	Before peak shaving and filtering	After peak shaving and filtering
	Phase A	Phase A
Phase voltage (V)	17.866	17.935
Line current (A)	3.6941	1.7705
Three phase active power (W)	112.2	87.9
PF	0.60669	0.97562
THD (%)	7.312	12.737

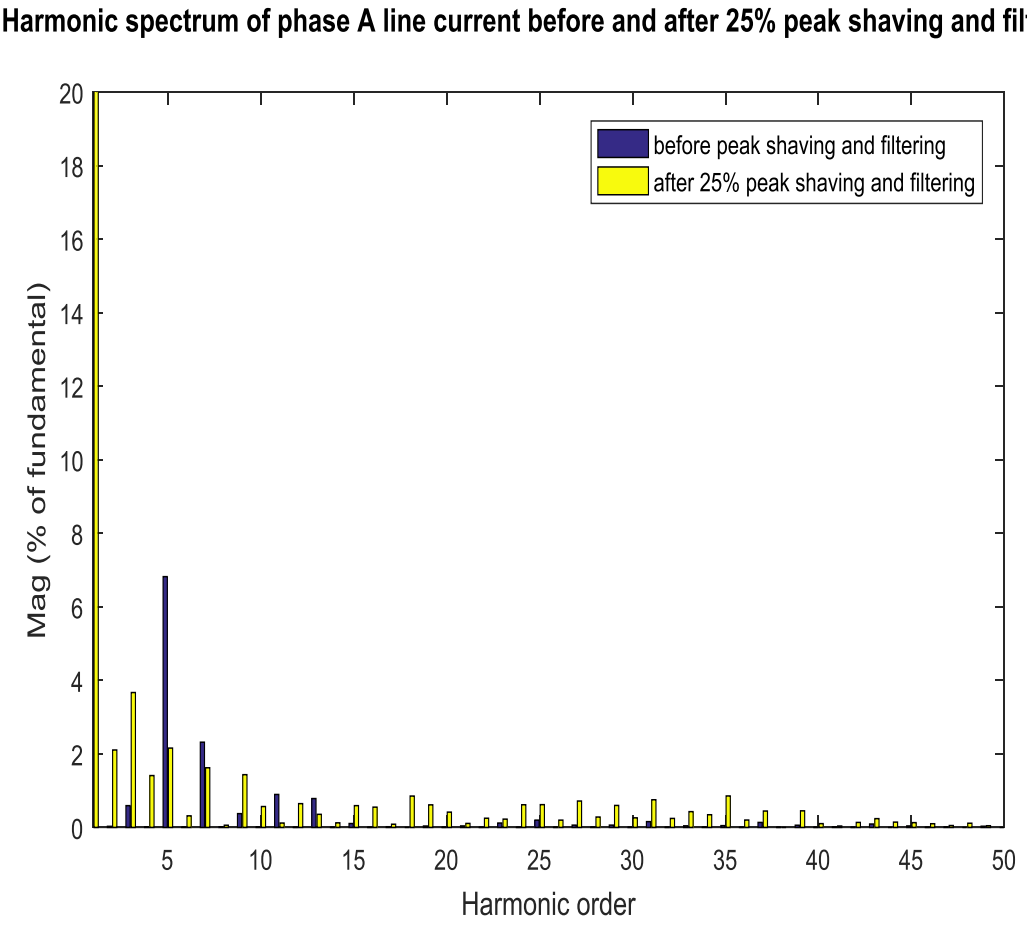

Figure 3.34 Low power factor case study: Harmonic spectrum of phase A line current before and after peak shaving and active power filtering.

Table 3.17 Experimental performance summary for harmonic distortion case study with the different shave levels and active power filtering.

Shave level (%)	Three phase active power from grid (W)	PF	THD (%)
10	101.9	0.9826	9.181
15	96.7	0.9811	9.638
20	92.3	0.9796	10.461
25	87.9	0.9778	11.645

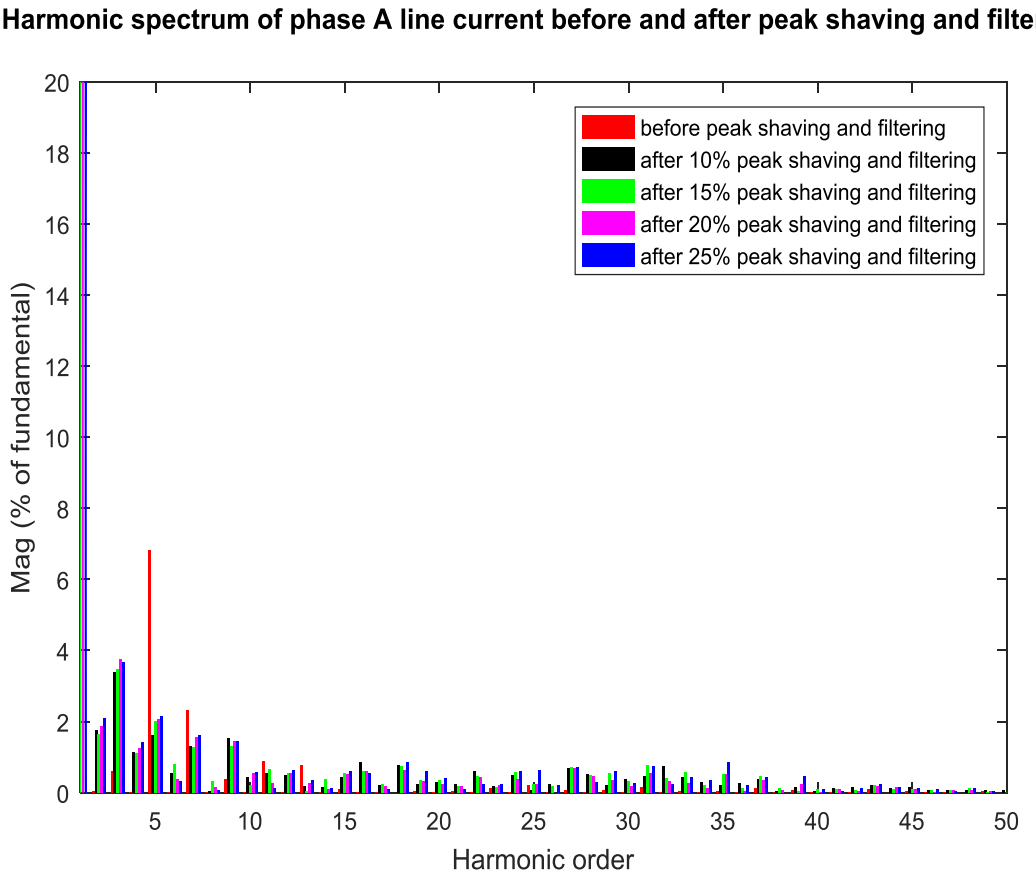

Figure 3.35 Low power factor case study: Harmonic spectrum of phase A line current before and after different shave levels and active power filtering.

3.4 Discussion

The simulation results show that the proposed control technique was able to improve the PF for the two case studies; from 0.956 to 0.9965 when operating under high THD, and from 0.5174 to 0.9958 when operating under low PF. The same observation is to be noted from the experimental results, where the PF was improved from 0.9514 to 0.976 when operating under high THD, when operating under low PF, the proposed control technique improved the PF from 0.6066 to 0.975. Hence, it is clear that the proposed control technique was successful in improving the PF for both case studies in simulation and experimentally.

The proposed control technique was able to reduce the THD when operating under high THD. From 25.02% to 8.62% in the simulation results, and from 20.815% to 14.079% experimentally. However when operating under low PF, the THD increased in the simulation

results from 6.41% to 6.9%, experimentally from 7% to 12.737%. This is because of scaling down the system to a lower voltage level. The scaling was done due to the current ratings of some of the system components used to construct the network in the laboratory. Furthermore, the achieved peak shaving reduced the current drawn from the grid, and since the fundamental component of the drawn current became lower, the effect of the harmonics generated from the HCC and the load become more profound.

3.5 Summary

This chapter proposes a control strategy for voltage source inverters (VSI) used in peak shaving applications, for power factor correction and reactive power compensation. The proposed control utilizes the power electronic converter used in peak shaving applications not only to send power to the load side, but also to control the flow of the reactive power and mitigate the line current harmonics. The proposed control firstly, eliminates the need for capacitor banks, STATCOM, and shunt passive filters, and secondly, achieves peak shaving sending power to the ac side, and finally, mitigates the line current harmonics produced by the loads reducing the line current THD. The simulation results and the experimental validation show the expected power quality improvements from the proposed control technique. Overall, the proposed strategy was able to properly operate under high harmonic distortion reducing the THD seen in the line current, and improving the PF. Hence, considerably improving the power quality of the power system.

CHAPTER 4

Modelling and Operation of Electric Drives from Photovoltaics Cells (PV)

4.1 Introduction

This chapter investigates the behavior of three phase induction motors when operated from Solar Photovoltaic cells (PVs). In industrialized countries, electrical machinery use a significant portion of the generated electrical power [38], namely, induction motors are widely used in industry due to their relative low cost, ruggedness, and simplicity [39].

In recent years, the semiconductor industry has developed rapidly, which made controlling induction motors easier than earlier times. Variable Frequency Drives (VFD's) are used to control the performance of the induction motor. By changing the voltage level and the frequency at which the voltage is fed to the motor, one can control the rotational speed and the produced torque of the induction motor.

The common control schemes used to control three phase induction motors are [40-42]:

- Scalar control or constant V/F control: in this technique, the ratio between the motor rated phase voltage and the rated frequency is kept constant to maintain the stator flux linkage. However, low speed operation for this technique is considered a problem because the voltage drop across the stator resistance at low speed is no longer negligible [43]. This control technique is not as accurate as the other techniques. However, it is the easiest to implement and the cheapest. Some modifications have been added to improve the accuracy of the control of this scheme. Slip estimation methods, and closed loop control using PID controllers are among the most popular variations [44, 45].
- Field Oriented Control (FOC): in this technique, the three phase stator currents are transformed into two phase equivalent components. The two current components control the torque and the stator magnetic flux, respectively. This technique is more complex when compared with the scalar control technique [41].

- Direct Torque Control (DTC): In FOC drives, the stator currents are decomposed into the torque component and flux component. These components are obtained from the stator current, thus a current control technique is required to get the required current references. On the other hand, in DTC, the voltage drop across the stator resistance is negligible, thus at low speeds this technique is problematic [42].

In general, the choice of the control scheme depends on the requirements of the applications. Each control technique has its advantages and disadvantages. For applications where the control accuracy is important the FOC and DTC provide better control, while for application where the speed control accuracy is not of great importance, scalar control is the cheapest and the easiest to implement.

4.2 Solar Photovoltaics in Industrial Sector

With the dropping costs of PV, the integration of PV in the industrial sector has grown by rapidly [25]. This encourages companies to reduce their demand of both power and energy from the grid by utilizing different peak shaving techniques by either generating power locally, or utilizing Energy Storage Systems (ESS). Since induction motors use around 68% of the electrical power generated therefore, it is of great importance to investigate the behavior of induction motors and their electrical drives when supplied from PVs.

4.3 Case Study

In this section, a case study is implemented to investigate the behavior of induction machines and electrical drives when fed from PV.

4.3.1 Induction Motor

The Induction motor used for the case study is a three phase, 3 HP, Y- connected, two pole induction motor, rated at 220 V, 60 Hz, and 3450 RPM. The equivalent circuit of the motor was not available in the datasheet. Therefore, the equivalent circuit has to be extracted from the motor. To extract the equivalent circuit parameters in figure 4.1, Method 1 of IEEE Std 112^{TM} – 2004 is used [46].

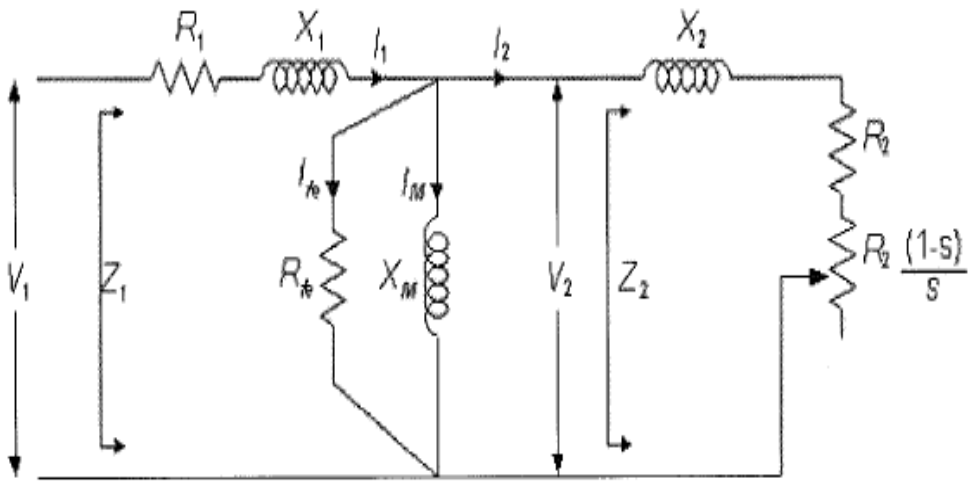

Figure 4.1 Per-phase equivalent circuit of three phase induction motor [46].

Where

Table 4.1 Equivalent circuit parameters.

Variable	Description	Unit
V_1	Phase voltage	V
V_2	Rotor phase voltage referred to stator	V
f	Frequency	Hz
I_1	Stator current	A
I_2	Rotor current referred to stator	A
I_m	Magnetizing current	A
I_{fe}	Core loss current	A
m	Number of phases	N/A
R_1	Stator resistance	ohms
R_2	Rotor resistance referred to stator	ohms
R_{fe}	Core loss resistance	ohms
G_{fe}	Core loss conductance	Siemens
X_1	Stator leakage reactance	ohms
X_2	Rotor leakage reactance referred to stator	ohms
X_m	Magnetizing reactance	ohms
B_m	Magnetizing susceptance	Siemens
Z	Impedance per phase	ohms
Z_2	Rotor impedance referred to stator	ohms
s	Slip	%

This method is based on three tests to determine the parameters of the induction motor

- DC test**:**

This test is used to extract the stator resistance by exciting the phases with DC voltage. The resistance is calculated by dividing the DC voltage by the DC current. Based on the stator winding connection, the per-phase resistance is calculated. For instance, if the motor is Y- connected, when exciting two phases, the resistance is equal to twice the per phase resistance, thus the per-phase resistance is simply half of the measured resistance.

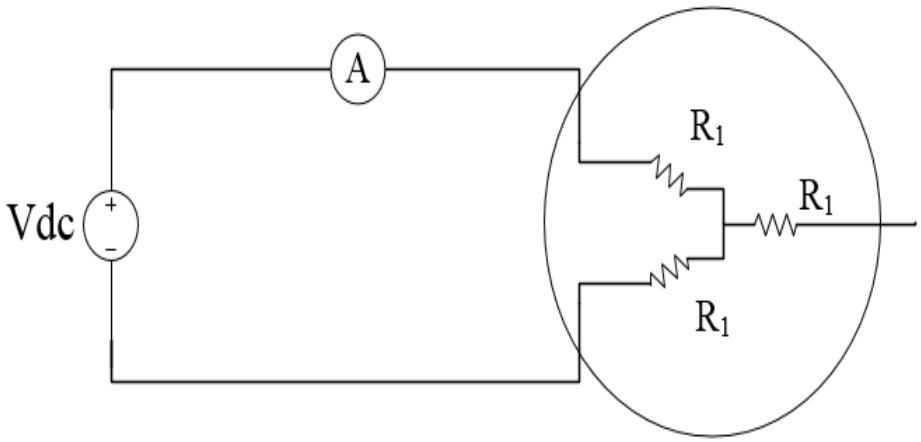

Figure 4.2 DC test of a three phase induction motor.

- Locked rotor test**:**

During this test, the rotor is locked mechanically to prevent it from rotating, and the applied voltage is increased gradually until the full load current flows in the stator coils. When locking the rotor, the slip is equal to one, thus the magnetizing branch of the induction motor can be ignored as seen from figure 4.3. When the rotor is locked, the full load rated current will flow at low voltage level much lower than the rated motor voltage. The instantaneous values of the three phase currents and voltages are recorded and the instantaneous power is calculated.

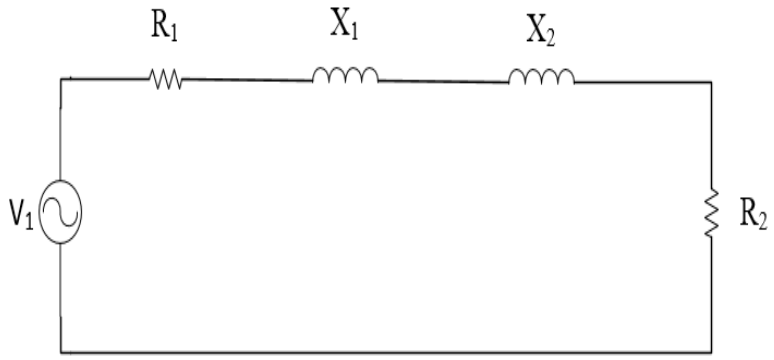

Figure 4.3 Locked rotor test of three phase induction motor.

- No load test**:**

This test is performed by running the motor at rated voltage and frequency with no load connected. In order to separate the losses of the motor at no load, a range of voltages should be tested, ranging from 125% of rated voltage down to the point where voltage reduction increases drawn current. By performing the test at different voltages, one can separate the friction and windage losses by extrapolating to zero voltage after subtracting the stator ohmic losses. After calculating the friction and windage losses, one can calculate the core loss at the rated voltage after subtracting the stator ohmic losses and the friction and windage losses from the total losses measured at rated voltage. By running the motor at no load, the slip is considered very small and negligible, hence, the rotor resistance is very high compared with the magnetizing branch resistance. Therefore, the motor equivalent circuit becomes as seen in figure 4.4.

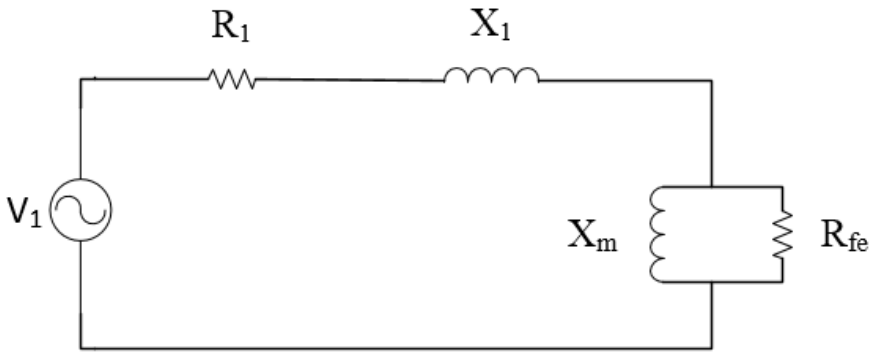

Figure 4.4 No load test of three phase induction motor.

After performing these tests, the equivalent circuit parameters in figure 4.1 are extracted and shown in table 4.2:

Table 4.2 Extracted equivalent circuit parameters.

Variable	Value
R_1	0.6832 Ω
R_2	0.7265 Ω
R_{fe}	409.714 Ω
X_1	1.0618 Ω
X_2	1.5848 Ω
X_m	42.985 Ω

4.3.2 Electrical Motor Drive

The induction motor parameters are the starting point in designing or selecting the electrical drive to be used [47]. The selection of the drive and the control scheme used depends on the nature of the application and the load to be driven by the motor. In this case study, the electrical drive is chosen to be a three phase two level inverter, and it consists of a full bridge diode rectifier to feed a DC bus, which is connected to a capacitance of 8.5 mF to reduce the ripples in the DC bus voltage. Three IGBT legs are connected to the DC bus, each leg consists of two IGBT switches.

The selected control scheme is an open loop V/f scalar control, where the ratio of the rated phase voltage to the rated frequency is kept constant to maintain a constant stator flux. First step in designing the scalar control is to calculate the constant V/f ratio. The rated phase voltage is 120 V, and the rated frequency is 60 Hz. Therefore, the constant scalar control ratio is calculated using equation 4.1. The frequency is expressed in radians rather than Hz. By keeping this ratio constant, the stator flux is kept constant and hence, the air gap flux is constant as well.

$$\frac{V}{f} = \frac{120}{2 \times \pi \times 60} = 0.31830 \sim 0.32 \qquad (4.1)$$

The desired speed reference in RPM is translated to rad/s. The speed is then used to calculate the required phase voltage based on the V//f ratio. The expected voltage drop in the stator resistance is then added to the calculated phase voltage. Since the induction motor has two poles, the electrical speed at which the magnetic field is rotating is equal to the mechanical speed of the

rotor when ignoring the slip speed. Integrating the speed reference will produce the required frequency for the three phase modulating references. This is shown in figure 4.5.

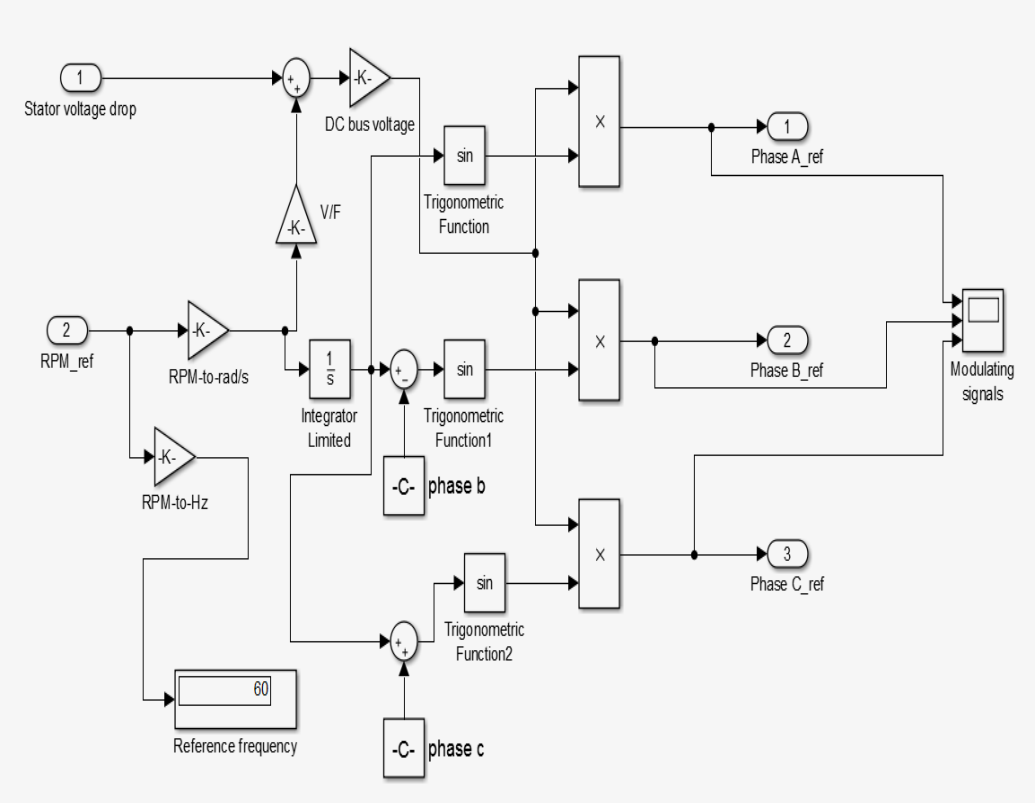

Figure 4.5 Scalar V/F controller design.

The resulting three phase modulating signals are described by the following set of equations:

$$V_{A\_ref} = V_1 \times \sin(wt) \qquad (4.2)$$

$$V_{B\_ref} = V_1 \times \sin\left(wt - \frac{2\pi}{3}\right) \qquad (4.3)$$

$$V_{C\_ref} = V_1 \times \sin\left(wt - \frac{4\pi}{3}\right) \qquad (4.4)$$

The three reference signals are then sent to a two level PWM controller to generate the gating signals for the drive switches. The RMS value of the fundamental component of the line to line voltage is calculated using [48]:

$$V_{LL\_1} = \frac{\sqrt{3}}{2\sqrt{2}} \times m_a \times V_{dc} \qquad (4.5)$$

Where m_a is the modulation index, and V_{dc} is the DC bus voltage.

4.3.3 Validation of Motor Model

The extracted equivalent circuit parameters of the case study motor in table 4.2 must be validated. The factors that determine the accuracy of the extracted parameters are the drawn line currents, the speed of the motor, and the line to line voltage that appears across the motor terminals. The validation is done by simulating the obtained parameters in Simulink as shown in figure 4.6 at different frequencies. The same setup is built in the laboratory, and figure 4.7 shows the experimental setup used to validate the extracted equivalent circuit. The step down transformer is used to supply power to the full bridge diode bridge rectifier installed with the inverter. A capacitor branch is connected with the DC bus to reduce the ripple in the voltage produced from the full bridge diode rectifier. The determining factors are compared at each frequency.

The used motor has a synchronous speed of 3600 RPM. In order to load the motor an eddy current brake is used to produce an opposing torque on the motor shaft. However, the brake is rated for a maximum rotation speed of 1800 RPM, while the motor is spinning at 3600 RPM, hence, a gear box is used to reduce the speed.

The synchronous speed of the motor at each frequency is calculated using:

$$N_{Synchronous} = \frac{120 \times f}{p} \qquad (4.6)$$

Where p is the number of poles in the motor, and f is the frequency. The corresponding reference speeds are calculated in table 4.3.

Table 4.3 Reference speeds for motor validation.

Frequency (Hz)	Speed (RPM)
60	3600
50	3000
30	1800

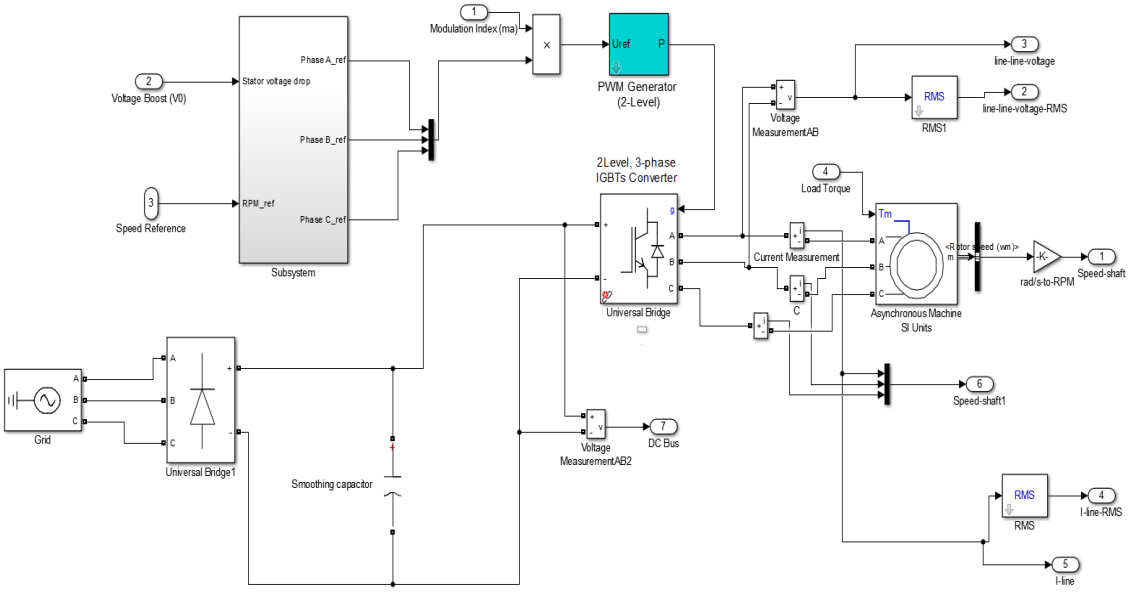

Figure 4.6 System simulation in Simulink.

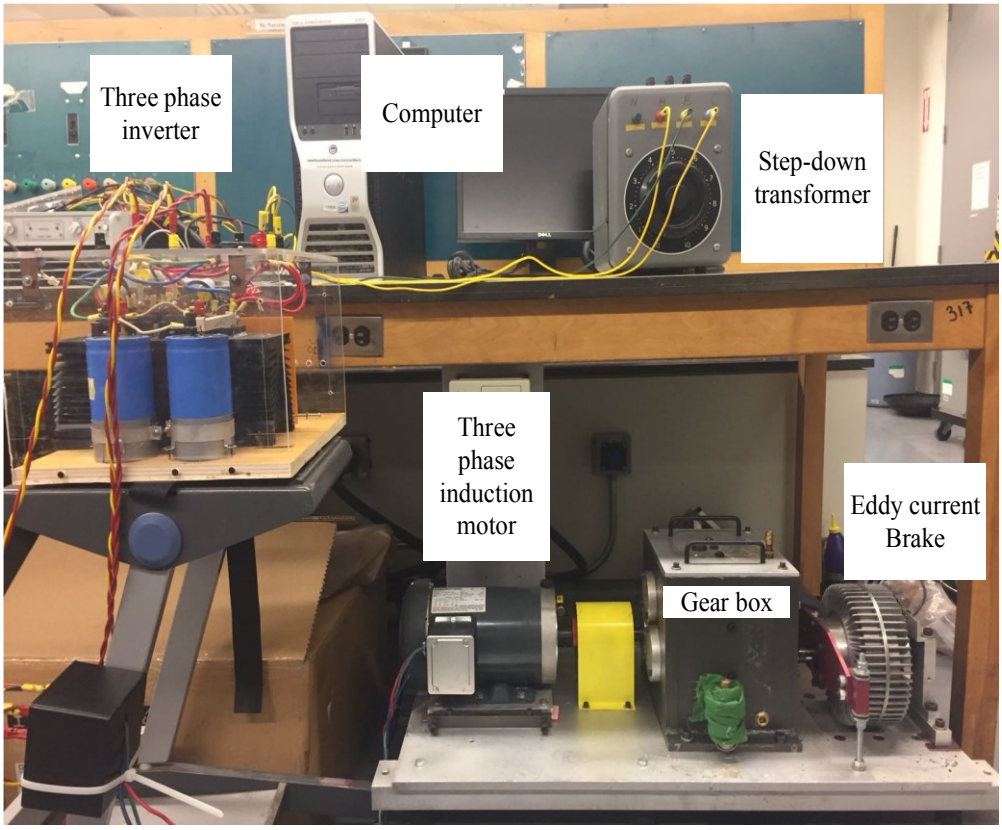

Figure 4.7 Experimental setup in the laboratory.

- Operation at 60 Hz

At 60 Hz, the reference speed sent to the controller is 3600 RPM. As seen from figure 4.6, the controller receives the speed reference and the expected voltage drop across the stator resistance (i.e. Boost voltage) and generates the three modulating signals.

The experimental setup in figure 4.7 is run first to obtain the actual values for comparison. The eddy current brake is used to fully load the motor, and the motor is left running for three hours to reach the rated temperature. After reaching steady state, the three phase currents to the motor are captured using currents probes connected to the motor terminals. Figure 4.8 shows the actual three phase currents. The RMS values of the drawn currents are 7.34 A, 7.57 A, and 7.66 A, for phases A, B, and C, respectively.

The line to line voltage, and the DC bus voltage are measured across the motor terminals shown in figure 4.9. The DC bus voltage is found to be 278 V, and the RMS value of the line to line voltage is 199.97 V. The actual speed is measured using a portable speed sensor, at 60 Hz reference, the measured motor speed is 3440 RPM.

The Simulink model in figure 4.6 is then run with the same references. The drawn currents after steady state are shown in figure 4.10, and the RMS values for phases A, B, and C, are 7.53 A, 7.6 A, 7.6 A, respectively. The DC bus voltage is 278.32 V, and the RMS value of the line to line voltage is 204.4 V. Figure 4.11 shows the simulated line to line voltage and the DC bus voltage waveforms. The rotor speed is found to be 3390 RPM. Table 4.4 summarizes the comparison between the experimental and simulation results.

Table 4.4 Equivalent circuit validation at 60 Hz.

60 Hz	Experimental setup	Simulink model
DC bus voltage (V)	278.0	278.316
RMS line to line voltage (V)	199.97	204.4
RMS line Currents (A)	7.34 7.57 7.66	7.582 7.596 7.591
Speed (RPM)	3440	3390

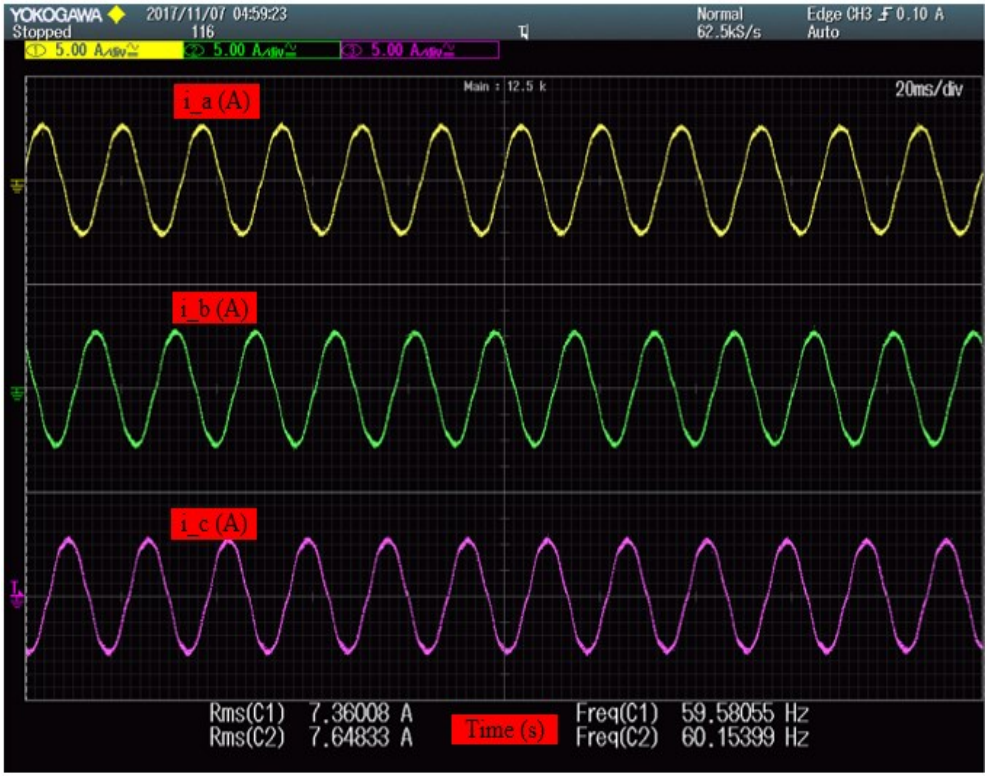

Figure 4.8 Three phase actual currents drawn by the motor at 60 Hz.

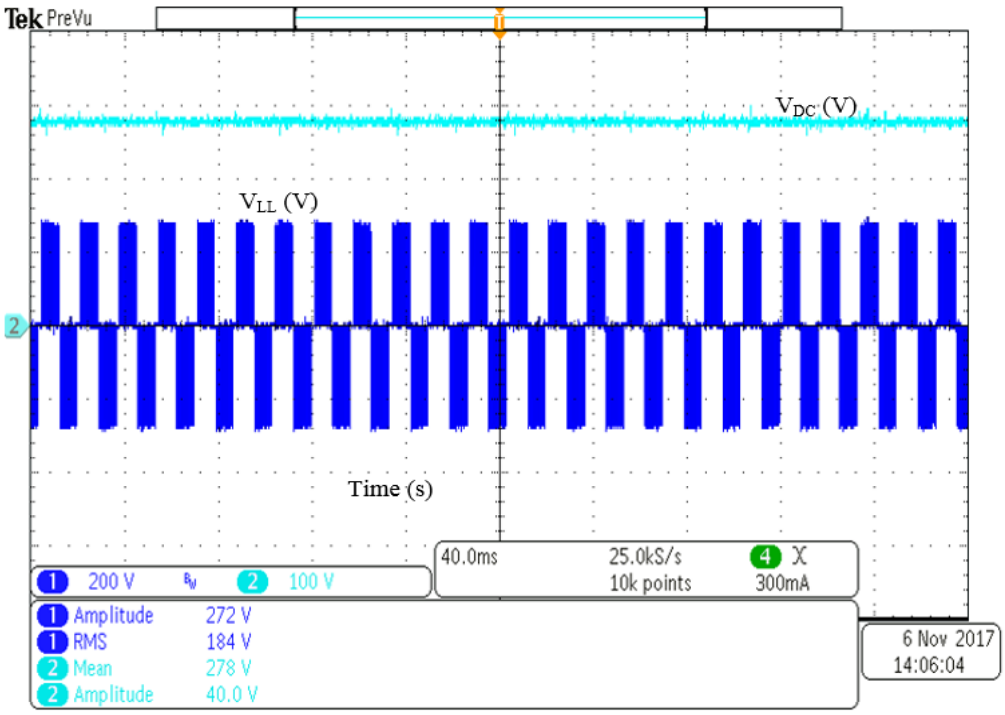

Figure 4.9 DC bus voltage and line to line voltage across the motor terminals at 60 Hz.

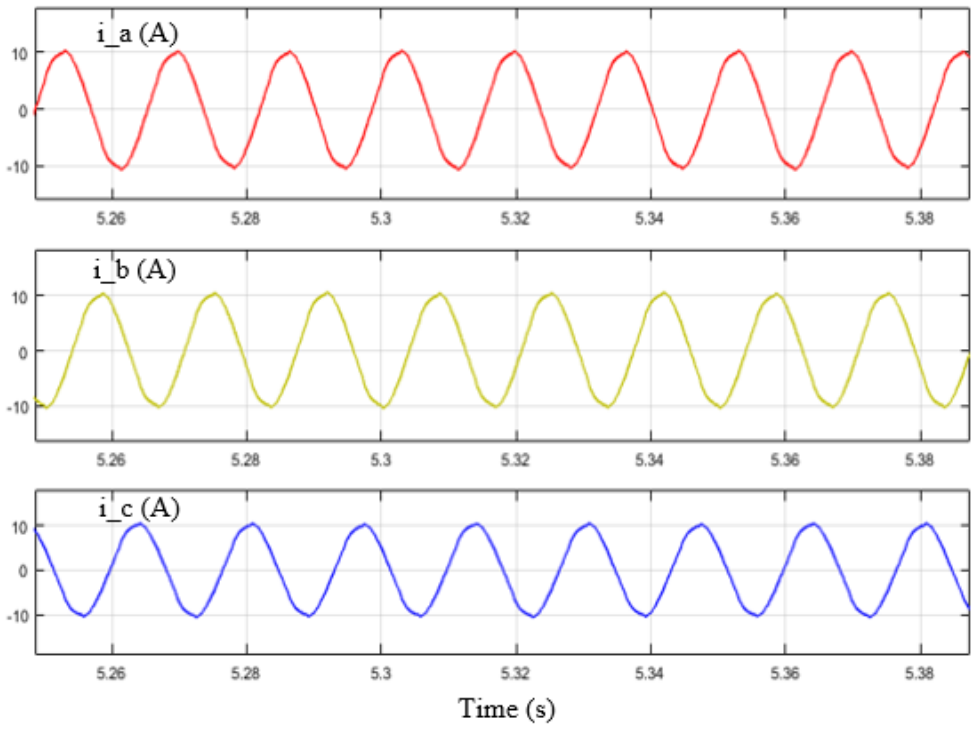

Figure 4.10 Three phase current drawn by the motor in Simulink at 60 Hz.

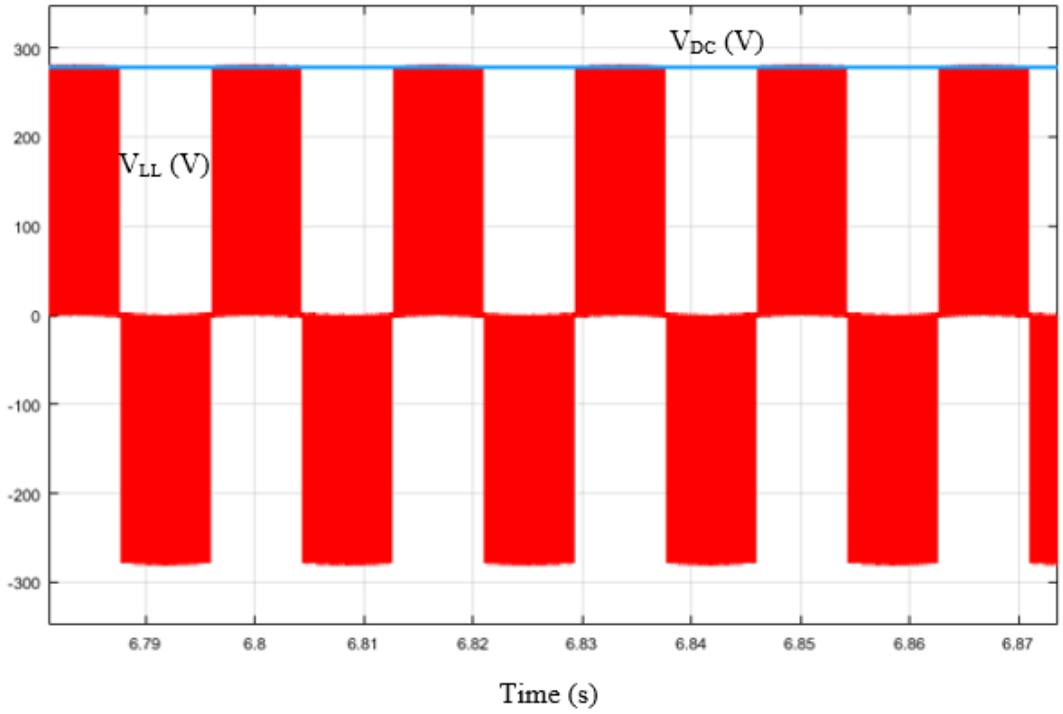

Figure 4.11 DC bus voltage and line to line voltage across the motor terminals in Simulink at 60 Hz.

- Operation at 50 Hz

At 50 Hz, the reference speed sent to the controller is 3000 RPM, and the same procedure used at 60 Hz is used at 50 Hz. Table 4.5 summarizes the comparison, and the figures below display the line currents and line to line voltages for both the experimental setup and the Simulink model.

Table 4.5 Equivalent circuit validation at 50 Hz.

50 Hz	Experimental setup	Simulink model
DC bus voltage (V)	283	283.3
RMS line to line voltage (V)	187.92	194.9
RMS line Currents (A)	5.75 5.93 5.97	5.638 5.629 5.620
Speed (RPM)	2896.8	2848.88

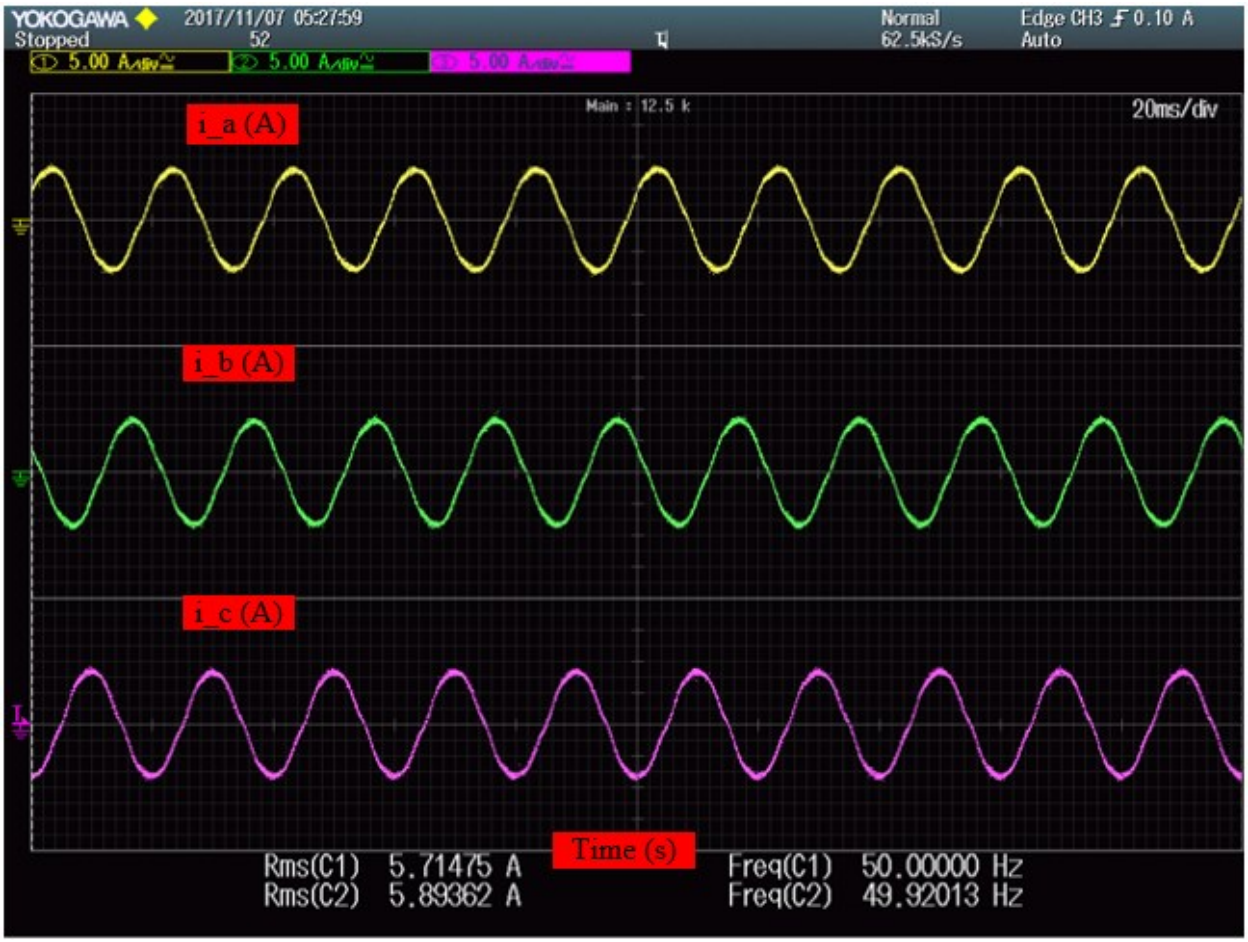

Figure 4.12 Three phase actual currents drawn by the motor at 50 Hz.

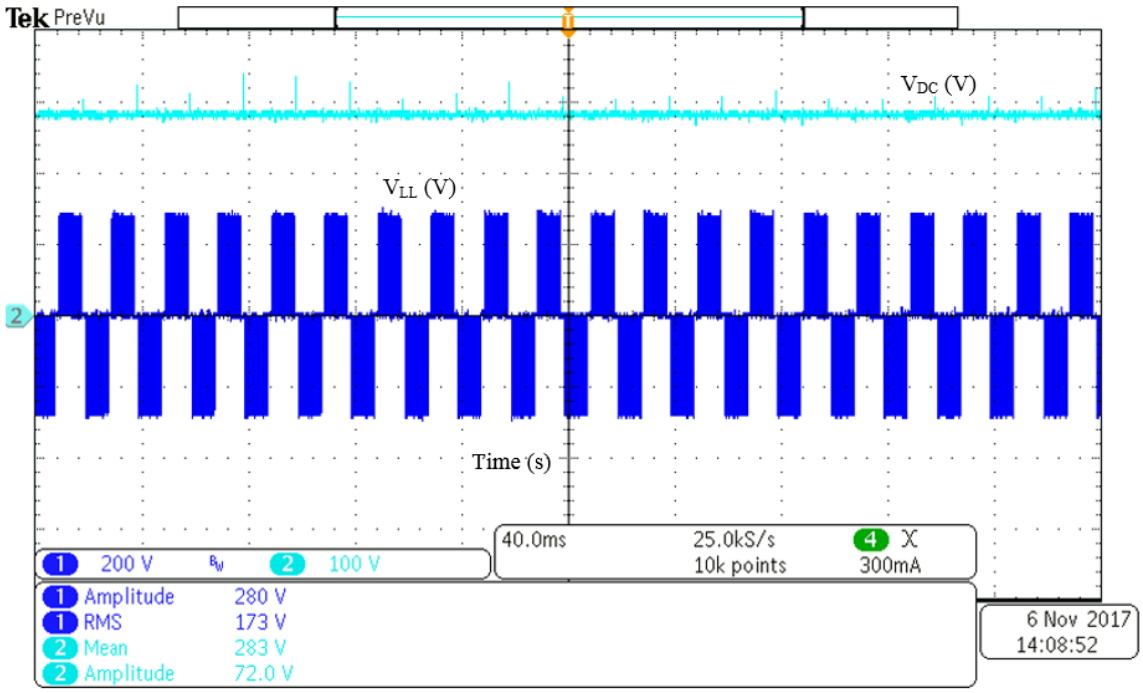

Figure 4.13 DC bus voltage and line to line voltage across the motor terminals at 50 Hz.

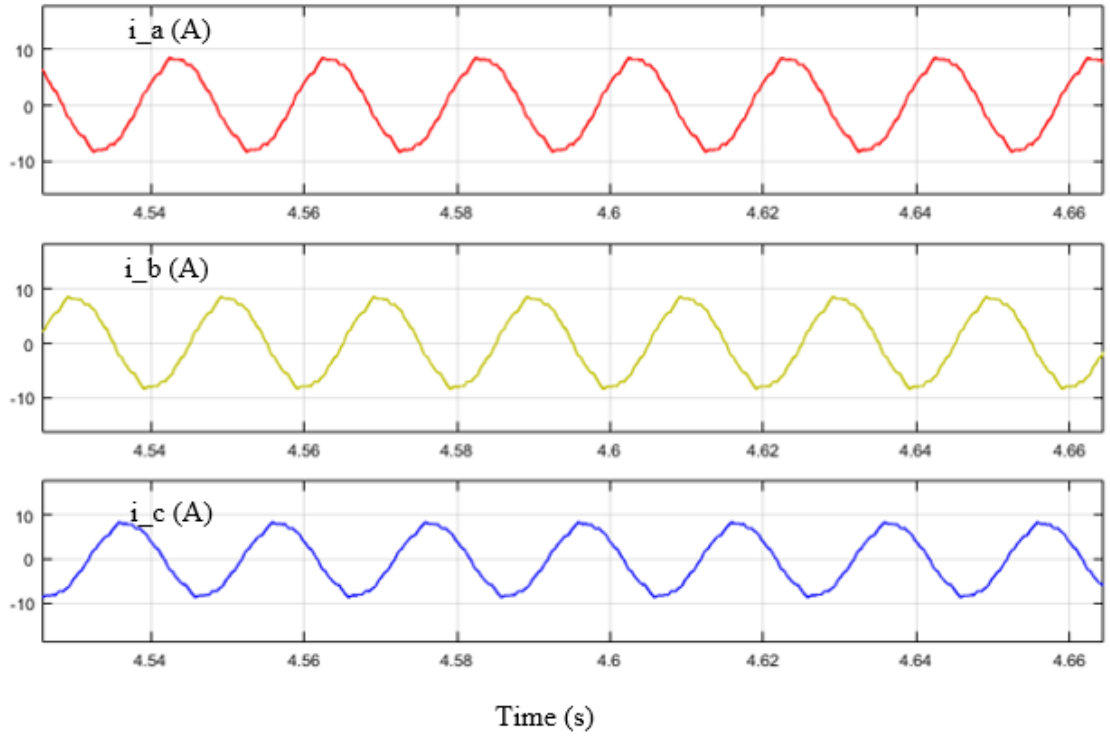

Figure 4.14 Three phase current drawn by the motor in Simulink at 50 Hz.

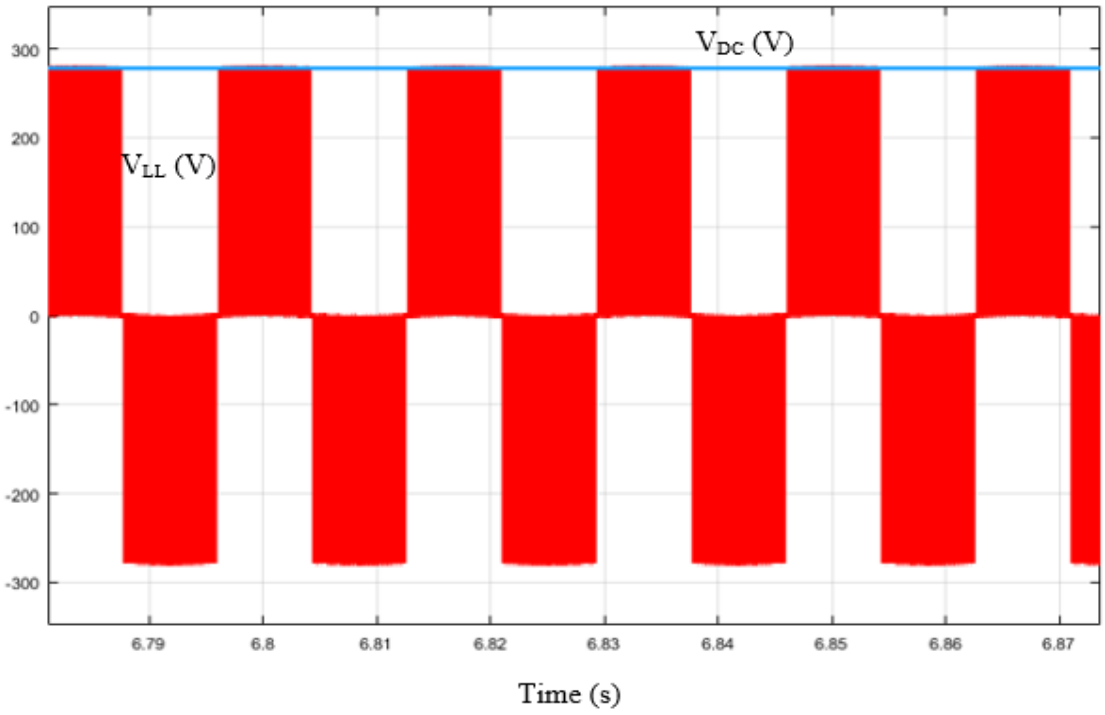

Figure 4.15 DC bus voltage and line to line voltage across the motor terminals in Simulink at 50 Hz.

4.3.4 Solar Array Simulator

The last component of the case study is the PV simulator. Chroma solar array simulator model 62000H-S in figure 4.16 is programed to simulate the PV array feeding the drive and the motor. The solar array generates voltage and currents that mimics voltages and currents (I-V characteristics) generated from actual solar photovoltaics cells.

The voltage and current produced by the simulator are based on the equivalent circuit of the photovoltaic cell in figure 4.17 [49-51]. The equivalent circuit consists of a current source I_{ph}, a diode connected in parallel with the current source, and the leakage resistance of the diode p-n junction is represented by a shunt resistance R_p. The resistances of other structural elements are lumped in a series resistance R_s. Table 4.6 shows the description of the variables used in figure 4.17. The shunt resistance is very large and the series resistance is very small. Ideally, the series resistance should be zero, and the shunt resistance is considered extremely high.

Figure 4.16 Chroma solar array simulator model 62000H-S series.

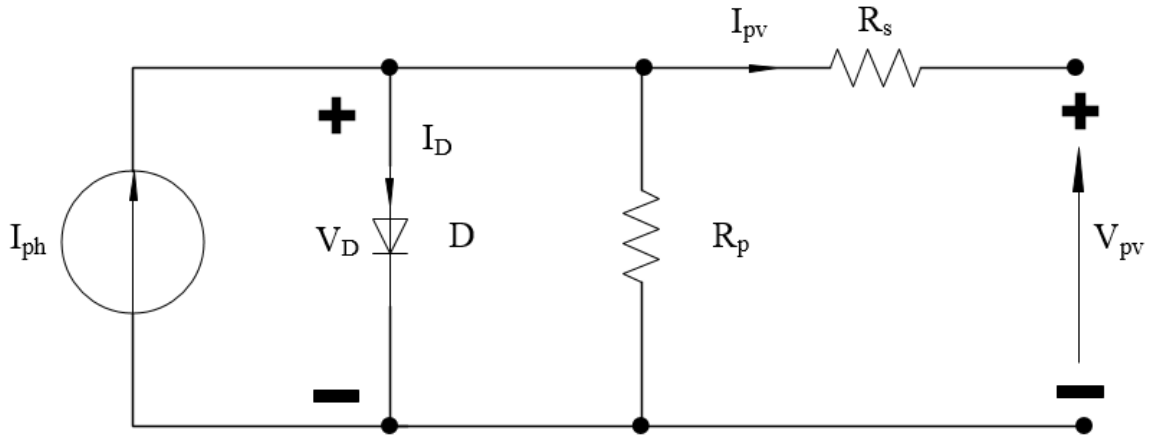

Figure 4.17 Equivalent circuit of Photovoltaic cell PV.

In short circuit conditions, the output voltage of the PV is zero. Therefore, no current flows through the diode and the shunt resistance. The output current of the PV cell in this case is equal to the current source output. The output current of the PV cell is zero in open circuit conditions, forcing the current to flow in the diode and the shunt resistance.

Table 4.6 Equivalent circuit of PV.

Element	Description
I_{ph}	Current source
V_D	Voltage across the diode

I_D	Diode Current
R_p	Shunt resistance
R_s	Series resistance
I_{pv}	Output current of PV
V_{pv}	Output voltage of PV

The I-V characteristics of a PV cell in figure 4.18, and the P-V curve in figure 4.19 are portrayed in equations 4.7-4.9, where k is Boltzmann constant ($k=1.38\times10^{-23}$ J/K), T is the temperature in Kelvin, and q is the electron charge ($q=1.6\times10^{-19}$ C).

$$I_{pv} = I_{ph} - \frac{V_D}{R_p} - I_D \qquad (4.7)$$

$$I_D = I_0\left(e^{\frac{qV_D}{nkT}} - 1\right) \qquad (4.8)$$

$$I_{pv} = I_{ph} - I_0\left(e^{\frac{qV_D}{nkT}} - 1\right) - \frac{V_D}{R_p} \qquad (4.9)$$

In order to operate the induction motor from the PV simulator, the full bridge diode rectifier is disconnected from the three phase inverter, and the PV simulator is connected directly to the DC bus of the inverter. However, the maximum voltage the solar array simulator can generate is 150 V. Due to this limitation, the motor will only run at 30 Hz, which corresponds to 1800 RPM.

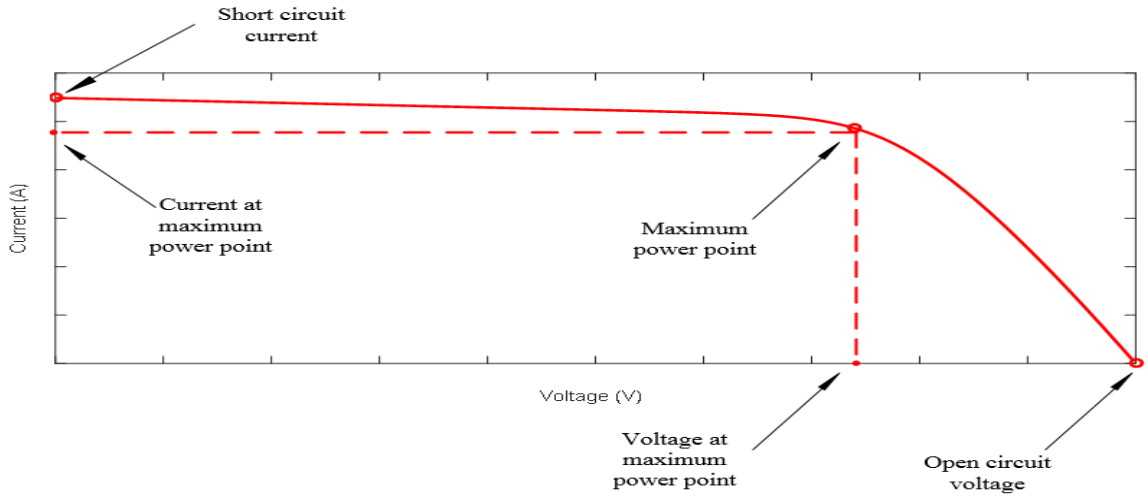

Figure 4.18 I-V characteristics of PV cell.

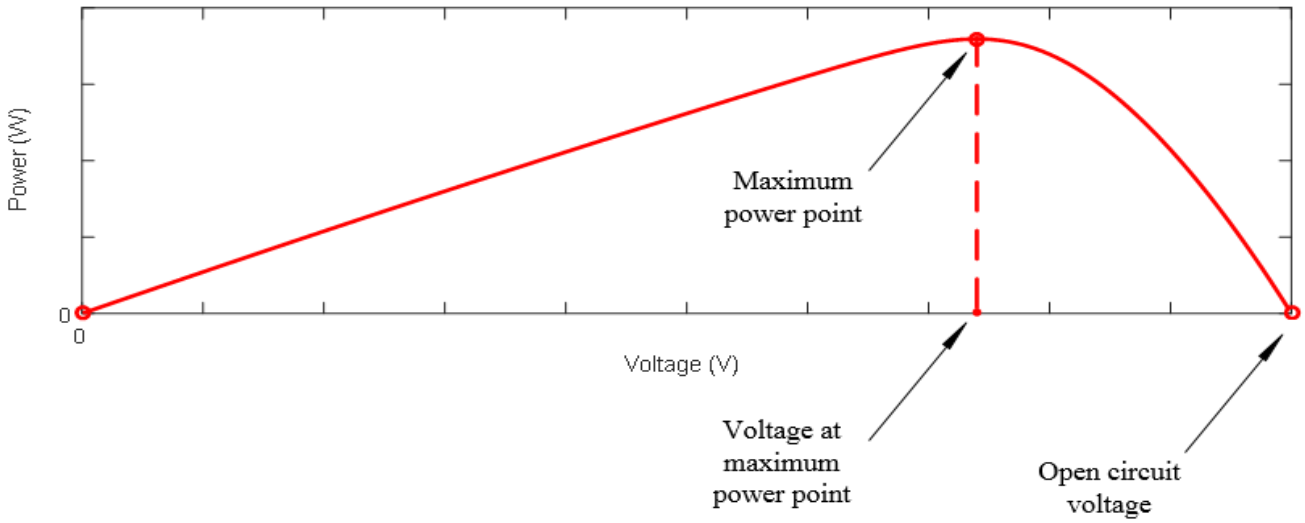

Figure 4.19 P-V curve of PV cell.

The required I-V characteristic is developed using MATLAB. The I-V characteristics that insures operating at the maximum power point is in figure 4.20. The solar array simulator is programmed to produce these I-V characteristics. The experimental setup after connecting the PV simulator and the Simulink model are shown in figures 4.21, and 4.22, respectively.

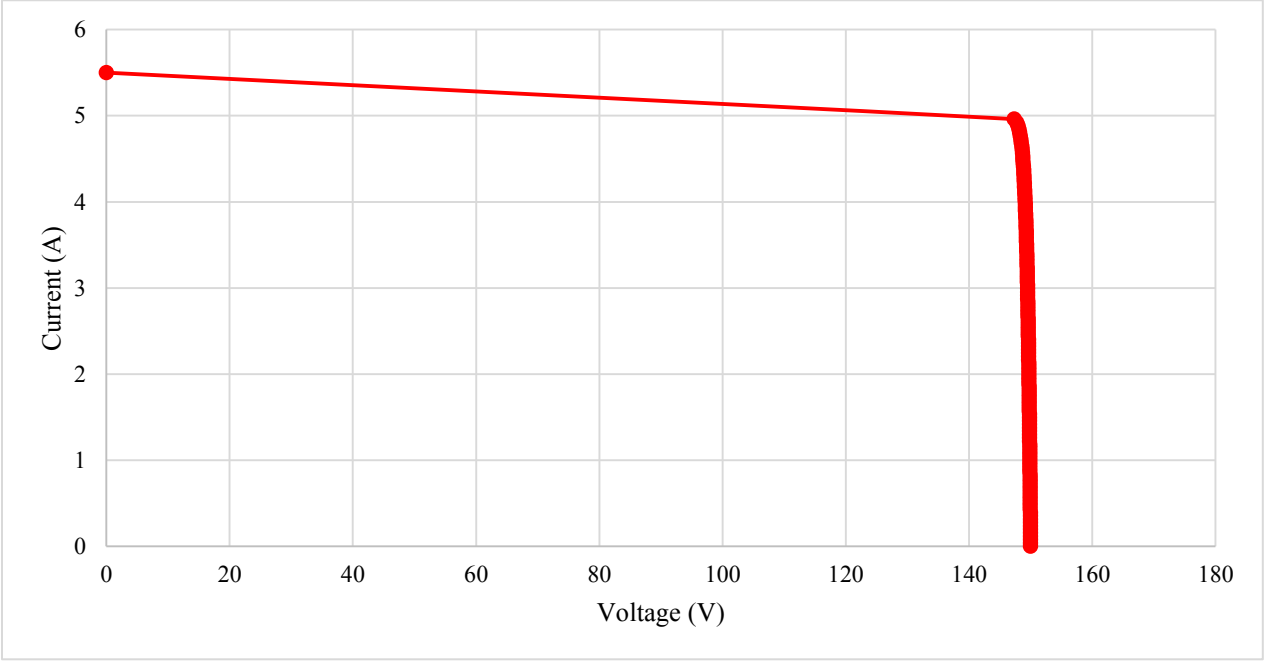

Figure 4.20 Programmed I-V characteristics.

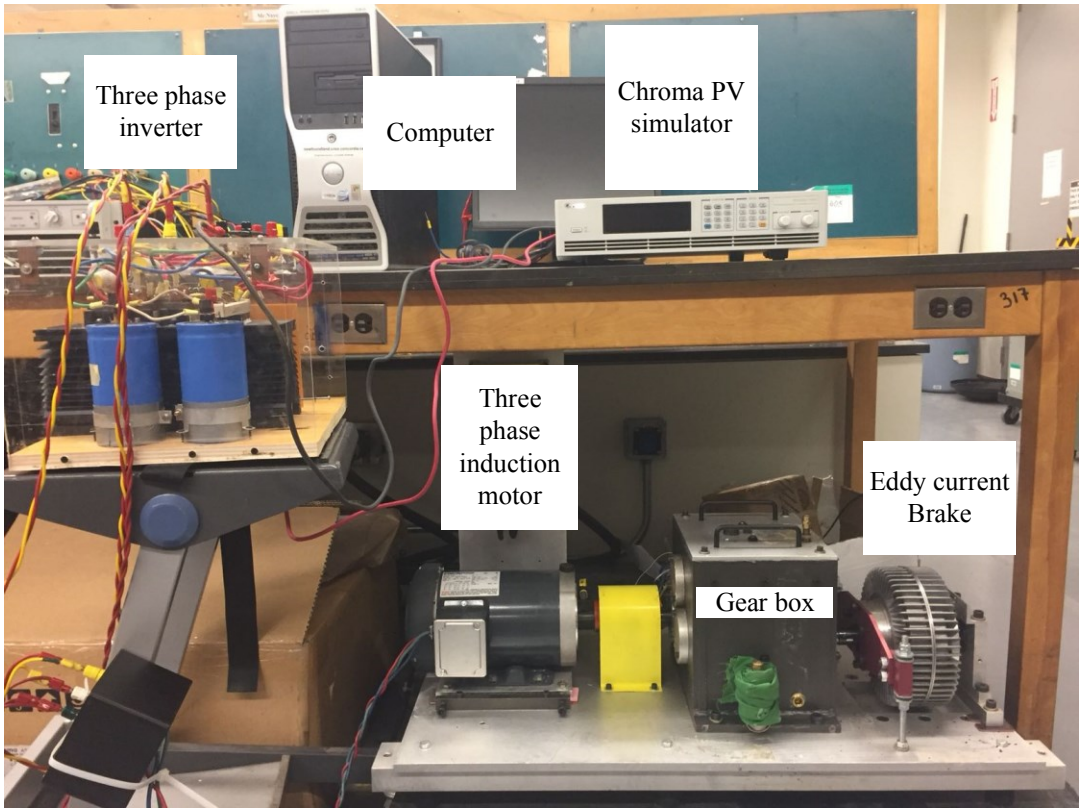

Figure 4.21 Experimental setup after connecting the solar simulator.

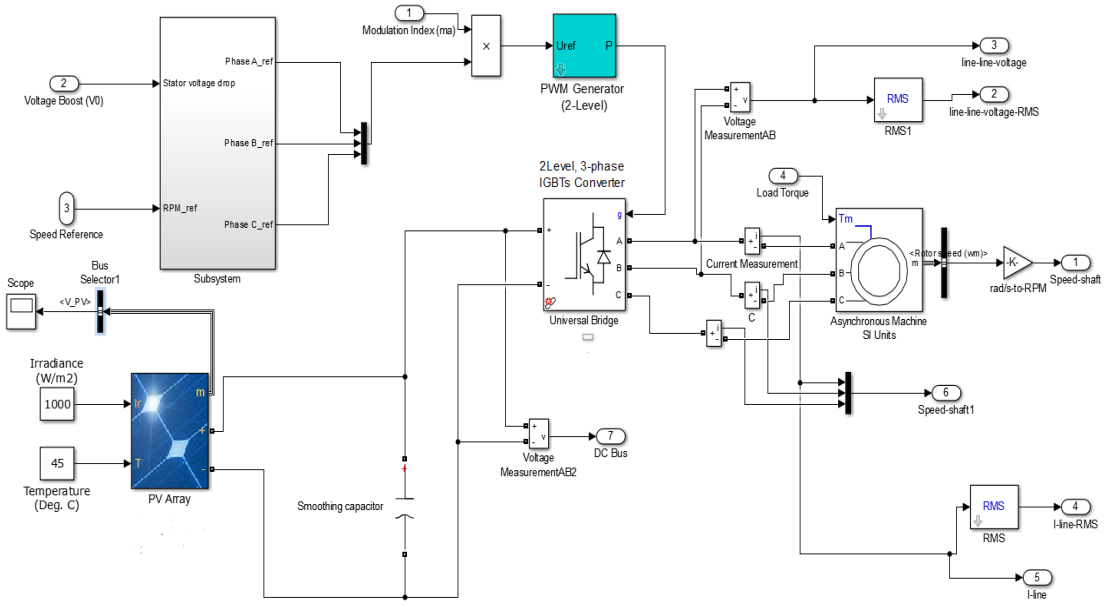

Figure 4.22 Simulink model after connecting the PV.

The Simulink model is simulated first. The RMS values of the currents drawn by the motor are 4.523 A, 4.518 A, and 4.520 A for phases A, B, and C, respectively. Figure 4.23 displays the simulated currents drawn. The DC bus voltage is 148 V and the RMS value of the line to line voltage is 112.9 V. Figure 4.24 shows the DC bus voltage and the line to line voltage waveforms, the motor is running at a speed of 1629 RPM.

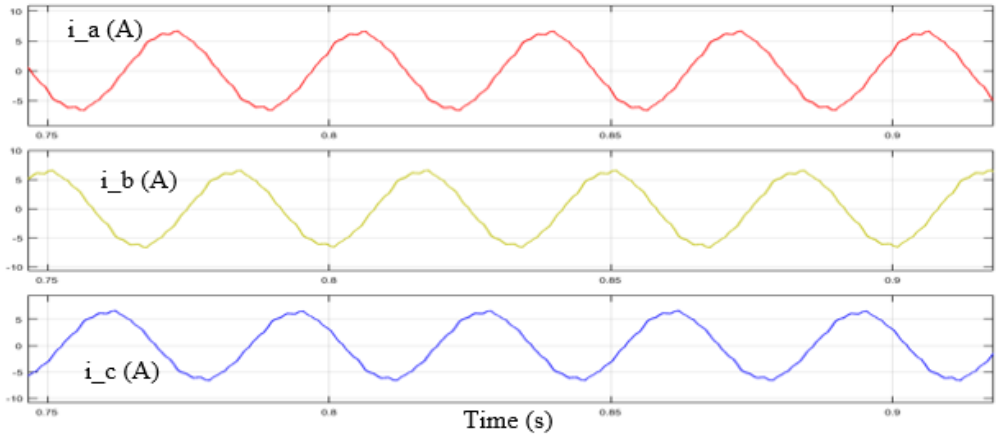

Figure 4.23 Three phase current drawn by the motor in Simulink at 30 Hz.

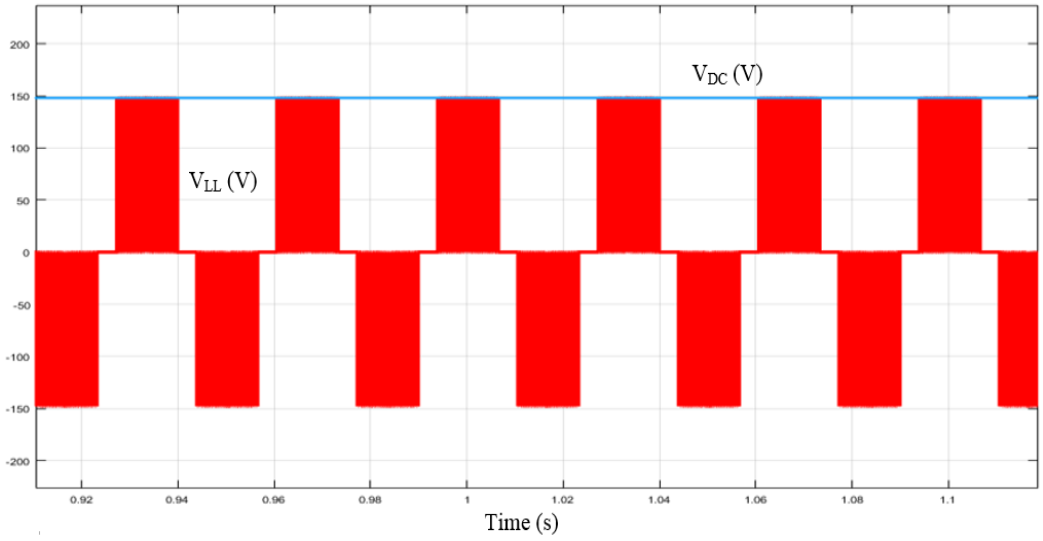

Figure 4.24 DC bus voltage and line to line voltage across the motor terminals in Simulink at 30 Hz.

The experimental setup in figure 4.21 is run to obtain the actual values for the comparison. The eddy current brake is used to load the motor. The motor is left running for three hours to reach

the rated temperature. After reaching steady state the three phase currents to the motor are captured using current probes connected to the motor terminals. Figure 4.25 shows the actual three phase currents. The RMS value of the drawn currents are 4.69 A, 4.65 A, and 4.77 A, for phases A, B, and C, respectively.

The line to line voltage, and the DC bus voltage are measured and shown in figure 4.26. The DC bus voltage is found to be 148 V, and the RMS value of the line to line voltage is 105 V. The actual speed is measured using a portable speed sensor. At 30 Hz reference, the measured motor speed is 1716 RPM.

Table 4.7 Case study comparison operating from the PV at 30 Hz.

30 Hz	Experimental setup	Simulink model
DC bus voltage (V)	148	148
RMS line to line voltage (V)	105	112.9
RMS line Currents (A)	4.69 4.65 4.77	4.523 4.518 4.520
Speed (RPM)	1716	1629

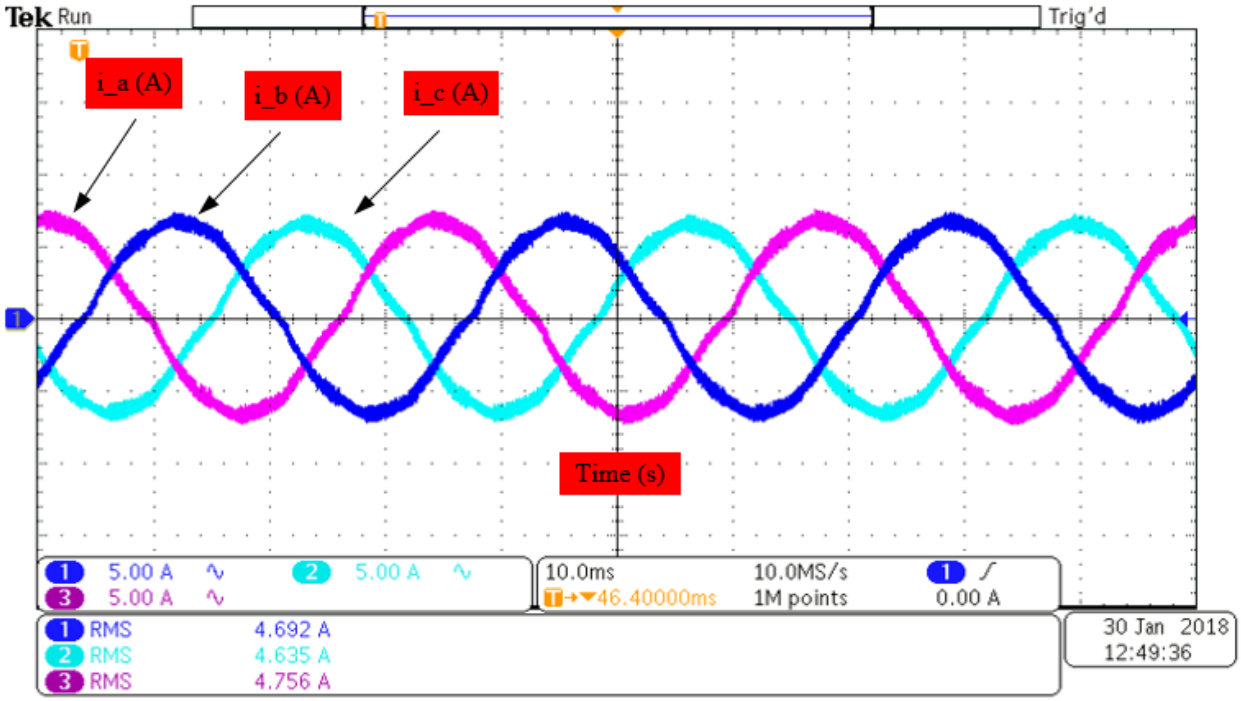

Figure 4.25 Three phase actual currents drawn by the motor at 30 Hz.

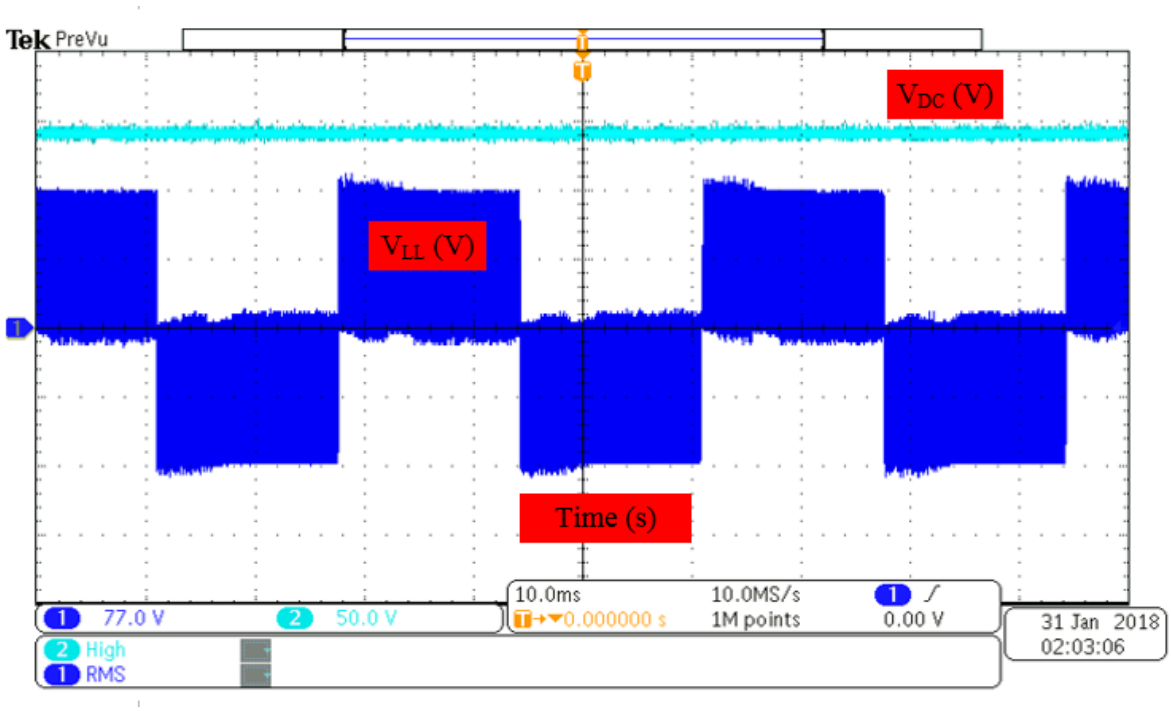

Figure 4.26 DC bus voltage and line to line voltage across the motor terminals at 30 Hz.

The PV simulator showed that when loading the motor at 30 Hz, the power drawn from the PV is 744.8 W which is at 96.45% of the maximum power which is 730.8 W. Figure 4.27 shows a segment of the software interface of the PV solar array simulator. The red dot in figure 4.27 represents the operating point of the PV simulator.

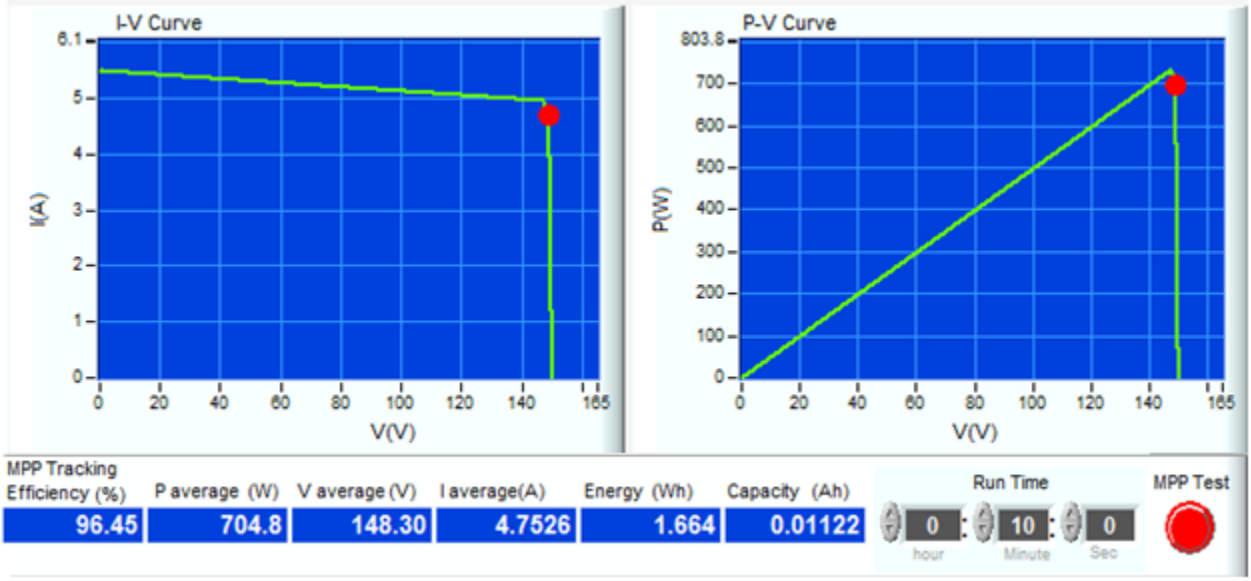

Figure 4.27 Chroma PV simulator screenshot.

4.4 Discussion

The three phase induction motor was supplied from the grid and from the PV simulator using the same three phase, two level inverter. The same control technique was implemented in both cases, and the same test conditions were taken into account. Due to the limitation imposed by the PV simulator, the motor was run at 30 Hz.

As can be seen from figure 4.28 in which the current drawn by the motor in phase A for both cases is shown, some key points are noticed; the current drawn from the grid has a small percentage of unbalance, as the peak value increases by 1.75 A every two cycles. The Total Harmonic Distortion (THD) is 0.6%, while when supplied from the PV simulator the peak value is constant and the THD is 0.1335%. The reduction in the THD is due to the cancelation of one conversion step. Instead of using a three phase diode bridge rectifier to power the DC bus, a separate DC source is directly connected. Hence, lower ripple in the DC bus voltage and therefore, increasing the lifetime of capacitor used to reduce the ripple in the DC bus voltage.

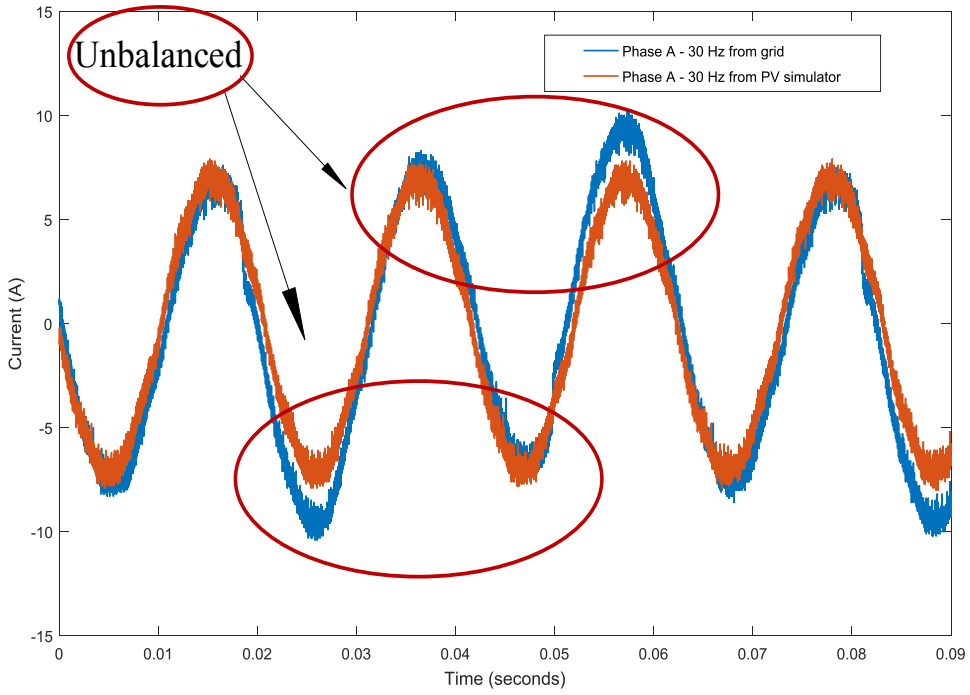

Figure 4.28 Phase A current at 30 Hz.

4.5 Summary

In this chapter, a case study to examine the performance of three phase induction motors and their electrical drives was conducted. The components of a case study were described. The equivalent circuit parameters of the induction motor to be used were extracted using Method 1 of IEEE Std 112TM – 2004. The extracted parameters were validated by simulating the motor at different frequencies and comparing the obtained measurements with the actual motor in the laboratory run under the same simulation conditions. The design procedure of a scalar V/f control scheme are explained and implemented in designing the control for a three phase two level inverter. Chroma Solar Array Simulator model 62000H-S was programmed to generate a specific I-V characteristics based on the operation requirements of the experimental setup. The three phase inverter was modified in order to connect the PV directly to the DC bus. The case study was run at 30 Hz because of the limitation imposed by the PV simulator. Comparing the current drawn when running the motor from the grid and from the PV simulator, the THD is reduced and the current peaks are more balanced when the three phase induction motor is operating from the PV array simulator.

CHAPTER 5

Conclusion and Future Work

5.1 Conclusion

A peak load shaving system is designed for the Louis-Hippolyte-La Fontaine Tunnel. The designed peak load shaving system utilizes Battery Energy Storage Systems (BESS) to store energy during off-peak hours. The stored energy is then discharged back to the electrical power system of the tunnel during peak hours reducing the peak load demand from the grid. A wide range of BESS sizes is studied, and the expected electrical bill savings are calculated by comparing the original load profile with the shaved load profile after the application of the BESS. Based on the electrical bill savings, the Net Present Value (NPV), Internal Rate of Return (IRR), and the Payback Period of each BESS size are calculated and used to decide the BESS size to be selected. The selected BESS size is the size that produces the highest peak load shaving while maintaining a positive NPV. The same method is followed to determine a BESS size when Photovoltaics solar farm (PV) is added to the network in conjunction with the BESS. The addition of PVs to the system allows for more peak shaving. This is true especially, when the peak load demand coincides with the peak production of the PV.

A control scheme is developed for Voltage Source Inverters (VSI) used in peak shaving applications. The developed control first allows the VSI to interface peak shaving systems with the grid reducing stress levels imposed on the grid, and secondly, play the role of power factor correction banks for reactive power compensation, and finally, inherit the capabilities of active harmonic filters and harmonic mitigation techniques to suppress the harmonic content in the line current. The proposed control strategy is developed using MATLAB/SIMULINK and validated experimentally where the peak shaving system and the VSI are connected to the grid in parallel with the load. The presented analysis highlights the overall power quality improvement attained from the control strategy when using the VSI as an intermediary between the peak shaving system and grid side. The proposed control strategy is validated under two different operation scenarios: first, operation under high harmonic distortion (THD), and secondly, operation under poor power factor conditions. The experimental results of the two operation scenarios show the potential

benefits of the proposed control strategy for power quality issues. The proposed control helped reducing the THD in the first operation scenario and improve the power factor of the load in the second case.

The performance of three phase induction motors and their electrical drives when operated from PV is investigated. A case study is created consisting of a three phase induction motor, a two level three phase inverter, and a solar array simulator. The equivalent circuit parameters of the induction motor are extracted using method 1 of the IEEE STD 112TM-2004. The extracted parameters are validated by comparing the simulation results obtained from simulating the motor in SIMULINK/MATLAB with those obtained from running the actual motor in the laboratory. Two operation frequencies are used to validate the extracted equivalent circuit parameters. A constant V/f control technique is developed and implemented to control the three phase induction motor. Based on the desired speed, the references for the three phase voltages are generated and fed to the inverter. The solar array simulator is connected to the DC bus of the three phase inverter and used to supply the three phase motor. Running the motor directly from the solar array simulator reduced the Total Harmonic Distortion (THD) in the motor line current when compared with the operation from the grid through a three phase diode bridge rectifier. The DC bus voltage when supplying the motor from the solar array simulator has less ripples, hence increasing the lifetime of the capacitor used to reduce the ripples.

5.2 Future Work

- The economic model, presented in section 2.5.2, can be improved by adding more economic parameters to enable a more accurate selection of BESS.
- The designed initial cost of capital, in section 2.5.3, is based on research papers and study reports. An estimation based on the market costs could be incorporated for more realistic results.
- A different control technique could be used to inject the required currents to the network, instead of the technique presented in section 3.2.4.
- The proposed control technique, presented in chapter 4, could be validated experimentally on a system capable of withstanding the rated voltage level of 208 V line to line.

REFERENCES

[1] A. Oudalov, R. Cherkaoui and A. Beguin, "Sizing and optimal operation of battery energy storage system for peak shaving application," in Power Tech, 2007 IEEE Lausanne, pp. 621-625, 2007.

[2] Hydro-Québec, "Electricity Rates Effective April 1, 2017." Hydro-Québec., Tech. Rep. ISBN 978-2-550-74418-4, 2017.

[3] M. Dabbagh, A. Rayes, B. Hamdaoui and M. Guizani, "Peak shaving through optimal energy storage control for data centers," in Communications (ICC), 2016 IEEE International Conference on, pp. 1-6, 2016.

[4] G. Ramya, V. Ganapathy and P. Suresh, "Power quality improvement using multi-level inverter based DVR and DSTATCOM using neuro-fuzzy controller," International Journal of Power Electronics and Drive Systems (IJPEDS), vol. 8, pp. 316-324, 2017.

[5] M. Awadalla, M. Omer and A. Mohamed, "Single-tuned filter design for harmonic mitigation and optimization with capacitor banks," in Computing, Control, Networking, Electronics and Embedded Systems Engineering (ICCNEEE), 2015 International Conference on, pp. 242-247, 2015.

[6] P. Karuppanan and K.K. Mahapatra, "Active harmonic current compensation to enhance power quality," International Journal of Electrical Power & Energy Systems, vol. 62, pp. 144-151, 2014.

[7] S. Srinath, M.S. Poongothai and T. Aruna, "PV Integrated Shunt Active Filter for Harmonic Compensation," Energy Procedia, vol. 117, pp. 1134-1144, 2017.

[8] B. Babes, L. Rahmani, A. Bouafassa, N. Hamouda and A. Chéraga, "Real Time Implementation of Shunt Active Power Filter (SAPF) for Harmonic suppression and Power Quality Improvement," Electrical Engineering, vol. 1, 2013.

[9] L. Morán and J. Dixon, "41 - Active Filters," in Power Electronics Handbook (Third Edition), M.H. Rashid, Boston: Butterworth-Heinemann, 2011, pp. 1193-1228.

[10] J. Abanto, M. Reggio, D. Barrero and E. Petro, "Prediction of fire and smoke propagation in an underwater tunnel," Tunnel.Underground Space Technol., vol. 22, pp. 90-95, 2007.

[11] D. MacLeod and P. Eng, "THE TRANS-CANADA HIGHWAY–A Major Link in Canada's Transportation System," in Transportation 2014: Past, Present, Future-2014 Conference and Exhibition of the Transportation Association of Canada//Transport 2014: Du passé vers l'avenir-2014 Congrès et Exposition de'Association des transports du Canada, 2014.

[12] Google Maps, "Tunnel Louis-Hippolyte-La Fontaine, Montreal, QC," https://www.google.ca/maps/place/LouisHippolyte+Lafontaine+Bridge%E2%80%93Tunnel,+Montreal,+QC/@45.5837317,73.5026333,17z/data=!3m1!4b1!4m5!3m4!1s0x4cc91d01cd9b1251:0xb97153aaf6a84e09!8m2!3d45.583728!4d-73.5004446, 2017.

[13] V. Papadopoulos, T. Delerue, J. Van Ryckeghem and J. Desmet, "Assessing the impact of load forecasting accuracy on battery dispatching strategies with respect to Peak Shaving and Time-of-Use (TOU) applications for industrial consumers," in Universities Power Engineering Conference (UPEC), 2017 52nd International, pp. 1-5, 2017.

[14] D. Katz, R. van Haaren and V. Fthenakis, "Applications and economics of combined PV and battery systems for commercial & industrial peak shifting," in Photovoltaic Specialist Conference (PVSC), 2015 IEEE 42nd, pp. 1-6, 2015.

[15] A. Oudalov, D. Chartouni, C. Ohler and G. Linhofer, "Value analysis of battery energy storage applications in power systems," in Power Systems Conference and Exposition, 2006. PSCE'06. 2006 IEEE PES, pp. 2206-2211, 2006.

[16] M. Shimoda, T. Yachi and Y. Kanai, "Economic evaluation of peak shift system using power demand forecasting," in Telecommunications Energy Conference (INTELEC), 2015 IEEE International, pp. 1-6, 2015.

[17] E. Telaretti and L. Dusonchet, "Battery storage systems for peak load shaving applications: Part 1: Operating strategy and modification of the power diagram," in Environment and Electrical Engineering (EEEIC), 2016 IEEE 16th International Conference on, pp. 1-6, 2016.

[18] R. Kempener and E. Borden, "Battery storage for renewables: market status and technology outlook," International Renewable Energy Agency (IRENA): Abu Dhabi, UAE, 2015.

[19] M.C. Ehrhardt and E.F. Brigham, Corporate finance: A focused approach, Cengage learning, 2016.

[20] R. Balakrishnan, K. Sivaramakrishnan and G. Sprinkle, Managerial accounting, John Wiley & Sons, 2008.

[21] G. Gupta, Managerial Economics, Tata McGraw-Hill Education, 2011.

[22] I.W. Seong, J.H. Yom, S.M. Cho and W.Y. Yoon, "Electrochemical Study of SiO Initial Efficiency for Lithium Ion Batteries," in Computer Science and Engineering (APWC on CSE), 2016 3rd Asia-Pacific World Congress on, pp. 78-83, 2016.

[23] K. Ardani, E. O'Shaughnessy, R. Fu, C. McClurg, J. Huneycutt and R. Margolis, "Installed Cost Benchmarks and Deployment Barriers for Residential Solar Photovoltaics with Energy Storage: Q1 2016," Installed Cost Benchmarks and Deployment Barriers for Residential Solar Photovoltaics with Energy Storage: Q1 2016, 2016.

[24] D. Katz, R. van Haaren and V. Fthenakis, "Applications and economics of combined PV and battery systems for commercial & industrial peak shifting," in Photovoltaic Specialist Conference (PVSC), 2015 IEEE 42nd, pp. 1-6, 2015.

[25] R. Fu, D. Chung, T. Lowder, D. Feldman, K. Ardani and R. Margolis, "US Solar Photovoltaic System Cost Benchmark: Q1 2016," National Renewable Energy Laboratory, US Department of Energy.NREL/TP-6A20-66532, 2016.

[26] N. DiOrio, A. Dobos and S. Janzou, Economic analysis case studies of battery energy storage with SAM, National Renewable Energy Laboratory, 2015, .

[27] P. Rao, M. Crow and Z. Yang, "STATCOM control for power system voltage control applications," IEEE Trans.Power Del., vol. 15, pp. 1311-1317, 2000.

[28] C. Liu, Y. He, K. Dai and Y. Kang, "Industrial power distribution system harmonic resonance problem and solution with shunt active power filter," in IECON 2017 - 43rd Annual Conference of the IEEE Industrial Electronics Society, pp. 1243-1248, 2017.

[29] S. C. Ferreira, R. B. Gonzatti, R. R. Pereira, C. H. da Silva, L. E. B. da Silva and G. Lambert-Torres, "Finite Control Set Model Predictive Control for Dynamic Reactive Power Compensation With Hybrid Active Power Filters," IEEE Transactions on Industrial Electronics, vol. 65, pp. 2608-2617, 2018.

[30] A. E. M. Bouzid, P. Sicard, A. Cheriti, H. Chaoui and P. M. Koumba, "Adaptive hysteresis current control of active power filters for power quality improvement," in 2017 IEEE Electrical Power and Energy Conference (EPEC), pp. 1-8, 2017.

[31] F. Wu, X. Li and J. Duan, "Improved elimination scheme of current zero-crossing distortion in unipolar hysteresis current controlled grid-connected inverter," IEEE Transactions on Industrial Informatics, vol. 11, pp. 1111-1118, 2015.

[32] J. Du, H. Zhao and T.Q. Zheng, "Study on a switching-pattern hysteresis current control method based on zero voltage vector used in three-phase PWM converter," IET Power Electronics, vol. 10, pp. 2190-2198, 2017.

[33] F. Wu, B. Sun, K. Zhao and L. Sun, "Analysis and solution of current zero-crossing distortion with unipolar hysteresis current control in grid-connected inverter," IEEE Trans.Ind.Electron., vol. 60, pp. 4450-4457, 2013.

[34] Y. Lu, G. Xiao, X. Wang and F. Blaabjerg, "Grid Synchronization with Selective Harmonic Detection Based on Generalized Delayed Signal Superposition," IEEE Transactions on Power Electronics, 2017.

[35] F. Baradarani, M.R.D. Zadeh and M.A. Zamani, "A phase-angle estimation method for synchronization of grid-connected power-electronic converters," IEEE Trans.Power Del., vol. 30, pp. 827-835, 2015.

[36] X. Cai, C. Wang and R. Kennel, "A Fast and Precise Grid Synchronization Method Based on Fixed Gain Filter," IEEE Trans.Ind.Electron., 2018.

[37] S. Gude and C. Chu, "Three-phase grid synchronization PLL using multiple delayed signal cancellation under adverse grid voltage conditions," in Industry Applications Society Annual Meeting, 2017 IEEE, pp. 1-8, 2017.

[38] A.G. Siraki and P. Pillay, "Comparison of two methods for full-load in situ induction motor efficiency estimation from field testing in the presence of over/undervoltages and unbalanced supplies," IEEE Trans.Ind.Appl., vol. 48, pp. 1911-1921, 2012.

[39] F. Edition and S.J. Chapman, "Electric Machinery Fundamentals," 2004.

[40] J.M. Peña and E.V. Díaz, "Implementation of V/f scalar control for speed regulation of a three-phase induction motor," in ANDESCON, 2016 IEEE, pp. 1-4, 2016.

[41] M. Martinez-Hernandez, J. Gutierrez-Villalobos, S. Malagon-Soldara, F. Mendoza-Mondragon and J. Rodriguez-Resendiz, "A speed performance comparative of field oriented control and scalar control for induction motors," in Mechatronics, Adaptive and Intelligent Systems (MAIS), IEEE Conference on, pp. 1-7, 2016.

[42] N.R.N. Idris and T. Sutikno, "High performance direct torque control of induction motor drives: Problems and improvements," in Electrical Engineering, Computer Science and Informatics (EECSI), 2017 4th International Conference on, pp. 1-7, 2017.

[43] A. Smith, S. Gadoue, M. Armstrong and J. Finch, "Improved method for the scalar control of induction motor drives," IET Electric Power Applications, vol. 7, pp. 487-498, 2013.

[44] M. Bechar, A. Hazzab and M. Habbab, "Real-Time Scalar Control of Induction Motor using RT-Lab Software".

[45] Z. Yang, X. Li, C. Zhang and S. Chi, "A new slip compensation method for induction motors based on current vector decoupling," in Electrical Machines and Systems (ICEMS), 2017 20th International Conference on, pp. 1-6, 2017.

[46] J.S. Hsu, J.D. Kueck, M. Olszewski, D.A. Casada, P.J. Otaduy and L.M. Tolbert, "Comparison of induction motor field efficiency evaluation methods," in Industry Applications Conference, 1996. Thirty-First IAS Annual Meeting, IAS'96. Conference Record of the 1996 IEEE, pp. 703-712, 1996.

[47] V. K. A. Shankar, S. Umashankar, S. Paramasivam, Y. Venkatesh, K. Venkatesh and K. N. D. Sailesh, "Mathematical modelling and investigation of reduced order induction motor drive system," in 2017 Innovations in Power and Advanced Computing Technologies (i-PACT), pp. 1-8, 2017.

[48] N. Mohan, Power electronics: a first course, Wiley, 2011.

[49] M. Ünlü and S. Çamur, "A simple Photovoltaic simulator based on a one-diode equivalent circuit model," in Electrical and Electronic Engineering (ICEEE), 2017 4th International Conference on, pp. 33-36, 2017.

[50] M.A. Mohamed, "Efficient approximation of photovoltaic model using dependent thevenin equivalent circuit based on exponential sums function," in Photovoltaic Specialist Conference (PVSC), 2015 IEEE 42nd, pp. 1-6, 2015.

[51] K. Matsuda, N. Nagaoka, T. Higo and A. Namba, "A simple lumped-equivalent circuit of a photovoltaic panel for transient simulations," in Power Engineering Conference (UPEC), 2014 49th International Universities, pp. 1-5, 2014.